Design and Characterization of Silicon-on-Insulator Passive Polarization Converter with Finite-Element Analysis

by

Henghua Deng

A thesis
presented to the University of Waterloo
in fulfillment of the
thesis requirement for the degree of
Doctor of Philosophy
in
Electrical and Computer Engineering

Waterloo, Ontario, Canada, 2005

© Henghua Deng 2005

I hereby declare that I am the sole author of this thesis. This is a true copy of the thesis, including any required final revisions, as accepted by my examiners.

I understand that my thesis may be made electronically available to the public.

Abstract

As optical fiber systems evolve to higher data rates, the importance of polarization control and manipulation steadily increases. Polarization manipulating devices, such as polarization splitters and converters, can be realized by introducing material anisotropy or geometric asymmetry. Compared to active devices, passive polarization converters are more simply fabricated and controlled, therefore they have attracted increasing attention during the past two decades. However, materials employed in previous polarization rotating waveguides are mainly limited to low index-contrast III-V semiconductors such as InP and GaAs. Such III-V devices possess large radiation loss, large curvature loss, and low coupling efficiency to single-mode fibers; in addition, due to the weak optical confinement, the device spacing has to be large, which prevents high-density and large-scale integration in optoelectronic integrated circuits (OEIC) and planar lightwave circuits (PLC).

In this dissertation, the silicon-on-insulator (SOI) technology is introduced to the design and fabrication of passive polarization rotators (PR). Efficient and accurate full-vectorial finite-element eigenmode solvers as well as propagation schemes for characterizing novel SOI PRs are developed because commercial software packages based on finite-difference techniques are inefficient in dealing with arbitrary waveguide geometries.

A set of general design procedures are accordingly developed to design a series of slanted-angle polarization converters, regardless of the material system (SOI or III-V), outer-slab layer configuration (symmetric or asymmetric), and longitudinal loading (single- or multi-section). In particular, our normalized design charts and simple empirical formula for SOI polarization converters are applicable to a wide range of silicon-guiding-film thickness, e.g., from 1 to 30 μm, enabling fast and accurate polarization rotator design on most commercial SOI wafers. With these procedures, in principle 100% polarization conversion efficiency can be achieved by optimizing waveguide geometric parameters.

A novel configuration with asymmetric external waveguiding layers is proposed, which is advantageous for fabrication procedure, manufacturing tolerance, single-mode region, and conversion efficiency. By etching along the crystallographic plane, the angled-facet can be perfectly fabricated. Completely removing external waveguiding layer beside the sloped sidewall not only simplifies production procedures but also enhances fabrication tolerances.

To accurately and efficiently characterize asymmetric slanted-angle SOI polarization converters, adaptive mesh generation procedures are incorporated into our finite-element method (FEM) analysis. In addition, anisotropic perfectly-matched-layer (PML) boundary condition (BC) is employed in the beam propagation method (BPM) in order to effectively suppress reflections from the edges of the computation window. For the BPM algorithm, the power conservation is strictly monitored, the non-unitarity is thoroughly analyzed, and the inherent numerical dissipation is reduced by adopting the quasi-Crank-Nicholson scheme and adaptive complex reference index.

Advantages of SOI polarization rotators over III-V counterparts are studied through comprehensive research on power exchange, single-mode condition, fabrication tolerance, wavelength stability, bending characteristics, loss and coupling properties. The performance of SOI PRs is stable for wavelengths in the ITU-T C-band and L-band, making such devices quite suitable for DWDM applications. Due to the flexible cross-section of SOI polarization converters, the coupling loss to laser diodes and single mode fibers (SMF) can be designed to be very small and can be further reduced by a tapered waveguide with cross-sections always satisfying the single-mode criteria. Slanted-angle SOI polarization rotators display asymmetric bending characteristics and permit extremely small curvatures with negligible radiation loss when the angled-facet is located at the outer bend radius. Moreover, SOI polarization rotators can be manufactured with low-price processing techniques that are fully compatible with CMOS integrated circuits (IC) technology, and thus can be integrated on both photonic and electronic chips.

Experimental verifications have shown good agreement with theoretical analysis and have confirmed the promising characteristics of our novel asymmetric SOI polarization converters. Similar asymmetric-outer-slab geometry has recently been employed by peer researchers to fabricate high performance III-V polarization rotators. We therefore believe that results in this dissertation will contribute much to related research fields.

***Index Terms*:** Polarization Rotator (PR), Silicon-on-Insulator (SOI), III-V semiconductor, Finite Element Method (FEM), Beam Propagation Method (BPM), Adaptive Meshing, Perfectly Matched Layer (PML), Numerical Dissipation, Conformal Mapping Method, Integrated Optics, Silicon Photonics, Nanophotonics, Optoelectronic Integrated Circuit (OEIC), Planar Lightwave Circuit (PLC), Dense Wavelength Division Multiplexing (DWDM)

Acknowledgements

First and foremost, I would like to express my sincere gratitude to my supervisors Prof. David O. Yevick and Prof. Sujeet K. Chaudhuri at the University of Waterloo. Their knowledge, understanding, guidance, inspiration and encouragement are invaluable to the success of my research projects. It is really one of the luckiest things in my life that I have studied under their supervision during the past years, and what I have learned from them will definitely benefit me greatly in my future careers.

I especially thank Prof. Paul E. Jessop and Christopher Brooks at McMaster University for their fruitful collaboration and wonderful experimental support.

Many thanks are due to the members of my doctoral committee, Prof. Anand Gopinath at the University of Minnesota, Minneapolis, Prof. Safieddin Safavi-Naeini, Prof. Yung Leonard Chow, Prof. Joseph Sanderson, Prof. John Smith, and Prof. Arokia Nathan at the University of Waterloo, for their valuable time, helpful advice and important comments.

I thank the Canadian Institute for Photonic Innovations (CIPI), the Natural Science and Engineering Research Council of Canada (NSERC), the National Research Council Canada (NRC), and Nortel Networks for financial support.

Deep appreciation also goes to Prof. Witold Bardyszewski (University of Warsaw, Poland), Prof. Amir Hamed Majedi, Tao Lu, Benedict Chukwuka Ofuonye (currently with the University of Illinois — Urbana-Champaign), Magnus Wik (currently with the Swedish Institute of Space Physics), Luis Manuel de Menezes, Dr. Yaxun Liu (currently with the University of Toronto), Dr. Zhongde Wang (University of Michigan — Ann Arbor, currently with Ansoft Inc.), Xuan Chen, Daryoosh Saeedkia, Mohammed Basha, and many other friends, for their help during my study at the University of Waterloo.

Last, but certainly not the least, I am much obliged to my family. I would like to thank my wife Li Xiao, for her love, understanding, support, and sacrifice during our unforgettable years in Canada; my son William, for the sunshine, comfort, and happiness brought to my heart; and my parents and siblings, for their understanding, encouragement, and sacrifice from tens-of-thousands of miles away.

Henghua Deng
June 22, 2005

Contents

List of Tables

List of Figures

List of Acronyms

III-V	semiconductors such as AlGaAs/GaAs and InGaAsP/InP
ABC	Absorbing Boundary Condition
AWG	Arrayed Waveguide Grating
BC	Boundary Condition
BEM	Boundary Element Method
BPM	Beam Propagation Method
CMT	Coupled Mode Theory
CMOS	Complementary Metal Oxide Semiconductor
CT-LN	Constant Tangential /Linear Nodal triangle (1st order mixed element)
DWDM	Dense Wavelength Division Multiplexing
EIM	Effective Index Method
ESW	Equivalent Straight Waveguide Method
FD	Finite-Difference
FDM	Finite Difference Method
FDTD	Finite-Difference Time-Domain method

FDTD-BPM	Finite-Difference Time-Domain Beam-Propagation Method
FD-BPM	Finite-Difference Beam-Propagation Method
FE	Finite-Element
FEM	Finite Element Method
FE-BPM	Finite-Element Beam-Propagation Method
FFT-BPM	Fast-Fourier-Transform Beam-Propagation Method
FV	Full Vectorial
FV-FEM	Full-Vectorial Finite Element Method
ID-BPM	Imaginary-Distance Beam-Propagation Method
I/O	Input/Output
LAS	Left Asymmetric Structure
LSM	Least-Squares-Method
LT-QN	Linear Tangential/Quadratic Nodal triangle(2nd order mixed element)
MFD	Mode Field Diameter
MMI	Multi-Mode Interferometer
MoL	Method of Lines
MoM	Method of Moments
MZI	Mach-Zehnder Interferometer
OEIC	Optoelectronic Integrated Circuit
PIC	Photonic Integrated Circuit

PLC	Planar Lightwave Circuit
PML	Perfectly Matched Layer
PR	Polarization Rotator
PRW	Polarization Rotating Waveguide
RAS	Right Asymmetric Structure
RIE	Reactive Ion Etching
SC-FEM	Scalar Finite Element Method
SEM	Scanning Electron Microscope
SM	Single-Mode
SMF	Single-Mode Fiber
SOI	Silicon-on-Insulator
SSC	Spot-Size Converter
SVEA	Slowly Varying Envelop Approximation
SV-FEM	Semi-Vectorial Finite Element Method
TBC	Transparent Boundary Condition
TE	transverse-electric
TM	transverse-magnetic
TMAH	TetraMethyl Ammonium Hydroxide
VLSI	Very Large Scale Integration
WDM	Wavelength Division Multiplexing

List of Symbols

t	time
(x, y, z)	Cartesian coordinates (x-horizontal, y-vertical, z-longitudinal)
$(\boldsymbol{i}_x,\ \boldsymbol{i}_y,\ \boldsymbol{i}_z)$	unit vectors along $(x,\ y,\ z)$ directions
$(u,\ v)$	optical axes
∇	del (nabla) operator (in Cartesian coordinates $= \boldsymbol{i}_x \frac{\partial}{\partial x} + \boldsymbol{i}_y \frac{\partial}{\partial y} + \boldsymbol{i}_z \frac{\partial}{\partial z} = \nabla_t + \boldsymbol{i}_z \frac{\partial}{\partial z}$)
∇_t	transversal del operator (in Cartesian coordinates $= \boldsymbol{i}_x \frac{\partial}{\partial x} + \boldsymbol{i}_y \frac{\partial}{\partial y}$)
∇^2	Laplacian operator (in Cartesian coordinates $= \frac{\partial^2}{\partial x^2} + \frac{\partial^2}{\partial y^2} + \frac{\partial^2}{\partial z^2}$)
$\nabla,\ \nabla\cdot,\ \nabla\times$	grad, div, curl operations
Δ	differential or waveguide index-contrast
$(\varepsilon,\ \mu)$	(permittivity, permeability) of dielectric material ($\varepsilon = \varepsilon_0 \varepsilon_r,\ \mu = \mu_0 \mu_r$)
$(\varepsilon_r,\ \mu_r)$	relative (permittivity, permeability) ($\mu_r = 1$ for non-magnetic materials)
ε_0	free space permittivity ($= 8.854187817 \times 10^{-12}$ F/m)
μ_0	free space permeability ($= 4\pi \times 10^{-7}$ H/m)
$(\sigma_E,\ \sigma_H)$	electric and magnetic conductibility
Z_0	intrinsic impedance of vacuum ($Z_0 = \sqrt{\frac{\mu_0}{\varepsilon_0}} = 376.7303134749689\Omega$)
n_{eff}	effective index
n_0	reference index used in beam-propagation method (BPM)
$n,\ n_1,\ n_2,\ n_3$	refractive indices of materials ($n = \sqrt{\varepsilon_r}$)
$(n_x,\ n_y,\ n_z)$	refractive indices of the material along $(x,\ y,\ z)$ directions
$[p]$, $[q]$	permittivity- and permeability- tensor
$[\Lambda]$, $[s]$	perfectly matched layer (PML) tensor

$\boldsymbol{E}$	electric field
$\boldsymbol{H}$	magnetic field
φ	optical axes rotation angle (formed by $(u,\, v)$ and $(x,\, y)$)
c	velocity of the light in vacuum $(= \dfrac{1}{\sqrt{\mu_0 \varepsilon_0}} = 2.99792458 \times 10^8\,\mathrm{m/s})$
ν	velocity of the light in dielectric materials $(= \dfrac{1}{\sqrt{\mu\varepsilon}})$
f	frequency
ω	angular frequency $(= 2\pi f)$
λ	wavelength
k	wavenumber $(= 2\pi/\lambda)$; in free space denoted as k_0
β	propagation constant $(= n_{eff} k_0)$
b	normalized propagation constant
$\phi,\, \psi$	either the electric field $\boldsymbol{E}$ or the magnetic field $\boldsymbol{H}$
$\{\phi_t\}$	transverse tangential field $(= \boldsymbol{i}_x \phi_x + \boldsymbol{i}_y \phi_y)$
$(\phi_x,\, \phi_y)$	transverse field components along $(x,\, y)$ directions
ϕ_z	longitudinal field component
Ω	waveguide cross-section region (denoted as Ω_e for each finite-element)
e	an element number in finite-element analysis
$(L_1,\, L_2,\, L_3)$	area coordinates (local coordinates) for a triangular element
$\{N\}$	scalar-based shape function for nodal element
$\{U\},\, \{V\}$	vector-based shape function for edge element $(\boldsymbol{i}_x\{U\} + \boldsymbol{i}_y\{V\})$
$\{N_x, N_y, U_x, U_y, V_x, V_y\}$	derivatives of shape functions $\{N_x\} = \dfrac{\partial\{N\}}{\partial x}$, $\{N_y\} = \dfrac{\partial\{N\}}{\partial y}$, $\{U_x\} = \dfrac{\partial\{U\}}{\partial x}$, $\{U_y\} = \dfrac{\partial\{U\}}{\partial y}$, $\{V_x\} = \dfrac{\partial\{V\}}{\partial x}$, $\{V_y\} = \dfrac{\partial\{V\}}{\partial y}$
(N_e, N_p, N_t)	number of (triangular elements, nodal points, tangential edges)
$[K^e],\, [M^e]$	elemental matrices of each finite-element
$[K],\, [M]$	global matrices related to waveguide cross-section
$(w,\, w_e,\, w_{th})$	(total weight, element weight, threshold weight) in adaptive meshing
α	the difference parameter in BPM algorithms
W	base rib width in a rib waveguide
H	rib height in a rib waveguide
$(h,\, h_r)$	thickness of (left, right) outer-slab layer in a rib waveguide

$(r,\, s)$	normalized rib height and width ($r = h/H,\, s = W/H$)
θ	slanted-angle in an angled-facet rib waveguide
ϑ	phase delay for different polarizations in birefringent waveguides
θ_p	polarization angle regarding to x-axis ($= tan^{-1}\left(\frac{P_y}{P_x}\right)$)
δ	alignment offset
$(d_c,\, d_p,\, d_i,\, d_s)$	other waveguide geometry parameters
L	length or propagation distance
L_π	half-beat length of birefringent materials or waveguides
L_T	transition loss
L_b	bending loss
L_c	coupling length
R	rotation parameter indicating the ratio of TE and TM field components
R_c	bending radius of a curved waveguide
P	power of the electromagnetic field
PC	polarization conversion efficiency
ER	extinction ratio

Chapter 1

Introduction

As information exchange demands are exploding in today's communications, optical communication systems are developing with increasing transmission capacities, e.g., 10G/s, 40G/s to 160G/s, which impose a strong necessity in dense integration of both electronic and photonic circuits. In high density electronics, very large scale integration (VLSI) circuits have taken the place of many traditional discrete tubes and transistors. Similarly, in present and next-generation photonic systems, large-scale planar lightwave circuits (PLC) and optoelectronic integrated circuits (OEIC) will inevitably substitute most discrete optical components in early fiber optics. The advent of dense wavelength division multiplexing (DWDM) technology greatly enhances the transmission capacity of a single optical fiber; however, it requires each channel to present such characteristics as low insertion-, coupling-, and polarization-dependent-losses, small signal- and polarization-crosstalk, and good wavelength- and thermal-stability, etc.

Due to the existence of birefringence, light with different polarizations travel at different group velocities in optical fibers and waveguides, causing the spreading of light pulses and consequently signal distortion and system performance degradation. Common factors contribute to the birefringence are asymmetric geometry, material anisotropy, mechanical stress, thermoelastic effect, photoelastic effect and electro-optical effect, etc. The importance of polarization control and manipulation has become obvious; therefore, the main research topic of this thesis is to explore novel high-performance polarization manipulating devices for integrated optics.

1.1 Impetus and Objective

In integrated optics, two main categories of polarization manipulating devices are polarization splitters and polarization converters: the former separates hybrid polarizations into two independent orthogonally-positioned polarizations, and the latter converts one polarization state of light into the other. Polarization splitters are important in applications where specific states of polarization direction are needed, e.g., optical systems for sensing, imaging, data storage, and signal processing. Structures such as directional couplers, multi-mode interference (MMI) couplers, Mach-Zehnder interference (MZI) couplers, and Y-junctions have been adopted for polarizing beam splitters. On the other hand, polarization converters find wide applications in polarization-maintaining systems and can be achieved with geometries as simple as rib waveguides. In this thesis, we therefore focus on polarization converters which offer arbitrary and continuous polarization control.

To realize a polarization manipulating device, we have methods employing voltage-controlled electrodes. The electric field applied by these electrodes leads to electro-optic or thermal-strain effects, which cause some difference in the ordinary and extraordinary refractive indices. However, cumbersome extraordinary procedures are required to fabricate metal electrodes over dielectric waveguides, and very accurate control of electric voltage is needed in such devices. In contrast, passive polarization controlling devices fabricated with solely dielectric materials do not encounter these difficulties, and have attracted increasing attention during the past two decades.

Early passive polarization rotations (PR) utilize periodic asymmetrical-loading in the longitudinal direction. As a result, small conversions between polarization states are accumulated by the periodic perturbation in the optical-axes, leading to a strong polarization rotation after a sufficiently long distance. However, fabrication of multi-section periodic structures is complicated, and unavoidable losses occur at junctions between adjacent sections. In addition, the length of such devices tends to be quite long, which limits their application in compact photonic integrated circuits (PIC).

By enhancing the asymmetry of waveguide cross-section through careful optimizations, the polarization rotating effects can be significantly improved, resulting in single-section polarization converters. Currently, most of these devices employ slanted-angle (also named as angled-facet) rib waveguides made of low index-contrast III-V (InP and GaAs, etc.)

semiconductors. These polarization rotating waveguides (PRW) generally have a small guiding region for single-mode propagations and a thick substrate, leading to large overall cross-section, small coupling loss to single-mode fibers (SMF), and large radiation loss into the substrate. In addition, since optical fields are not well-confined in the guiding region, these devices present large bending radius and bending losses. As a result, the device size tends to be large, which is disadvantageous for high-density integration. In contrast, high index-contrast materials overcome these difficulties due to the strong optical confinement.

The silicon-on-insulator (SOI) technology, offering extremely high index-contrast for optical waveguides, has consequently been fast developing in the field of integrated optics since middle 1980s. SOI, a main platform for both silicon photonics and VLSI CMOS electronics, enables large-scale and high-density integration of optoelectronic integrated circuits (OEIC). To the best of our knowledge, though SOI has found various applications in directional-, MMI- and MZI-couplers, waveguide gratings, wavelength multiplexers, photodetectors and modulators, it has not been considered for polarization converters prior to this research. To fully utilize the advantages of both the silicon-on-insulator technology and single-section polarization converter structures, this thesis is therefore focused on designing and analyzing novel SOI polarization rotators.

1.2 Thesis Contribution

The main contribution of this thesis is that a series of SOI passive polarization rotators have been accomplished with a systematic procedure. Asymmetric external-waveguiding-layer geometry is employed in the design of polarization converters as it shows better performances compared with conventional slanted-angle structures with symmetric outer-slab layers. Advantages of SOI PRs, such as compact size, small bending loss, good coupling to single mode fibers, are elaborated by comparing with III-V counterparts. General normalized charts and a simple empirical formula are proposed to design slanted-angle polarization converters, regardless of the material system (SOI or III-V), outer-slab layer configuration (symmetric or asymmetric), and longitudinal loading (single- or multi-section), etc. For SOI polarization rotators, the general design charts illustrated in this thesis can be approximately applied to a wide range of silicon-guiding-film thickness from 1 to 30μm.

In order to analyze high-index-contrast asymmetric angled-facet waveguides efficiently and accurately, after pointing out the incapability of other numerical schemes such as the finite difference method (FDM), we develop full-vectorial (FV) finite element method (FEM) programs for both eigenmode solver and beam-propagation analysis. The perfectly matched layer (PML) boundary condition (BC) as well as adaptive techniques for generating non-uniform meshes and renewing reference index are incorporated into the sophisticated and versatile computer codes. The non-unitarity of the propagation operators in the mixed-element beam propagation method (BPM) is carefully analyzed. To predict the power exchange behavior of SOI polarization rotators as reliably as possible, the quasi-Crank-Nicholson scheme and complex reference index technique are employed. With these efficient numerical algorithms, the fabrication tolerance, power exchange, polarization conversion, bending characteristics, coupling and loss issues associated with novel SOI polarization rotators are thoroughly studied.

The theoretical research in this dissertation has resulted in a series of publications [1–7]. The experimental verification of our SOI polarization rotators conducted by McMaster University (partially in collaboration with Carleton University) has lead to a M.A.Sc degree thesis [8], a conference paper [7], and a journal paper [5]. Our concept of asymmetric external-waveguiding-layer (outer-slab) configuration has recently been employed by Dr. Meint K. Smit's research group at the Eindhoven University of Technology, the Netherlands [9, 10]. We therefore believe that our general design procedures and novel SOI polarization converter structures will find wide application in optical communication systems.

1.3 Thesis Organization

The thesis is organized as follows:

Chapter 2 gives an overview of polarization rotators and silicon-on-insulator technology. The operation principle of asymmetric passive polarization converters as well as the merits and challenges of silicon photonics are discussed in detail in this chapter.

Chapter 3 presents numerical procedures associated with finite-element eigenmode solvers. Three formulations (scalar, semi-vectorial, and full-vectorial) of the FEM method are derived with the same form of a generalized eigenvalue equation. Techniques to realize the Dirichlet or Neumann boundary condition and adaptive mesh generation are briefly discussed. General-purposed efficient codes are then developed to calculate a rib waveguide and two slanted-angle polarization converters made of III-V (InGaAsP) materials.

In Chapter 4, we propose general design procedures for slanted-angle polarization converters by normalizing geometric waveguide parameters. Various possible geometries and materials for designing polarization rotating waveguides are analyzed and compared. Merits of SOI polarization rotator with asymmetric external waveguiding layer are elaborated. In addition to normalized design charts, we present a simple empirical design formula and give the range of validity. Finally, the half-beat length variation and the single-mode condition are studied.

In Chapter 5, we analyze the fabrication tolerance and the wavelength insensitivity of novel SOI polarization rotators. Fabricated sample devices and experimental results are described in this chapter.

In Chapter 6, we revisit SOI PR designs with full-vectorial mixed-element beam-propagation method. Anisotropic perfectly-matched-layer boundary condition is incorporated into BPM programs and its efficiency is confirmed with both on- and off-axis Gaussian beam propagation in free space and waveguides. To reliably predict power exchange characteristics, we study the unitarity of full-vectorial FE-BPM. After the feasibility and accuracy of our BPM codes are confirmed, the polarization conversion and power exchange in a SOI polarization converter are analyzed. Validation of analytical formula of polarization conversion efficiency is examined with numerical calculations. Finally, measurement results for the fabricated devices are compared with theoretical predictions.

Chapter 7 studies bending characteristics of asymmetric SOI polarization converters using the conformal mapping technique. Two bending directions are analyzed for features such as optical-axis rotation angle, maximum polarization conversion, radiation loss and transition loss to straight waveguides.

Chapter 8 mainly focuses on loss and coupling issues associated with SOI polarization converters. Butt-coupling to single-mode fibers and input/output rib waveguides, parallel coupling of identical PRs, and a tapered single-mode SOI rib waveguide are analyzed.

Finally, we draw conclusions and present topics of future importance in Chapter 9.

Chapter 2

Background

The objective of this chapter is to provide a brief yet complete introduction to the historic evolution of passive polarization rotator (PR) designs and the silicon-on-insulator (SOI) technology. The general operation principle of asymmetrical passive polarization converters and advantages of silicon photonics will also be thoroughly studied.

2.1 Passive Polarization Rotators

As optical fiber systems evolve to higher data rates, the importance of polarization control and manipulation steadily increases. Recently, there have been increasing interests in the analysis of polarization converters for its significant importance in optical guided-wave devices that require polarization diversity and polarization control. Existing polarization rotators (PR) are cataloged into active and passive devices: the former can be achieved by either electro-optic [11, 12] or photoelastic [13, 14] effects, which introduce some material anisotropy and therefore coupling between differently polarized modes; while the latter generally employ asymmetric geometry such as longitudinally-periodic perturbation structures [15–20] or bending waveguides [21–27] that can be fabricated more easily.

2.1.1 Longitudinally-Periodic Passive Polarization Rotator

Passive polarization converters employ the idea that hybrid modes can experience an exchange of power between polarization states due to the presence of junctions, tapers, bends, or other discontinuities and asymmetries. Shani [15] reported the first experimental demonstration of such a device using periodic asymmetric-loaded rib waveguides illustrated in Fig. 2.1(a). Here, the asymmetric transverse-cross-section introduces perturbation in the primary waveguide axes, and the longitudinal-periodical loading allows coherent accumulation of converted polarization. Shani himself was uncertain about the operating mechanism but suggested that it could probably be a coherent (codirectional) scattering effect due to the asymmetric periodic index loading. Mertens [28] tried to explain this phenomenon with the theory of hybrid supermodes. However, we will give a better explanation in detail in Section 2.1.3.

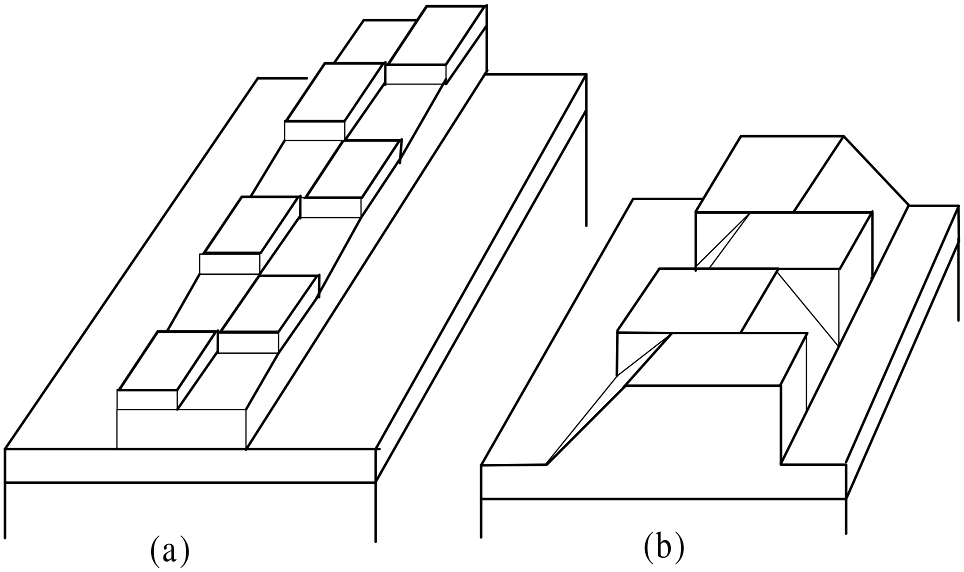

Figure 2.1: Longitudinally-periodic passive polarization rotator: (a) periodically-loaded asymmetric rib waveguides; and (b) periodic angled-facet rib waveguides.

Based on the same mechanism, Heidrich [16, 17] demonstrated a similar passive polarization mode converter with constant 45° rotation, $7025\mu m$ length and 3dB excess loss, by using a periodic laterally-tilted InP/GaInAsP rib waveguide on a stepped substrate, and simulated the conversion effect using both scalar and vectorial 2-D finite difference methods (FDM). Later, with the aid of coupled mode theory (CMT) and beam propagation method (BPM) simulations, van der Tol [18, 19] fabricated a 0.9mm-long and 0.3dB-excess-loss InGaAsP polarization converter configured as Fig. 2.1(b), which contains ten periodic sections of asymmetric angled-facet rib waveguides. Since then, a variety of authors have numerically studied periodically-loaded asymmetric polarization converters by the coupled-mode theory (CMT) analysis [29, 30], vectorial finite-difference method (FDM) [17], finite-difference beam-propagation method (FD-BPM) [18, 19, 31, 32], finite-difference time-domain (FDTD) method [33, 34], multimode analysis method [35], and vectorial finite-element beam-propagation method (FE-BPM) [36].

2.1.2 Single-Section Passive Polarization Rotator

All passive polarization rotators with longitudinally-periodic perturbation structure suffer from high coupling loss at waveguide junctions between adjacent sections; moreover, production process of such long multi-section devices is rather difficult. With coupled mode theory and full-vectorial finite-element perturbation analysis, Mertens [28, 37, 38] found in a buried strip waveguide the degeneracy and strong coupling between hybrid TM_{11} and TE_{21} supermodes, leading to a strong polarization conversion in a configuration free of longitudinally-periodic perturbation. Full vectorial simulation tools were used for the waveguide design in order to avoid unwanted mode coupling [28]. However, polarization conversion was achieved between high-order hybrid supermodes, which limits the application of Mertens' device since most guided-wave systems require single-mode operation so as to reduce power losses from coupling into high-order modes. In addition, the strip waveguide structure [38] displayed in Fig. 2.2(a) has quite thin guiding-layer thickness ($h = 0.15\mu$m, $d = 0.34\mu$m) compared to its width ($W = 1.5 \sim 3.5\mu$m), which demands very precise control in the vertical direction and also leads to very poor coupling to square waveguides or circular fibers.

With the aid of a three-dimensional finite-element propagation method (FE-BPM) [39], Tzolov and Fontaine [40] proposed a longitudinally-invariant passive polarization converter using the slanted-angle rib waveguide as illustrated in Fig. 2.2(b), which is easy to fabricate and has low excess loss. Huang [41, 42] experimentally demonstrated such a single-segment

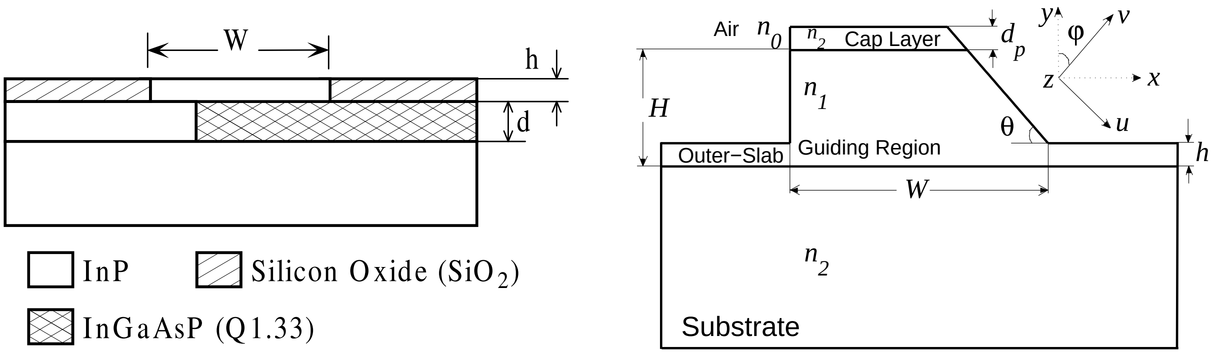

(a) (b)

Figure 2.2: Single-section passive polarization rotator: (a) strip-loaded slab waveguide; and (b) slanted-angle rib waveguide.

polarization rotator with 720μm device length, 1.25dB/mm propagation loss and 96% maximum polarization conversion on GaAs/AlGaAs material. For InP/InGaAsP waveguides, Zhu [9, 43–45] fabricated a 200μm single-section passive PR with 1.7dB insertion loss and 80% polarization conversion ratio. By completely eliminating both outer-slab layers, El-Refaei and Yevick [46–48] improved the fabrication tolerance of the device, and obtained -16dB conversion efficiency and 0.02 dB loss for a 330μm device.

Single-section passive polarization rotator employing slanted-angle rib waveguide has attracted much attention during the past few years because of its simple geometry, compact dimension (compared with longitudinal-periodic structures), and small insertion loss. Numerous simulations of slanted-facet polarization rotators with III-V materials (InGaAsP, AlGaAs, etc.) have been performed using the finite-difference method (FDM) [41–44, 46–48], finite-element-method (FEM) mode solver [18, 19, 31, 40, 49–51], finite element beam propagation method (FE-BPM) [52], finite-element based genetic algorithm [53], and vectorial boundary-element method (V-BEM) [54]. However, weakly-guiding polarization rotators based on low-refractive-index-contrast III-V materials possess large bending radius, large curvature losses, large device size and large radiation loss to substrate or outer-slab region. Therefore, this thesis focuses on introducing the silicon-on-insulator (SOI) material system with extremely high index-contrast into the design and fabrication of single-section passive polarization rotators.

2.1.3 Operation Principle

The principle of passive polarization converters is based on the well-known property of birefringent optical devices [55, 56]: the field propagates at different speeds along the fast- and slow-axis (also called ordinary- and extraordinary-axis) of the optical-axes (u, v). In a waveguide with constant birefringence, the time delay between the two polarized eigenstates is given by [57]

$$\Delta t = \frac{L}{\nu_1} - \frac{L}{\nu_2} \tag{2.1}$$

where L is the propagation distance, ν_1 and ν_2 are the phase velocities along the slow- and fast-axis, respectively. Since the phase velocity is related to the propagation constant by $\nu = \frac{\omega}{\beta}$ [58], the phase delay is expressed as

$$\vartheta = \omega\Delta t = L(\beta_1 - \beta_2) \tag{2.2}$$

where $\omega = 2\pi f$ is the angular frequency, f is the frequency, $\beta = n_{eff}k_0$ is the propagation constant, n_{eff} is the effective index, $k_0 = \omega\sqrt{\varepsilon_0\mu_0} = 2\pi/\lambda$ is the free-space wavenumber, λ is the free space wavelength, and the subscripts 1 and 2 are for the two fundamental polarization states along the slow- and fast-axis, respectively. When the phase delay becomes 180°, the propagating distance is called the half-beat length L_π which is defined as

$$L_\pi = \frac{\pi}{\beta_1 - \beta_2} = \frac{\pi}{(n_{eff1} - n_{eff2})\,k_0} = \frac{\lambda}{2\,(n_{eff1} - n_{eff2})} \tag{2.3}$$

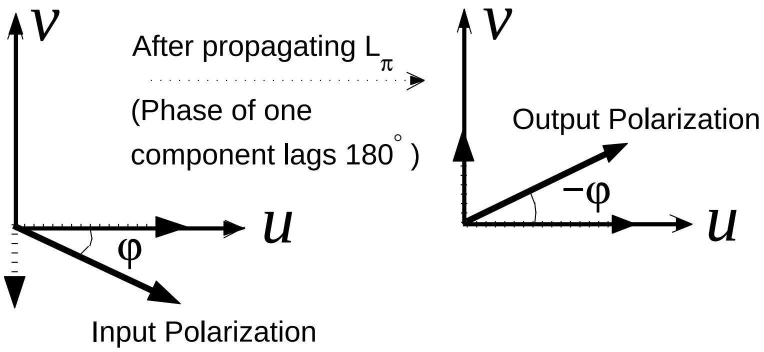

Figure 2.3: Polarization rotation in birefringent device.

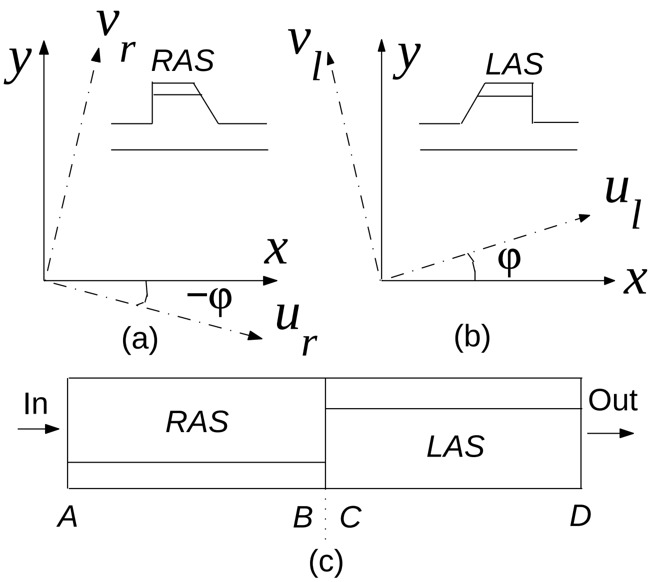

Figure 2.4: Operation principle of the periodic-loaded asymmetric waveguide: (a) optical-axes (u_r, v_r) of subsection right-asymmetric-structure (RAS); (b) optical-axes (u_l, v_l) of subsection left-asymmetric-structure (LAS); and (c) one section of a periodically-loaded waveguide with both RAS and LAS subsections.

As illustrated in Fig. 2.3, a linearly-polarized light can be decomposed into two components along the optical-axes. After the distance of a half-beat length, the phase of one component is 180° later than that of the other. Therefore, *if a linearly-polarized light is launched into a longitudinally-invariant birefringent waveguide with an angle φ (counter-clockwise) to one optical axis, after propagating a half-beat length, the output polarization makes an angle of $-\varphi$ (clock-wise) with respect to the same axis.*

As shown in Figs. 2.1 and 2.4, a longitudinally-periodic structure consists of N sections, and each section contains two subsections — a right-asymmetric-structure (RAS) and a left-asymmetric-structure (LAS). Taking the periodic angled-facet structure of Fig. 2.1(b) as an example, the subsection is RAS if the angled-facet locates on the right-hand side, and LAS if the slanted angle locates to the left. The optical axes are denoted as (u_r, v_r) for RAS and (u_l, v_l) for LAS. The asymmetry of the waveguide cross-section causes the optical-axes to rotate by an angle φ [59] around a fixed Cartesian coordinate system, where

x- and y-axes are along the horizontal and vertical directions, respectively. The optical axes in RAS and LAS are rotated by an angle $-\varphi$ (clockwise) and φ (counter-clockwise), respectively.

Polarization Angle	RAS input (A)	RAS ouput (B)	
to (u_r, v_r)	φ	$-\varphi$	
		LAS input (C)	LAS output (D)
to (u_l, v_l)		-3φ	3φ
to (x, y)	0	-2φ	4φ

Table 2.1: Evolution of the polarization angle in a section of the periodically-loaded asymmetric waveguides.

For simplicity, we consider an x-polarized input light and match the length of each subsection to its half-beat length. At the RAS input port (point A in Fig. 2.4(c)), the light is positioned at an angle φ with respect to the optical-axes (u_r, v_r) of RAS subsection, thus at the RAS output the polarization state is rotated to $-\varphi$ regarding to (u_r, v_r) and -2φ to the x-axis. Similar effect happens in the LAS subsection, however, at the LAS input port, the light is positioned at an angle -3φ to (u_l, v_l) since the optical-axes of LAS and RAS form an angle of -2φ. Consequently, at the LAS output port, the polarization is located 3φ regarding to the optical-axes of LAS (u_l, v_l), and 4φ regarding to the x-axis. This procedure is well illustrated in Table 2.1.

As a result, one subsection (RAS or LAS) rotates the polarization state by 2φ and one section (a pair of RAS and LAS) rotates the polarization by 4φ. Even though the optical-axis of each subsection is only slightly perturbed, i.e., φ is very small, for sufficient N periodically-loaded sections, the final polarization is rotated by $4N\varphi$ which could be about 90°, indicating a complete TE ↔ TM conversion. In this case, the eigenmodes are *weakly hybridized* and the polarization rotation is accumulated along the propagation direction.

If the optical-axis of an asymmetric-loaded waveguide is rotated by $\varphi = 45°$, we see from the above analysis that the polarization will be rotated by $2\varphi = 90°$ after a half-beat length. Such a waveguide thus can be employed as a single-section passive TE ↔ TM polarization converter. Its eigenmodes are *strongly hybridized* with comparable TE and TM components and similar field distributions.

2.2 Silicon-on-Insulator Technology

As mentioned in Section 2.1.2, the silicon-on-insulator (SOI) material will be employed in this thesis to design single-section polarization rotators for its many unique optical characteristics compared to III-V semiconductor counterparts. Hence, in this section, a brief introduction to silicon photonics, SOI waveguides and their advantages will be presented.

2.2.1 Silicon Photonics

Silicon photonic components employ the optical properties of crystalline silicon, a Group IV dielectric material. The impetus for Silicon Photonics [57,60–68] came from optoelectronics — integration of optics and electronics on the same chip, since optoelectronic integrated circuits (OEIC) exhibit better performances compared with separated optical and electrical chips. Silicon-based optoelectronic systems have the potential to incorporate with silicon electronics and to achieve high integration densities. The significant importance of silicon in future optoelectronics comes from the following factors:

1. Silicon-on-Insulator (SOI) material [69, 70] has become a main platform for both photonics and VLSI CMOS electronics, with fully compatible processing procedures;
2. Si-based optoelectronic integrated circuits have economic advantages;
3. compared with III-V semiconductors, silicon has better crystal perfection, better native oxide, and superior thermal and mechanical properties;
4. SOI CMOS circuits have reduced parasitics and latch-up that enable high-speed at low power [66];
5. strong optical-confinement of SOI waveguides enables low-loss and compact device-size.

At present, most optoelectronic devices employ III-V semiconductor materials such as AlGaAs/GaAs and InGaAsP/InP, because the indirect bandgap and low carrier mobility in silicon were once obvious obstacles to optoelectronic applications. However, there are now methods to surmount these problems. Modulation doping enhances higher mobilities [64]; optical and electrical properties can be transformed by adopting heterostructures or by tetragonal distortion of the lattice due to coherent strain [64, 66, 71]. Emitting, guiding, detecting, modulating, and switching infrared light ($\lambda > 1.2\mu$m) have been realized in silicon [64]. Waveguiding structures have been demonstrated in Si/Si$_{1-x}$Ge$_x$, silicon-on-silicon (SOS), silicon-on-insulator (SOI) and silicon-germanium-on-silicon (SGOS) materials [64]. Therefore it is reasonable to foresee more silicon-based photonic components since the performance of Si-based OEIC could eventually surpass that of III-V OEIC in some areas.

2.2.2 SOI Waveguides

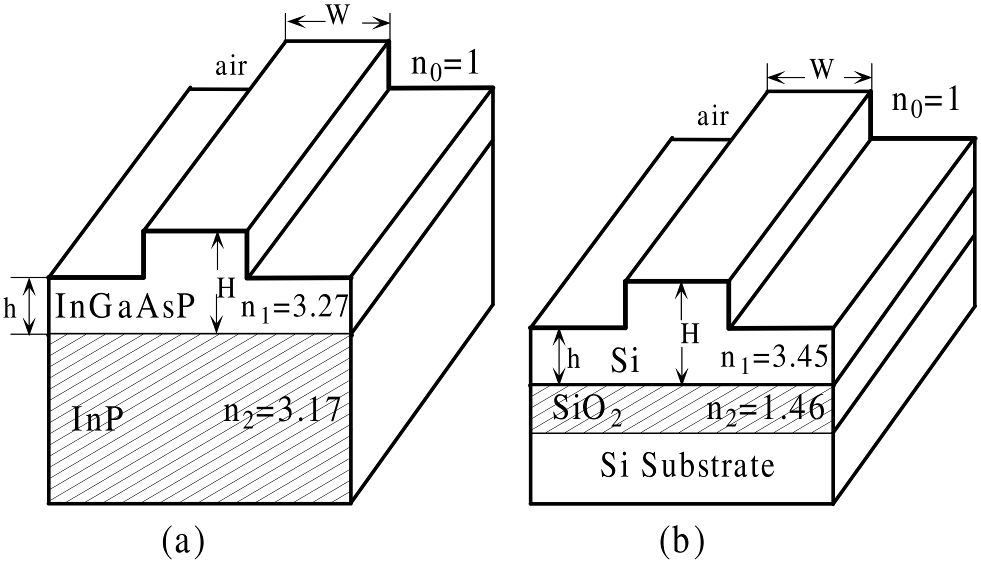

Figure 2.5: Rib waveguides: (a) III-V rib waveguide; and (b) SOI rib waveguide

The unique optical performance of SOI mainly comes from its very large refractive index difference. As shown in Fig. 2.5, the index contrast between guiding- and insulator- regions in SOI is $\Delta = (n_1^2 - n_2^2)/n_1^2 = 82\%$, where $n_1 = 3.45$ and $n_2 = 1.46$ are the refractive indices of silicon and silicon-oxide, respectively; while that of waveguides made of conventional III-V semiconductors such as AlGaAs/GaAs and InGaAsP/InP is generally as small as

$\Delta = 0.01\%$ to 2%. The large index-contrast in SOI leads to very strong optical confinement and hence some unique challenges as well as opportunities. The strong optical confinement enables close waveguide spacing, thin substrate layer, and small bending radius; therefore very compact and large-scale OEIC can be made through SOI technology. The overall dimension of SOI waveguides is comparable to that of CMOS devices and the fabrication procedure is fully compatible with VLSI technology.

SOI was originally difficult to work with because of the poor silicon-epitaxial-layer quality from manufacturing processes [72]; however, with developing technologies, nowadays there are many sophisticated techniques to fabricate low-defect SOI wafers. These technologies [68, 70] include Silicon-on-sapphire (SOS), separation by implantation of oxygen (SIMOX) [73, 74] or nitride (SIMNI), bond-and-etchback SOI (BE-SOI), and smart cut, etc., which enable SOI wafers to be widely used for commercial high speed CMOS and DRAM chips. Over the past few years, SOI has been applied to many guided-wave optical devices and circuits, such as high-speed modulators [75, 76], photodetectors [77], directional couplers [78], Mach-Zehnder Interferometer (MZI) switches [79, 80], Corner-Mirrors and T-Branches [81], Y-Branches [82], Bragg gratings [83,84], star couplers [85], multimode interference (MMI) coupler [86], and arrayed-waveguide gratings (AWG) [72, 87–89].

2.2.3 Single-Mode Condition of SOI Rib Waveguides

In many optical communication systems, single mode propagation is a prerequisite. There once existed a conventional opinion suggesting that, due to the large refractive index step, SOI waveguides must have submicron transverse cross-section for mono-mode propagation; as a result, the coupling efficiency to optical fibers is extremely poor [66]. This misconception came from the analysis of single mode condition for slab waveguides with analytical means or effective index method (EIM) using simplified approximations. It prevented SOI from being applied to photonics until Soref [90] demonstrated that the slab criteria is not essential for single mode propagation in rib waveguides. With mode-matching and beam-propagation methods, Soref derived the approximate single-mode (SM) criteria for the SOI rib waveguide of Fig. 2.5(b) as

$$\frac{W}{H} \leq const + \frac{h/H}{\sqrt{1-(h/H)^2}} \ , \ \text{with } const = 0.3 \tag{2.4}$$

subject to the conditions of slightly-etching ($\frac{h}{H} \geq 0.5$) and large cross-section ($H > \frac{1}{\sqrt{n_1^2 - n_2^2}}$). The symbols W, H and h denote the rib width, rib height and thickness of the outer slab layer, respectively. Schmidtchen [91], Zinke [92], Fisher [93,94], Rickman [95,96] and Tang [74, 97] experimentally fabricated single-mode photonic devices with transverse dimensions comparable to optical wavelength or the spot-size of single-mode fibers (SMF) and therefore realized efficient coupling into SMF. These experimental results are in favor of the hypothesis that single mode behavior exists with certain multi-micron rib dimensions even when planar SOI waveguides of similar dimensions are multi-mode. Although Pogossian [98] claimed a stronger criterion for designing large cross-section single-mode SOI rib waveguides, his expression is based on data [95] *predicted* from Soref's original formula [90] rather than obtained experimentally as he took for granted. The correctness and accuracy of Soref's formula have been numerically verified with effective index method (EIM) [99] and finite-difference beam-propagation method (FD-BPM) [99, 100]. Moreover, single-mode condition analysis has recently been carried out for trapezoidal cross-section [99, 101], small cross-section and deeply-etched [102] SOI rib waveguides.

Chapter 3

Finite Element Mode Solvers

This thesis focuses on applying the extremely-high-index-contrast Silicon-on-Insulator (SOI) material system to the design and fabrication of single-section passive polarization rotators. For this purpose, we have developed a general-purposed software package including Full-Vectorial Finite Element Method (FV-FEM) and Finite-Element Beam-Propagation Method (FE-BPM) based on mixed triangular elements.

This chapter explains why a full-vectorial FEM scheme is mandatory in Section 3.1, and describes complete algorithms of various FEM formulations for solving eigenmodes in Section 3.2. Sections 3.3 and 3.4 provide an overview of boundary conditions and adaptive meshes. Section 3.5 presents simulation results of III-V rib waveguides and polarization converters in order to confirm program accuracy and efficiency. Numerical algorithms associated with FE-BPM procedures will be discussed in detail in Chapter 6.

3.1 Why FEM and Full-Vectorial Scheme

The Finite Element Method (FEM), also called the Finite Element Analysis (FEA), is an efficient numerical technique to obtain approximate solutions to boundary-value problems in mathematical physics [103, 104]. FEM originated in structural analysis during 1940s', and has been widely employed in analyzing stress, torsion, heat transfer, fluid flow, and so on. Silvester [105–109] introduced FEM into the field of electromagnetics in 1968, since when it has been applied to diverse areas such as semiconductor devices, optical waveguides, and radiation and absorption of electromagnetic waves. Based on the variational principle, basic procedures of the FEM include: obtaining functionals (variational expressions) from corresponding differential equations, dividing interested regions into small elements, constructing interpolation model for each element, assembling all elements' contributions to the global system, and finally solving the global-matrix problems.

There are two topics of interest in optical waveguide analyses: one is to find the eigenmodes that a waveguide supports (*Guided-mode analysis*); and the other is to study the field propagation along the waveguide (*Beam-propagation analysis*). The algorithms associated with the former are the major topic of Section 3.2, while the details for the latter will be presented in Section 6.1. Although FEM has been widely employed in the guided-mode analysis, it has not been applied to the beam propagation analysis until recently. Numerical techniques [110–115] other than FEM [105–109, 116–125] involved in the guided-mode analysis include: the Finite Difference Method (FDM) [126–129], the Finite-Difference Time-Domain method (FDTD) [33, 34, 130], the Method of Lines (MoL) [131], the Method of Moments (MoM) [132], and the Boundary Element Method (BEM) [54, 133, 134], which are conceptually simpler. Prior to the Finite-Element Beam-Propagation Method (FE-BPM) [135–140], there existed various Beam Propagation Method (BPM) [141–146] algorithms such as the Fast-Fourier-Transform Beam-Propagation Method (FFT-BPM) [147], the Finite-Difference Time-Domain Beam-Propagation Method (FDTD-BPM) [148] and the Finite-Difference Beam-Propagation Method (FD-BPM) [129].

Presently, commercially available software packages for photonics design, such as the APSS [1], OptiWave [2], BeamProp [3], FIMMWAVE/FIMMPROP [4] and Empire FDTD [5], are mostly based on Finite-Difference (FD) algorithms (i.e., FDM, FDTD, FD-BPM, FDTD-BPM, and FD-based Coupled Mode Theory (CMT) etc.), which use rectangular grids such that nodes are positioned at intersections of orthogonal straight lines. However, these grids are not suitable for problems with curved boundaries/interfaces, arbitrary cross-sections,

---

[1] Apollo Photonics, Inc., Hamilton, Ontario, Canada. http://www.apollophoton.com

[2] Optiwave Corporation, Ottawa, Ontario, Canada. http://www.optiwave.com

[3] RSoft Design Group, Inc., Ossining, New York, United States. http://www.rsoftdesign.com

[4] Photon Design, Oxford, United Kingdom. http://www.photond.com/products/fimmwave.htm. Note that a FEM eigenmode solver has recently been incorporated in FIMMWAVE-4.00 of late 2004.

[5] IMST GmbH, Kamp-Lintfort, Germany. http://www.empire.de and http://www.imst.com

large index-contrasts and steep field-variations. In contrast, the systematic generality of FEM makes it possible to construct a general-purposed computer program for a wide range of problems. In FEM, the field region is divided into subregions (elements), which could be of different shapes — triangular, rectangular, curvilinear, ring, or infinite. In addition, mixed element shapes and/or different base-function orders can be used simultaneously in one problem, depending on required computational accuracy. Moreover, for both mode solver and propagation analysis, nonuniform unstructured meshes [149–151] and adaptive meshing procedures can be employed to significantly improve the accuracy and efficiency of FEM programs. FEM makes it possible to take into consideration the discontinuity of refractive indices, no matter how complicated the geometrical profile is [39]. Furthermore, FEM scheme can be established not only by the variational method but also by the Galerkin method (a weighted residual method) or the least-squares-method (LSM) [122], so FEM can still be used even though a variational principle does not exist or cannot be identified. These unique features are not available in FFT- and FD- algorithms. In conclusion, FEM is a more general, powerful, versatile, accurate and efficient strategy for problems involving complicated geometries, inhomogeneous media, anisotropic dielectrics, lossy materials, strongly-guiding structures and polarization-dependent waveguides. Due to faster and faster CPU processors and enormously-increasing available computer memory, undoubtedly more and more electromagnetic field problems will be solved routinely with FEM techniques in the future.

Specifically, for asymmetric slanted-angle polarization rotators, when finite-difference (FD) techniques are applied, numerical instabilities, inaccuracy and inefficiency could appear as a consequence. Huang [41] reported unstable simulations for GaAs/AlGaAs polarization rotators, and had to improve the stability by adopting a cumbersome procedure in which the large refractive discontinuities were smoothed over a specific scale length. In another calculation on InP/InGaAsP polarization rotators by Zhu et. al., large field errors were presented at the high-contrast waveguide corners and interfaces, as clearly observed from Fig. 1 of [43]. El-Rafaei and Yevick [47] pointed out the relative inefficiency of FDM which has to be trivially programmed for slanted-angle rib waveguides. Moreover, FDM can give rise to spurious modes [152, 153] and has trouble in getting accurate results at dielectric corners and interfaces [154, 155]. The main challenges in simulating an angled-facet polarization converter come from the strongly-hybrid nature of its eigenmodes and the tilted facet which is difficult to be precisely discretized by regular orthogonal FDM grids. Although a structure-related finite-difference beam-propagation method for the analysis of photonics structures with sloped sides has been proposed by Djurdjevic et al. [156], it is restricted to the scalar analysis thus polarization effects cannot be characterized. Similarly, a semi-vectorial finite-difference scheme has been recently proposed by Xia and Yu [157] for the purpose of titled interfaces; however, the staircase approximation still exists and the programming implementation is more complicated. With a modified finite-difference formula employing the imaginary axis method and proper enforcement of boundary conditions [158], the quantization error generated in the staircase approximation can be reduced (but cannot be completely eliminated) at the cost of increasing CPU time and memory usages. On the contrary, with FEM an arbitrary angled-facet can be represented exactly and precisely with much less degree of freedoms.

When silicon-on-insulator (SOI) material substitutes III-V semiconductors in passive polarization rotators, another challenge arises — the extremely high refractive-index-contrast makes it difficult to precisely simulate SOI devices with traditional techniques [159]. In addition, the silicon oxide (SiO_2) layer is usually quite thin (0.2 to 0.4μm by SIMOX process [96] and $> 0.4\mu$m [73] such as 1μm for large cross-section waveguides), while the silicon guiding layer could be as thick as several micron-meters. This further imposes difficulty for finite-difference simulations, and in fact very poor and unreliable results have been observed with FDM-based commercial software. In this case, highly versatile finite-element (FE) techniques seem to be a best choice, since a non-uniform unstructured mesh together with adaptive refinement could easily overcome the above difficulties without an appreciable increase in either CPU time or memory usage.

Due to the strong modal hybridness in highly-birefringent photonic waveguides or optical fibers [39], a full-vectorial (FV) scheme is prerequisite. Scalar calculations ignore polarization effects and semi-vectorial algorithms neglect the coupling between transverse polarizations, hence neither could correctly predict the different TM→TE and TE→TM conversion-efficiency and excess-loss behavior. A proper polarization converter design thus should rely on a FV-calculation so as to correctly describe polarization conversion behaviors and avoid unwanted mode couplings [28] as well.

3.2 FEM Eigenmode Solvers

In this section, starting with scalar analysis, general procedures for finite-element guided-mode analysis are first introduced, while semi-vectorial and full-vectorial algorithms are subsequently described. We have developed general-purposed computer codes for all these schemes; however, our main focus is the FV-FEM which is a necessity for studying polarization behaviors in asymmetric angled-facet rib waveguides. With FV-FEM eigenmode solver, general design procedures for slanted-angle polarization rotators are obtained in Chapter 4. The analysis of polarization conversion along the propagation direction using the beam-propagation scheme will then be shown in Chapter 6.

3.2.1 Scalar FEM

The Scalar Finite Element Method (SC-FEM) is the simplest formulation with good numerical efficiency and without spurious modes [124]. It neglects the polarization effects by setting transverse derivatives of the relative permittivity to zero [125]. The scalar wave equation for a homogenous waveguide is obtained from the Maxwell's equation as

$$\nabla^2\psi - \frac{1}{\mu\varepsilon}\frac{\partial^2}{\partial t^2}\psi = 0 \tag{3.1}$$

where t is the time, $\varepsilon = \varepsilon_0\varepsilon_r$ and $\mu = \mu_0\mu_r$ are the permittivity and permeability of the dielectric material, respectively. The free-space permittivity and permeability are $\varepsilon_0 = 8.854187817 \times 10^{-12}$ F/m and $\mu_0 = 4\pi \times 10^{-7}$ H/m, respectively. The relative permeability μ_r is 1 for non-magnetic materials. In the Cartesian coordinates, the Laplacian operator ∇^2 is

$$\nabla^2 = \frac{\partial^2}{\partial x^2} + \frac{\partial^2}{\partial y^2} + \frac{\partial^2}{\partial z^2} \tag{3.2}$$

Substituting a solution of the form

$$\psi = \phi(x, y)\exp(-j\beta z)\exp(j\omega t) \tag{3.3}$$

and noting that

$$\frac{\partial}{\partial z} = -j\beta, \text{ and } \frac{\partial}{\partial t} = j\omega \tag{3.4}$$

the Helmholtz equation is derived as

$$\frac{\partial^2\phi}{\partial x^2}+\frac{\partial^2\phi}{\partial y^2}+(n^2k_0^2-\beta^2)\phi=0 \tag{3.5}$$

where $\omega=2\pi f$ is the angular frequency, f is the frequency, $\beta=n_{eff}k_0$ is the propagation constant, n_{eff} is the effective index, $k_0=\omega\sqrt{\varepsilon_0\mu_0}=2\pi/\lambda$ is the free-space wavenumber, λ is the free-space wavelength, and $n=\sqrt{\mu_r\varepsilon_r}$ is the refractive index of the material. The Euler's Equation $L\phi=g$ [110, 111] has a source excitation $g=0$ and a self-adjoint positive-definite operator $L=\frac{\partial^2}{\partial x^2}+\frac{\partial^2}{\partial y^2}+(n^2k_0^2-\beta^2)$ therefore its functional is

$$I(\phi)=\langle L\phi,\phi\rangle-\langle\phi,g\rangle-\langle g,\phi\rangle=\frac{1}{2}\iint\left[\left(\frac{\partial\phi}{\partial x}\right)^2+\left(\frac{\partial\phi}{\partial y}\right)^2-(n^2k_0^2-\beta^2)\phi^2\right]\mathrm{d}x\,\mathrm{d}y \tag{3.6}$$

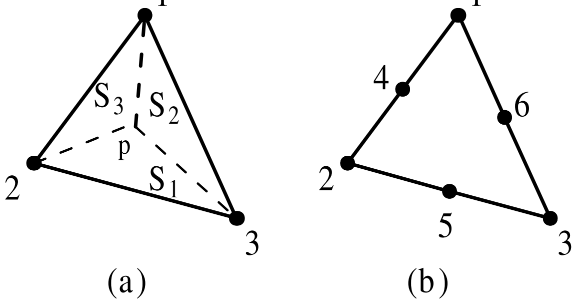

Figure 3.1: Nodal triangular elements: (a) linear triangle; and (b) quadratic triangle.

After discretizing the waveguide into small elements (rectangular or triangular, etc.), the functional can be written as $I(\phi)=\sum_e I^e(\phi^e)$ and the field anywhere in an element is

$$\phi(x,y)=\sum_i N_i^e\phi_i^e=[N]^T\{\phi\}_e \tag{3.7}$$

where e is the element, i (or j) denotes a node, ϕ_i^e and N_i^e are the field and polynomial (base vector) associated with node i, respectively, and $\{\phi\}_e$ and $[N]$ are the field vector and the shape function for element e, respectively. For a linear triangular element as shown in

Fig. 3.1(a), the shape function $[N]$ is given by [105–108, 125]

$$[N] = \begin{bmatrix} L_1 \\ L_2 \\ L_3 \end{bmatrix} = \begin{bmatrix} 1 & 1 & 1 \\ x_1 & x_2 & x_3 \\ y_1 & y_2 & y_3 \end{bmatrix}^{-1} \begin{bmatrix} 1 \\ x \\ y \end{bmatrix} \tag{3.8}$$

where (x, y) is a point inside the triangle formed by vertices (x_1, y_1), (x_2, y_2) and (x_3, y_3), and L is the so-called *local coordinates* or *area coordinates*. Higher order basis function for triangles can be derived in terms of local coordinates from the Silvester Polynomial [108, 109, 119–121]. In particular, for a quadratic triangle as Fig. 3.1(b) it is given by

$$N_i = L_i(2L_i - 1), i = 1, 2, 3; \text{ and } N_4 = 4L_1L_2, N_5 = 4L_2L_3, N_6 = 4L_3L_1 \tag{3.9}$$

Applying the Rayleigh-Ritz, Galerkin or Least-Squares-Method (LSM) procedure [110, 111, 122], from $\dfrac{\partial I(\phi)}{\partial \phi} = 0$, we obtain the eigenvalue equation for scalar FEM analysis

$$[K]\{\phi\} - \beta^2[M]\{\phi\} = \{0\} \tag{3.10}$$

where

$$[K] = \sum_e [K^e], \text{ with } K^e_{ij} = \iint\limits_{\Omega_e} \left(n^2 k_0^2 N^e_i N^e_j - \frac{\partial N^e_i}{\partial x}\frac{\partial N^e_j}{\partial x} - \frac{\partial N^e_i}{\partial y}\frac{\partial N^e_j}{\partial y} \right) \mathrm{d}x\, \mathrm{d}y \tag{3.11}$$

$$[M] = \sum_e [M^e], \text{ with } M^e_{ij} = \iint\limits_{\Omega_e} \left(N^e_i N^e_j \right) \mathrm{d}x\, \mathrm{d}y \tag{3.12}$$

Here Ω_e is the region of each element, $\sum_e$ means assembling the contribution of all elements, $[K^e]$ and $[M^e]$ are the elementary matrices, $[K]$ and $[M]$ are the global matrices, and $\{0\}$ is a null vector. The assembling of the global matrix $[K]$ [110, 111, 119–121, 123, 125] from the elementary matrix $[K]^e$ is obtained according to the pattern

$$K_{pq} = \sum_e K^e_{ij}, \text{ for all } p = n(i, e),\ q = n(j, e) \tag{3.13}$$

where $n(i, e)$ denotes the global numbering for the i-th node in the triangle e, and $\sum$ means considering contribution from all elements. In the SC-FEM eigenvalue problem, both global matrices $[K]$ and $[M]$ are sparse and symmetric.

3.2.2 Semi-Vectorial FEM

The semi-vectorial (SV-) analysis can be employed to calculate different polarization modes [126, 160], although the coupling between transverse polarizations is neglected [125, 129]. Based on the transverse-electric (TE) or transverse-magnetic (TM) field the semi-vectorial Helmholtz wave equation is [140, 161–163]

$$\frac{\partial}{\partial x}\left(p_x\frac{\partial \phi}{\partial x}\right)+\frac{\partial}{\partial y}\left(p_y\frac{\partial \phi}{\partial y}\right)+\frac{\partial}{\partial z}\left(p_z\frac{\partial \phi}{\partial z}\right)+k_0^2 q\phi=0 \tag{3.14}$$

where

$$\phi=E_x,\ p_x=n_x^2/n_z^2,\ p_y=p_z=1,\ q=n_x^2,\ \text{for Quasi-TE } (E^x) \text{ modes} \tag{3.15}$$

$$\phi=H_x,\ p_x=1/n_y^2,\ p_y=1/n_z^2,\ p_z=1/n_y^2,\ q=1,\ \text{for Quasi-TM } (E^y) \text{ modes} \tag{3.16}$$

Here E_x and H_x are the electric- and magnetic-field along the x-direction, respectively, and n_x, n_y, and n_z are the refractive indices of the material in the x, y, and z directions, respectively. Other components of the electromagnetic fields are

$$\begin{aligned}\text{for Quasi TE mode: } E_y\equiv 0,\ E_z=-\frac{j}{\beta}\frac{\partial E_x}{\partial x},\ H_x=\frac{1}{\omega\mu\beta}\frac{\partial^2 E_x}{\partial x\partial y},\\ H_y=\frac{1}{\omega\mu\beta}\left(\beta^2E_x-\frac{\partial^2 E_x}{\partial x\partial y}\right),\ H_z=\frac{j}{\omega\mu}\frac{\partial E_x}{\partial y}\end{aligned} \tag{3.17}$$

$$\begin{aligned}\text{for Quasi TM mode: } E_x=-\frac{1}{\omega\varepsilon\beta}\frac{\partial^2 H_x}{\partial x\partial y},\ E_y=\frac{1}{\omega\varepsilon\beta}\left(\frac{\partial^2 H_x}{\partial x^2}-\beta^2H_x\right),\\ E_z=\frac{j}{\omega\varepsilon}\frac{\partial H_x}{\partial y},\ H_y\equiv 0,\ H_z=-\frac{j}{\beta}\frac{\partial H_x}{\partial x}\end{aligned} \tag{3.18}$$

By applying similar procedures as in the scalar analysis, the eigenvalue equation for Semi-Vectorial Finite Element Method (SV-FEM) is derived as

$$[K]\{\phi\}-\beta^2[M]\{\phi\}=\{0\} \tag{3.19}$$

where

$$[K] = \sum_e \iint_{\Omega_e} \left[qk_0^2\{N\}\{N\}^T-p_x\{N_x\}\{N_x\}^T-p_y\{N_y\}\{N_y\}^T\right]\mathrm{d}x\,\mathrm{d}y \tag{3.20}$$

$$[M] = \sum_e \iint_{\Omega_e} p_z\{N\}\{N\}^T\mathrm{d}x\,\mathrm{d}y \tag{3.21}$$

Here the derivatives of the shape function are defined by $\{N_x\} \equiv \partial\{N\}/\partial x$ and $\{N_y\} \equiv \partial\{N\}/\partial y$. In the SV-FEM eigenvalue problem, both global matrices $[K]$ and $[M]$ are sparse and symmetric.

3.2.3 Full-Vectorial FEM

To study strongly-hybrid modes, polarization exchange or polarization-dependent propagation, a full-vectorial (FV-) analysis is mandatory. For an optical waveguide with arbitrary cross-section Ω in the transverse xy-plane, the full-vectorial Helmholtz wave equation is derived from Maxwell equations with an implied time dependence $\exp(j\omega t)$:

$$\nabla \times ([p]\,\nabla \times \phi) - k_0^2\,[q]\,\phi = 0 \tag{3.22}$$

where ϕ is either the electric field $\boldsymbol{E}$ or the magnetic field $\boldsymbol{H}$. The del (nabla) operator is

$$\nabla = \boldsymbol{i}_x \frac{\partial}{\partial x} + \boldsymbol{i}_y \frac{\partial}{\partial y} + \boldsymbol{i}_z \frac{\partial}{\partial z} = \nabla_t + \boldsymbol{i}_z \frac{\partial}{\partial z} \tag{3.23}$$

Here $\boldsymbol{i}_x$, $\boldsymbol{i}_y$, $\boldsymbol{i}_z$ are the unit vectors along x, y and z directions, respectively, and ∇_t is the transversal del operator. The dielectric constant of the material is associated with the permittivity- and permeability- tensors $[p]$ and $[q]$ by

$$[p] = \begin{bmatrix} p_x & 0 & 0 \\ 0 & p_y & 0 \\ 0 & 0 & p_z \end{bmatrix} \text{ and } [q] = \begin{bmatrix} q_x & 0 & 0 \\ 0 & q_y & 0 \\ 0 & 0 & q_z \end{bmatrix} \tag{3.24}$$

$$p_x = p_y = p_z = 1,\ q_x = n_x^2,\ q_y = n_y^2,\ q_z = n_z^2,\ \text{for } \phi = \boldsymbol{E} \tag{3.25}$$

$$q_x = q_y = q_z = 1,\ p_x = 1/n_x^2,\ p_y = 1/n_y^2,\ p_z = 1/n_z^2,\ \text{for } \phi = \boldsymbol{H} \tag{3.26}$$

where n_x, n_y, and n_z are the refractive indices in the x, y, and z directions, respectively.

The functional for Eq.(3.22) is given by

$$F = \iint\limits_{\Omega} \left[(\nabla \times \phi)^* \cdot ([p]\,\nabla \times \phi) - k_0^2\,[q]\,\phi^* \cdot \phi \right] \mathrm{d}x\,\mathrm{d}y \tag{3.27}$$

with the asterisk denoting complex conjugate.

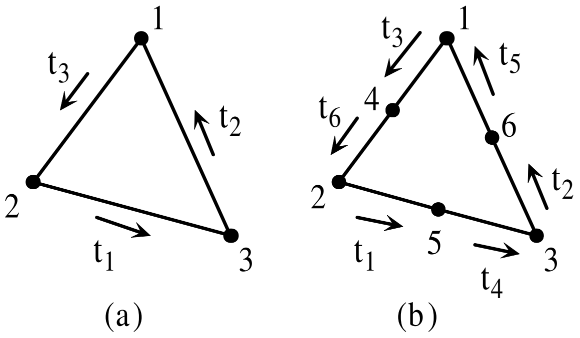

Figure 3.2: Mixed-interpolation-type triangular elements: (a) constant tangential and linear nodal (CT-LN) element (1st order mixed element); and (b) linear tangential and quadratic nodal (LT-QN) element (2nd order mixed element).

In our FV-FEM programs, we employ the hybrid elements of Fig. 3.2 instead of traditional nodal elements. Full-vectorial analysis with nodal triangles has encountered the appearance of spurious modes [118–121, 124, 164–166] that do not satisfy the divergence-free condition ($\nabla \cdot \boldsymbol{B} = 0$ for magnetic fields and $\nabla \cdot \boldsymbol{D} = 0$ for electric fields). Several methods, such as the penalty method [167–170], implicitly implying the divergence-free constraint into the FEM functional [116, 171], or solving eigenvalue equation in a subspace defined by the divergence constraint [172], have been proposed to eliminate non-physical solutions at the expenses of increased algorithm complexity and decreased computation accuracy or efficiency. In contrast, edge basis functions [119–121, 173, 174] not only enforce tangential continuity of fields across element edges but also allow discontinuity of normal field components; therefore, they work well for inhomogeneous problems and also suppress spurious modes. Moreover, since each edge belongs to no more than two elements, global matrices for edge elements have greater sparsity than those for nodal elements [121].

Dividing waveguide cross-section into a number of mixed-interpolation-type triangular elements, we expand the transverse components ϕ_x, ϕ_y and longitudinal component ϕ_z in each element as

$$\phi = \begin{bmatrix} \phi_x \\ \phi_y \\ \phi_z \end{bmatrix} = \begin{bmatrix} \{U\}^T\{\phi_t\}_e \\ \{V\}^T\{\phi_t\}_e \\ j\{N\}^T\{\phi_z\}_e \end{bmatrix} e^{j\beta z} \tag{3.28}$$

where $\{\phi_t\}_e$ is the transverse tangential field, and $\{\phi_z\}_e$ is the longitudinal nodal field of each element. The scalar-based shape function {N} in terms of local coordinates has been shown in Eqs. (3.8) and (3.9) for linear and quadratic nodal triangles, respectively. The vector-based shape functions {U} and {V} for Nédélec edge elements [175–178] are given by [117, 119, 120, 179–181]

$$\boldsymbol{i}_x\{U\} + \boldsymbol{i}_y\{V\} = \begin{bmatrix} |\nabla_t L_3|_1(L_1\nabla_t L_2 - L_2\nabla_t L_1) \\ |\nabla_t L_1|_2(L_2\nabla_t L_3 - L_3\nabla_t L_2) \\ |\nabla_t L_2|_3(L_3\nabla_t L_1 - L_1\nabla_t L_3) \end{bmatrix} \tag{3.29}$$

for constant tangential and linear nodal (CT-LN) elements, and

$$\boldsymbol{i}_x\{U\} + \boldsymbol{i}_y\{V\} = \begin{bmatrix} |\nabla_t L_3|_1(L_1\nabla_t L_2) \\ |\nabla_t L_1|_2(L_2\nabla_t L_3) \\ |\nabla_t L_2|_3(L_3\nabla_t L_1) \\ |\nabla_t L_3|_2(L_2\nabla_t L_1) \\ |\nabla_t L_1|_3(L_3\nabla_t L_2) \\ |\nabla_t L_2|_1(L_1\nabla_t L_3) \end{bmatrix} \tag{3.30}$$

for linear tangential and quadratic nodal (LT-QN) elements.

Dividing the field ϕ into transverse and longitudinal components [52, 121] ϕ_t and ϕ_z, i.e., $\phi = \phi_t + \boldsymbol{i}_z\phi_z$, we separate the full-vectorial wave equation Eq.(3.22) into two parts:

$$\nabla_t \times (p_z \nabla_t \times \phi_t) + \frac{\partial}{\partial z}\{[p]_t\,(\nabla_t\phi_z - \frac{\partial}{\partial z}\phi_t)\} - k_0^2\,[q]_t\,\phi_t = 0 \tag{3.31}$$

$$\nabla_t \times \left[\{[p]_t\,(\nabla_t\phi_z - \frac{\partial}{\partial z}\phi_t)\} \times \boldsymbol{i}_z\right] - k_0^2 q_z \phi_z \boldsymbol{i}_z = 0 \tag{3.32}$$

where the transverse permittivity and permeability are

$$[p]_t = \begin{bmatrix} p_x & 0 \\ 0 & p_y \end{bmatrix} \text{ and } [q]_t = \begin{bmatrix} q_x & 0 \\ 0 & q_y \end{bmatrix} \tag{3.33}$$

By applying the Galerkin procedure and noting the relationship of Eq.(3.4), propagation constants and eigenmodes can be obtained from the following set of equations:

$$\beta^2[M_{tt}]\{\phi_t\} + \beta[M_{tz}]\{\phi_z\} - [K_{tt}]\{\phi_t\} = \{0\} \tag{3.34}$$

$$\beta[M_{zt}]\{\phi_t\} + [M_{zz}]\{\phi_z\} = \{0\} \tag{3.35}$$

where

$$
\begin{aligned}
[K_{tt}] = \sum_e \iint\limits_{\Omega_e} [& q_x k_0^2 \{U\}\{U\}^T + q_y k_0^2 \{V\}\{V\}^T - p_z \{U_y\}\{U_y\}^T \\
& - p_z \{V_x\}\{V_x\}^T + p_z \{U_y\}\{V_x\}^T + p_z \{V_x\}\{U_y\}^T] \, \mathrm{d}x \, \mathrm{d}y
\end{aligned}
\tag{3.36}
$$

$$
[M_{tt}] = \sum_e \iint\limits_{\Omega_e} [p_y \{U\}\{U\}^T + p_x \{V\}\{V\}^T] \, \mathrm{d}x \, \mathrm{d}y \tag{3.37}
$$

$$
[M_{tz}] = [M_{zt}]^T = \sum_e \iint\limits_{\Omega_e} [p_y \{U\}\{N_x\}^T + p_x \{V\}\{N_y\}^T] \, \mathrm{d}x \, \mathrm{d}y \tag{3.38}
$$

$$
[M_{zz}] = \sum_e \iint\limits_{\Omega_e} [p_y \{N_x\}\{N_x\}^T + p_x \{N_y\}\{N_y\}^T - q_z k_0^2 \{N\}\{N\}^T] \, \mathrm{d}x \, \mathrm{d}y \tag{3.39}
$$

Here the derivatives of shape functions are defined by $\{N_x\} = \partial\{N\}/\partial x$, $\{N_y\} = \partial\{N\}/\partial y$, $\{U_x\} = \partial\{U\}/\partial x$, $\{U_y\} = \partial\{U\}/\partial y$, $\{V_x\} = \partial\{V\}/\partial x$, $\{V_y\} = \partial\{V\}/\partial y$, respectively.

Eliminating the longitudinal component ϕ_z from the Eqs.(3.34) and (3.35), we obtain

$$
[K_{tt}]\{\phi_t\} = \beta^2 \left([M_{tt}] + [M_{tz}][M_{zz}]^{-1}[M_{zt}]\right) \{\phi_t\} \tag{3.40}
$$

The solution of generalized eigenvalue problem Eq.(3.40) directly yields the propagation constants and corresponding field distributions along the transverse plane. However, there is a major disadvantage with Eq.(3.40), that is, the inverse procedure for large-scale matrix $[M_{zz}]$ not only takes tremendous memory usage and CPU time but also destroys the matrix sparsity such that efficient sparse eigenvalue solvers cannot be employed.

However, if we perform a substitution $\phi_z = \beta \phi_z'$ into Eqs.(3.34) and (3.35), the generalized eigenvalue problem for the FV-FEM analysis is transformed to

$$
[K]\{\phi\} - \beta^2 [M]\{\phi\} = \{0\} \tag{3.41}
$$

with

$$
[K] = \begin{bmatrix} [K_{tt}] & [0] \\ [0] & [0] \end{bmatrix}, \; [M] = \begin{bmatrix} [M_{tt}] & [Mtz] \\ [Mzt] & [Mzz] \end{bmatrix} \text{ and } \{\phi\} = \left\{ \begin{array}{c} \phi_t \\ \phi_z' \end{array} \right\} \tag{3.42}
$$

Noting the z-dependence $\exp\{-j\beta z\}$ of the field, the above transformation is actually $\phi_z = j\dfrac{\partial}{\partial z}\phi'_z$ [182]. It is worth pointing out that this idea maintains the dominant transverse fields unchanged and is similar to the variable transformation ($\phi'_x = \beta\phi_x, \phi'_y = \beta\phi_y, \phi'_z = -j\phi_z$) that Lee, Sun and Cendes [119, 121, 174, 183] proposed to obtain the first FV-FEM eigenvalue equation directly solving propagation constant for a given wavelength.

The generalized eigenvalue problem Eq. (3.41) can be solved via numerous methods [58, 122] such as the variational techniques, method of moments, projection methods, or iterative techniques [184–186]. However, since both matrices in Eq. (3.41) are *sparse* and *symmetric*, one can easily solve it with widely available sparse-matrix solvers [121, 122] such as the implicitly restarted Arnoldi algorithm [127, 187] in the ARPACK library [6].

Although the eigenvalue equation of Eq.(3.41) has both electric- and magnetic-field formulations, i.e., $\boldsymbol{E}$- and $\boldsymbol{H}$-formulations, the latter is generally preferred since all three magnetic components are naturally continuous across dielectric interfaces [167, 188].

3.3 Boundary Condition

We have generalized scalar (SC-), semi-vectorial (SV-) and full-vectorial (FV-) analyses into the same form of eigenvalue problem $([K] - \beta^2[M])\{\phi\} = \{0\}$, as evident from Eqs.(3.10), (3.19) and (3.41), therefore the same eigenvalue solver could be applied for all these three analyses. However, the boundary condition (BC), which constraints field or potential value at material interfaces and calculation boundaries, has to be considered in advance.

A proper boundary condition directly affects the numerical efficiency and accuracy. In the guided-mode analysis, Dirichlet- or Neumann- BC is generally considered, which forces unknown field or its derivative to be zero at computation boundaries. For the $\boldsymbol{E}$-formulation, the Dirichlet- and Neumann- BC indicate a perfect electrical conductor (PEC) and a perfect magnetic conductor (PMC), respectively; and vice versa for the $\boldsymbol{H}$-formulation. The Neumann BC is the simplest in FEM analysis since the line integrations around boundaries vanish during the derivation procedure of functionals [119, 121, 189], therefore no specific action needs to be taken and the generalized matrix equation remains unchanged. However, for the Dirichlet BC, special care has to be given.

---

[6] ARPACK stands for ARnoldi PACKage. [Online] http://www.caam.rice.edu/software/ARPACK/

Dirichlet boundary condition requires boundary fields to be zero, i.e, $\phi_i = 0$ where i denotes an unknown node or edge at the boundaries. A common way to impose Dirichlet BC to the standard eigenvalue problem $[K]\{\phi\} = \beta^2\{\phi\}$ is to set the whole i-th row and i-th column of matrix $[K]$ to zero but remain matrix element K_{ii} unchanged [119,121], or set K_{ii} to an extremely large value such as 10^{70} while keeping all other elements [119]. Kawano [125] applied Dirichlet BC for the generalized eigenvalue problem $([K] - \beta^2[M])\{\phi\} = \{0\}$ by performing the same action on matrix $[M]$, i.e.,

$$\left(\begin{bmatrix} K_{11} & ... & 0 & ... & K_{1n} \\ & & \vdots & & \\ 0... & 0... & K_{ii} & ...0 & ...0 \\ & & \vdots & & \\ K_{n1} & ... & 0 & ... & K_{nn} \end{bmatrix} - \beta^2 \begin{bmatrix} M_{11} & ... & 0 & ... & M_{1n} \\ & & \vdots & & \\ 0... & 0... & M_{ii} & ...0 & ...0 \\ & & \vdots & & \\ M_{n1} & ... & 0 & ... & M_{nn} \end{bmatrix}\right) \begin{pmatrix} \phi_1 \\ \vdots \\ \phi_i \\ \vdots \\ \phi_n \end{pmatrix} = \{0\} \quad (3.43)$$

This simple way does not destroy the matrix sparsity and symmetry; however, it is not sufficient to force $\phi_i = 0$, since the i-th equation now becomes $(K_{ii} - \beta^2 M_{ii})\{\phi_i\} = 0$ in which ϕ_i could be any value if K_{ii} happens to equal to $\beta^2 M_{ii}$. Thus we employ a more robust method by removing the known ϕ_i and corresponding i-th row and i-th column from both matrices, that is, only equations related to unknown interiors are kept. Meanwhile, the matrix dimension is reduced by the number of fixed boundary values, leading to reduced calculation time for eigenvalues. The advantage of solving the system formed by only interior unknowns is especially pronounced for dense mesh discretization.

3.4 Adaptive Mesh Generation

The accuracy of FEM eigenmode solvers and propagation techniques strongly depends on a proper discretization of the problem domain. Generally, better numerical accuracy can be obtained with refined denser meshes at the cost of increased CPU time and memory usage. On the other hand, improper excessive refinement for insignificant regions wastes computer resources and degrades computing speed. Therefore, adaptive automatic mesh generations [149–151] are highly desired.

One major advantage of finite element techniques is that both orthogonal structured

FDM-type grids and general unstructured meshes can be employed, resulting in high versatility. Unstructured meshes can be either uniform or non-uniform. The non-uniform meshes can provide required degree of discretization in regions where necessary, and meanwhile avoid extraordinary fine discretization in places where not required.

Generally, two techniques — *adaptive mesh refinement* and *adaptive remeshing* — are involved in the adaptive mesh generation [190]. In the former technique, new nodes are continually added but no existing nodes are removed; while in the latter method, completely new mesh is adaptively generated according to previous calculations [190]. These allow one to obtain more accurate solutions without systematic increases in the number of unknowns and the size of matrices. In the adaptive mesh generation, individual element weights (*local weights*, also called *local errors*) are used to judge which elements should be refined. The refinement continues until a stopping criterion is met, resulting in a final mesh with local weights of the same order of magnitude. The adaptive mesh generation generally employs the Delaunay algorithm [150, 191, 192] and includes the following procedures [193, 194]: generating a coarse mesh, determining local weights for each element, refining selected elements, moving nodes and swapping edges to improve element shapes, and renumbering nodes and edges to reduce matrix bandwidth.

The efficiency of adaptive mesh generation largely depends on the *error function* related to each element. A most common error function is the *density function*, which weights the field amplitude or the field variation of each element in the problem domain. Fernandez [190] used user-defined Gaussian and sinusoidal density functions to evaluate element weights. Other alternatives for local estimates include: the “local error problem” algorithm, complete residual method, field residual algorithm [195], field gradient method [192], and nodal perturbation scheme [196]. The difference between results obtained by meshes of different orders has also been adopted as the density function [193, 194, 197]. For a two-dimensional discretization, the individual element weight w_e is related to the density function $f(x, y)$ as

$$w_e = \iint_e f(x, y)\mathrm{d}x\,\mathrm{d}y \tag{3.44}$$

If each weight is equal to a threshold w_{th}, the total weight should be $w = \sum_e w_e = N_e w_{th}$, where N_e is the number of elements. The threshold weight therefore can be set as $w_{th} = \dfrac{w}{N_e}$, and all the elements with weight larger than the threshold should be refined.

3.5 Numerical Accuracy and Efficiency

The convergence of our FEM programs has been verified earlier [198]. Here we confirm the numerical accuracy and efficiency with examples on rib waveguides [126,193,194,199] and asymmetric slanted-angle polarization rotators made of III-V semiconductors [40,41,49].

3.5.1 FEM Simulation for III-V Rib Waveguide

We consider the III-V rib waveguide as shown in Fig. 2.5(a) with refractive indices $n_1 = 3.44$ (GaAs), $n_2 = 3.34$ (GaAlAs), and rib height, rib width and thickness of outer-slab $(H, W, h) = (1.3, 2, 0.2)$ μm, respectively. The effective index of its fundamental mode (n_{eff1}) was found to converge to about 3.3885 by adaptive meshing procedures (maximum 800 second-order hybrid elements) with various density functions [193,194]. We first simulate the waveguide with the full-matrix problem Eq. (3.40) using a structured mesh as Fig. 3.3(a), whose connectivity is of the finite-difference type [149,151]. For 29×22 grid points, i.e., 1176 first-order mixed triangles with 638 nodes and 1813 edges, the effective index is calculated as 3.388305. The structured mesh for 2nd-order mixed elements with 17×16 grid points, i.e., 480 triangles with 1023 nodal unknowns and 1502 tangential unknowns, results in an effective index of 3.388288. The calculation for these small systems with full-matrix solver takes more than three hours on a Linux machine with Pentium-III 733MHz CPU and 512M memory. We hereafter improve the calculation using the equivalent sparse-matrix problem of Eq. (3.41) and a non-uniform unstructured mesh [149,151] as Fig. 3.3(b). The effective index 3.3885572 is obtained in only three minutes for 2620 second-order hybrid elements with 1358 nodes and 3977 edges. Various results for the effective-index of the rib waveguide are compared in Table 3.1, where the normalized propagation constant

$$b = \frac{n_{eff}^2 - n_2^2}{n_1^2 - n_2^2} \tag{3.45}$$

is also calculated for a more comprehensive comparison.

Fig. 3.4 displays the field plot of calculated fundamental modes, which penetrates deep into the substrate region due to the low-index contrast of the material system. The two lowest-order modes are TE- and TM-modes, with polarizations along the x- and y-axes of the Cartesian coordinate, respectively.

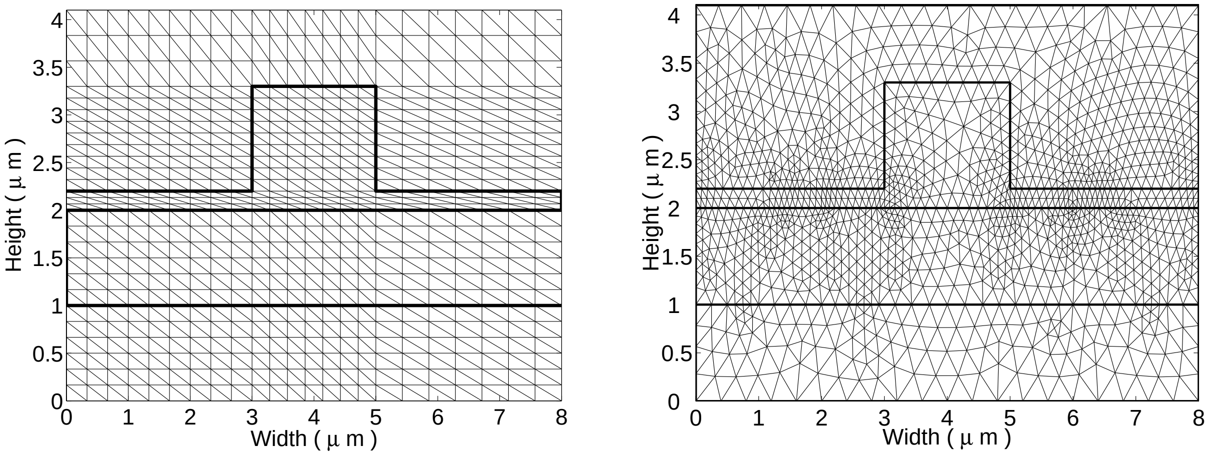

(a)

(b)

Figure 3.3: Meshes for the rib waveguide: (a) structured mesh; and (b) unstructured mesh.

	n_{eff}	error	b	error
Converged value in [193, 194]; $\leq$ 800 second-order mixed-element	3.3885	0%	0.48132	0%
Structured mesh: 29 × 22 grids, 1st order hybrid elements	3.388305	0.00575%	0.479368	0.40495%
Structured mesh: 17 × 16 grids, 2nd order hybrid elements	3.388288	0.00626%	0.479196	0.44025%
Unstructured mesh: 2620 second-order hybrid elements	3.3885572	0.00169%	0.481888	0.11885%
Unstructured mesh: 7072 second-order hybrid elements	3.388671	0.00502%	0.483022	0.35441%

Table 3.1: Comparison of calculated effective-index values for the III-V rib waveguide in [193,194].

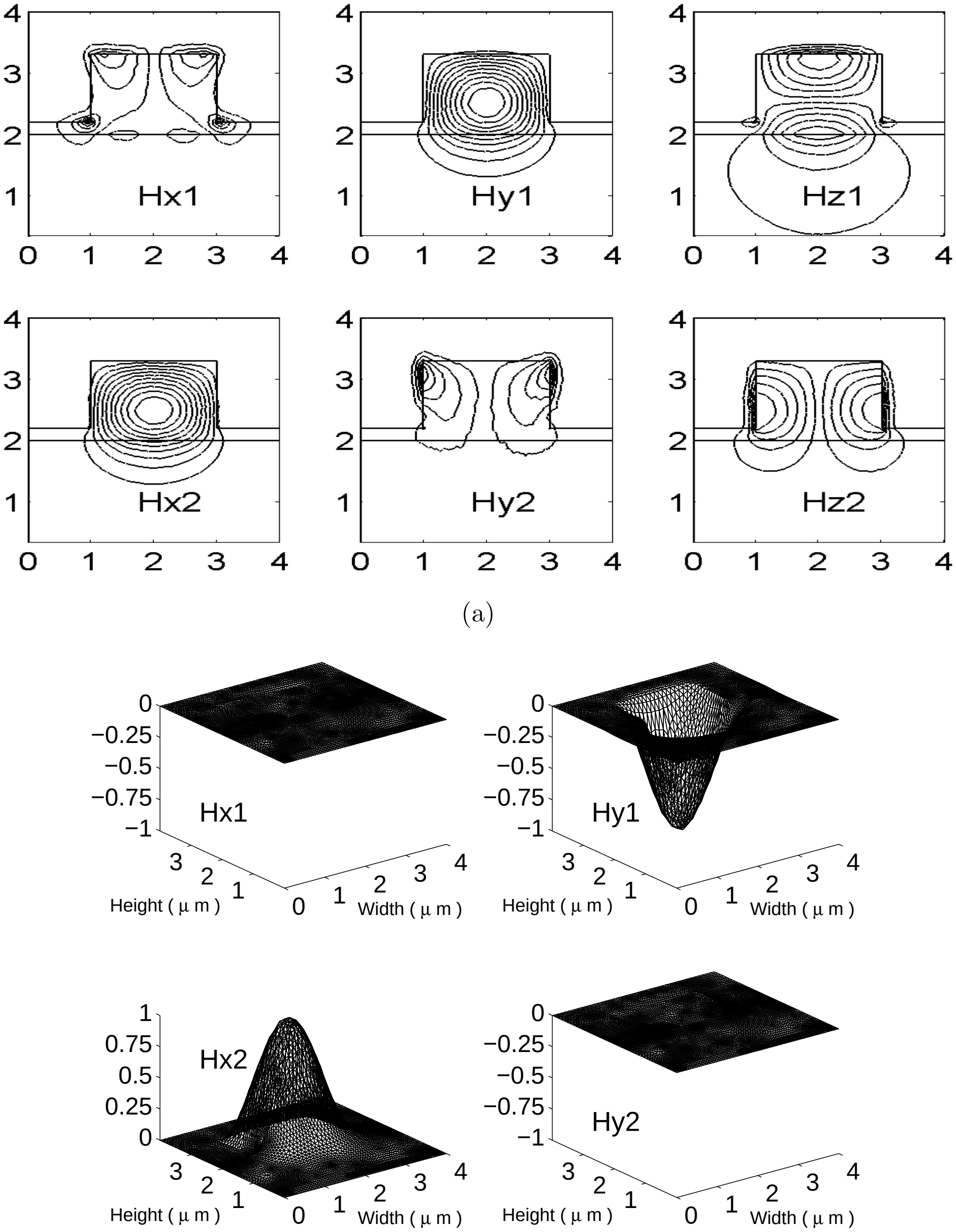

(a)

(b)

Figure 3.4: Lowest two eigenmodes of a III-V rib waveguide: (a) two-dimensional (2D) contour graph; and (b) three-dimensional (3D) surface plot. The first is a TE-like mode with dominant field H_y and non-dominant field H_x; while the second is a TM-like mode with dominant field H_x and non-dominant field H_y.

3.5.2 FEM for III-V Polarization Rotators

Using FEM eigenmode solvers, we show here results for asymmetric slanted-angle III-V polarization rotators with the geometry of Fig. 2.2(b). First, a GaAs/AlGaAs device [41, 49, 50] is considered, which has a base rib width $W = 2.5\mu$m, rib height $H = 1.3\mu$m, symmetric outer-slab layer thickness $h = h_r = 0.1\mu$m, angle of titled-facet $\theta = 52°$, and refractive indices $n_1 = 3.370$ (GaAs) and $n_2 = 3.324$ ($\mathrm{Al_{0.1}Ga_{0.9}As}$). Various available discretizations are shown in Fig. 3.5. One can easily find that the FDM grids Fig. 3.5(a) and structured FEM mesh Fig. 3.5(b) have trouble in precisely representing the refractive indices around the slanted facet, therefore the staircase approximation inevitably limits the calculation accuracy. The nonuniform unstructured mesh of Fig. 3.5(c) obtained by Delaunay triangulation [150, 191, 192] avoids this difficulty but wastes many triangles in regions with small field amplitude or variation. The adaptive mesh Fig. 3.5(d), which takes into account the field amplitude or variation, focuses elements to places of significance, therefore both accuracy and efficiency are guaranteed.

From a structured FEM mesh with 31 × 28 grids (Fig. 3.5(b), 1620 first-order mixed elements, 868 nodes and 2487 edges), the lowest fundamental mode of the slanted-angle GaAs/AlGaAs polarization converter is obtained as Fig. 3.6. We observe that the two transverse field components obviously have quite similar distributions and amplitudes, resulting in a 45° optical-axis rotation. However, although the structured mesh of Fig. 3.5(b) may approximately describe the waveguide geometry, calculated field patterns present large error at waveguide interfaces especially the dielectric/air boundary, which is obvious in Fig. 3.6. The same difficulty is inherent in the orthogonal FDM grids of Fig. 3.5(a). Therefore, in calculations hereafter, only the unstructured mesh of Fig. 3.5(c) and the adaptive mesh of Fig. 3.5(d) will be employed for much more accurate results.

Table 3.2 summarizes the results obtained with different meshes. In Table 3.2, CT-LN and LT-QN denote the 1st- and 2nd-order mixed triangular elements as Fig. 3.2 (a) and (b), respectively; N_e, N_p and N_t refer to the total number of triangular elements, nodal points and tangential edges, respectively; n_{eff1} and n_{eff2} are the effective indices of the two lowest-order fundamental polarizations, respectively; and L_π is the half-beat length which converges to 695μm in the FEM analysis. For the same accuracy, the adaptive mesh requires much less elements and less CPU time compared to regular nonuniform unstructured mesh, as is obvious in Table 3.2. The calculated half-beat length value is consistent with the 3D FV-FD-BPM simulation of 667μm (Table 1 of [41]) and nodal FEM analysis of about 730μm (Fig. 6 of [49]). The experimental result is $L_\pi \approx 720\mu$m when the geometric variation is 2° for the slant angle, $\pm 0.1\mu$m for the etch depth, and $\pm 0.2\mu$m for the base width [41]. However, neither [41] nor [49] gave exact values for effective indices, we therefore turn to a similar InP/InGaAsP device in [40] for a better comparison.

Mesh	Order	N_e	N_p	N_t	n_{eff1}	n_{eff2}	$L_\pi(\mu\text{m})$	time(s)
Fig. 3.5(c)	CT-LN	4168	2147	6314	3.325992	3.324862	685.531	127
Fig. 3.5(c)	LT-QN	4168	8461	12628	3.325922	3.324807	694.555	547
Fig. 3.5(d)	LT-QN	2756	1410	8330	3.325961	3.324845	694.489	373

Table 3.2: Comparison of results for the GaAs/AlGaAs slanted-angle polarization rotator in [41, 49, 50].

Tzolov's InP/InGaAsP slanted-angle polarization converter shown in Fig. 2.2(b) has a base rib width $W = 2\mu$m, rib height $H = 1\mu$m, symmetric outer-slab thickness $h = h_r = 0.2\mu$m, cap layer thickness $d_p = 0.2\mu$m, slant angle $\theta = 45°$, and refractive indices $n_1 = 3.4$ (InGaAsP) and $n_2 = 3.27$ (InP) [40, 52]. From an iterative FEM solver [39] with nodal elements, the effective indices are obtained [7] as $n_{eff1} = 3.331684$ and $n_{eff2} = 3.328660$, respectively [8], corresponding to a half-beat length of $L_\pi = 248.0159\mu$m. The results calculated with hybrid-type mixed elements are compared in Table 3.3, based on a Linux (RedHat7) machine with Pentium-III 733MHz CPU and 512M memory (the last calculation in Table 3.3 was executed on an IBM R6000 AIX51 supercomputer with 1.3GHz POWER4 CPUs [9]). All effective indices in Table 3.3 are accurate up to the fourth digit (10^{-4}). Especially, when small number of elements are used [10], our calculation of n_{eff1}, n_{eff2}, and L_π agrees well with Tzolov's value to within 0.00162%, 0.00378%, and 2.37%, respectively.

---

[7] For consistency, the largest effective index is always identified as n_{eff1} throughout this thesis.

[8] Tzolov mistakenly wrote the effective index of one fundamental mode as 3.228660 in [40], which is a obvious mistyping since it is below the lowest refractive index 3.27 of the material system.

[9] http://www.monolith.uwaterloo.ca/hardware.html

[10] Tzolov performed his calculations in [40] at the year 1995. At that time, popular personal computers were only 486 and 586, and memory chips were only 8M, 16M and 32M.

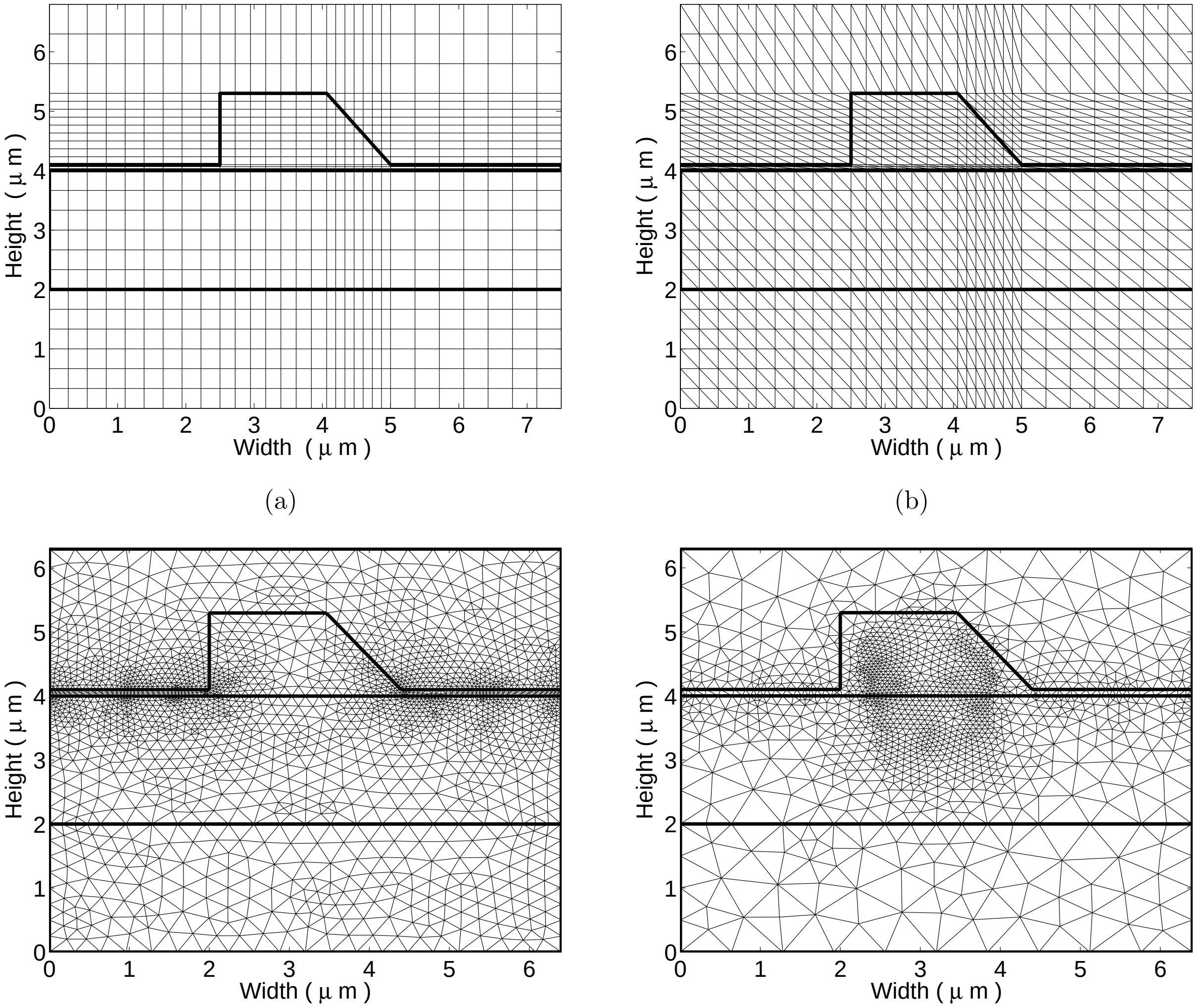

(a) (b) (c) (d)

Figure 3.5: Meshes for the slanted-angle polarization rotator: (a) non-equidistant grids for FDM analysis; (b) structured mesh for FEM analysis; (c) nonuniform unstructured mesh; and (d) nonuniform mesh obtained from adaptive procedure.

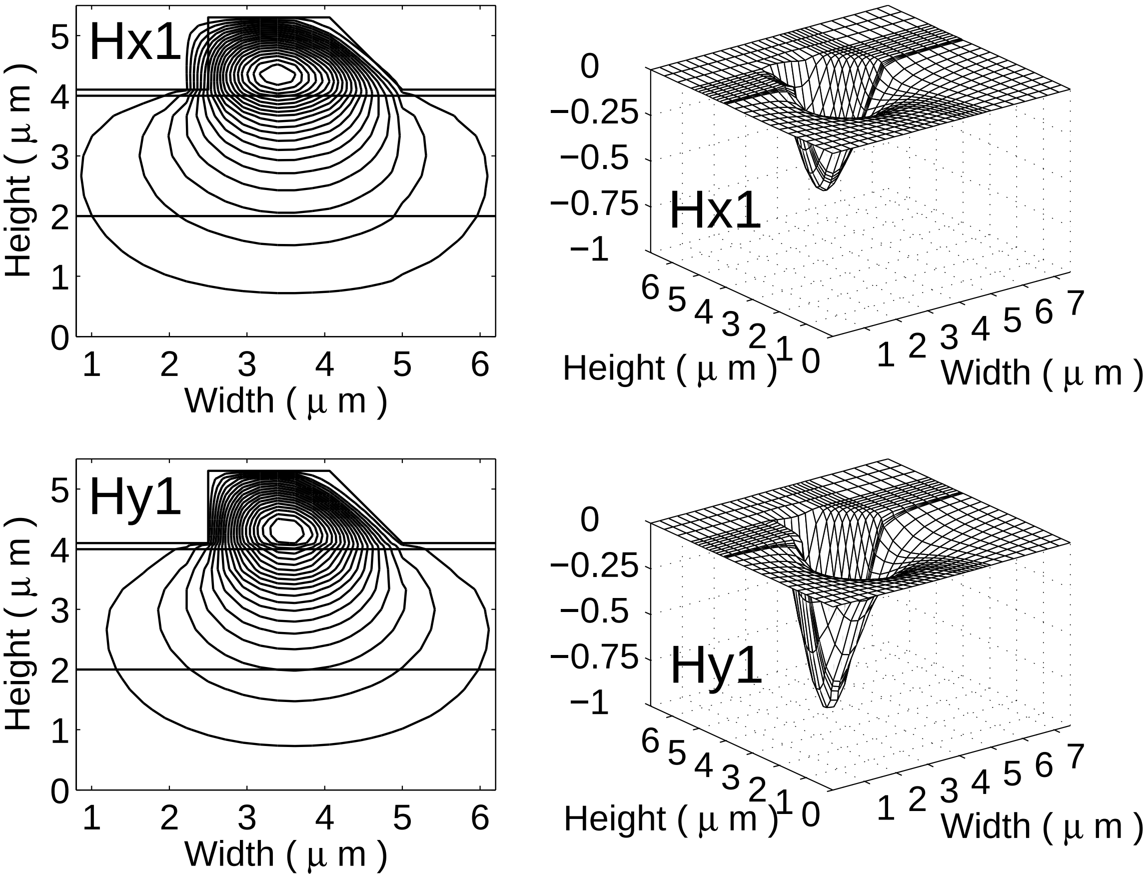

Figure 3.6: Field distribution of the lowest-order fundamental mode of the GaAs/AlGaAs polarization converter in [41, 49, 50] with geometry parameters $W = 2.5\mu\text{m}$, $H = 1.3\mu\text{m}$, $h = h_r = 0.1\mu\text{m}$, $\theta = 52^\circ$, and refractive indices $n_1 = 3.370$ (GaAs) and $n_2 = 3.324$ ($\text{Al}_{0.1}\text{Ga}_{0.9}\text{As}$). These modal plots are obtained with the structured FEM mesh of Fig. 3.5(b) with 31×28 grids and 1620 first-order mixed elements.

The half-beat length is more difficult to be accurately calculated than the effective indices (this point can be well understood from Eq. (2.3) where any small variation in effective indices is greatly amplified since these indices are in the denominator). However, with denser and denser meshes, L_π converges to about 316μm.

Mesh	Order	N_e	N_p	N_t	n_{eff1}	n_{eff2}	$L_\pi(\mu\text{m})$	time(s)
in [40]	/	/	/	/	3.331684	3.328660	248.016	/
Fig. 3.5(b)	LT-QN	646	1365	2010	3.331810	3.328714	242.129	/
Fig. 3.5(c)	LT-QN	830	1717	2546	3.331123	3.328051	252.320	51
Fig. 3.5(c)	LT-QN	3320	6753	10072	3.331534	3.328991	304.736	370
Fig. 3.5(d)	LT-QN	1108	2273	3380	3.331505	3.328931	301.181	122
Fig. 3.5(d)	LT-QN	1846	3749	5594	3.331609	3.329114	310.599	242
Fig. 3.5(d)	LT-QN	3514	7085	10598	3.331630	3.329157	313.362	669
Fig. 3.5(d)	LT-QN	6386	12817	19202	3.331663	3.329209	315.758	745

Table 3.3: Comparison of results for the InP/InGaAsP slanted-angle polarization rotator in [40, 52].

The eigenmode graphs for the InP/InGaAsP polarization converter are plotted in Fig. 3.7. By comparing Figs. 3.6 and 3.7 with Fig. 3.4, we confirm the operation principle of single-section asymmetric polarization rotator: the TE- and TM- components of either fundamental polarization have comparable field amplitude and very similar intensity distributions so that the orthogonal optical axes (c.f. Fig. 2.4) are rotated by 45° regarding to the horizontal and vertical directions.

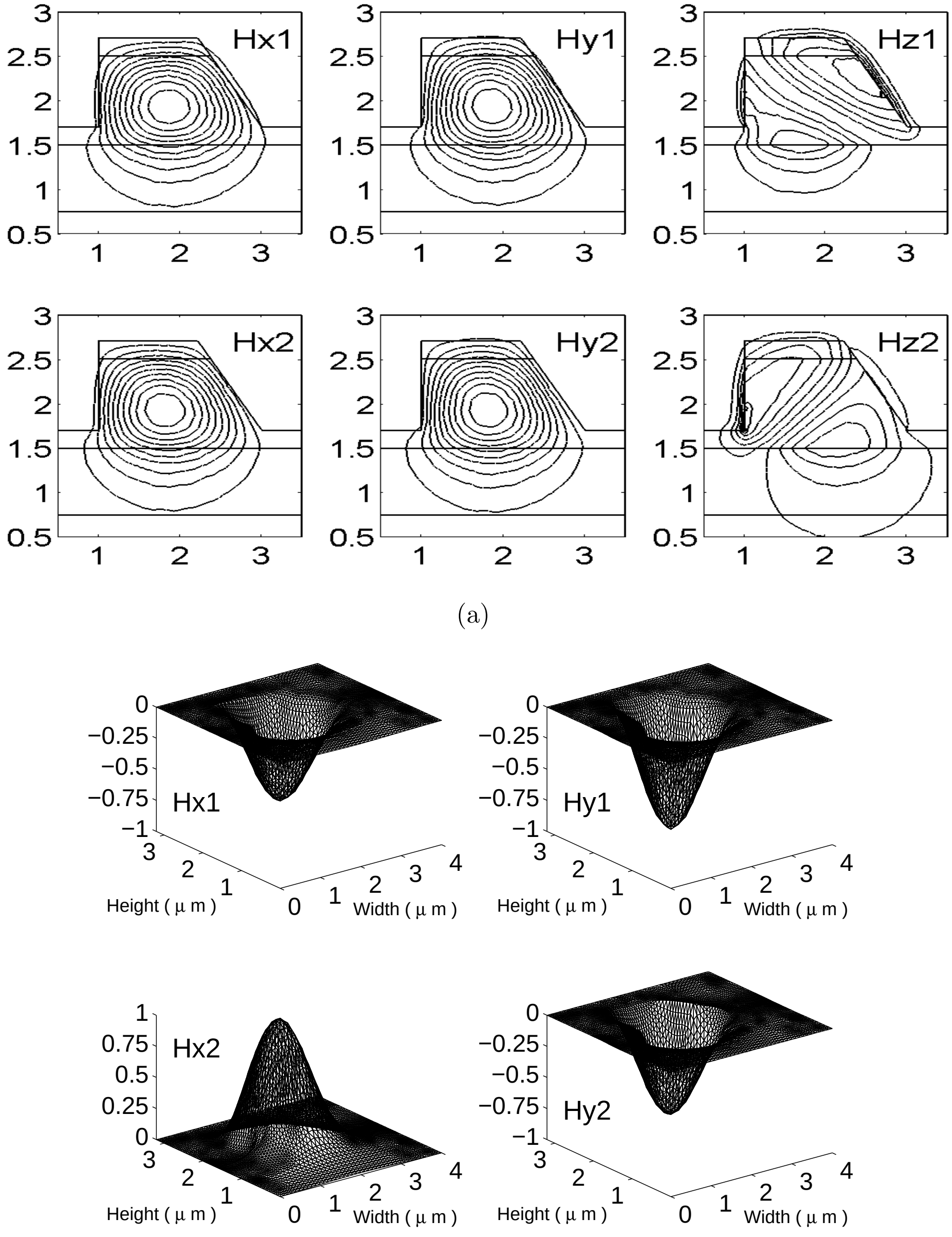

(a)

(b)

Figure 3.7: Field distribution of fundamental modes of the InP/InGaAsP polarization converter in [40, 52] with geometry parameters $W = 2\mu$m, $H = 1\mu$m, $h = h_r = 0.2\mu$m, $d_p = 0.2\mu$m, $\theta = 45^\circ$, and refractive indices $n_1 = 3.4$ (InGaAsP) and $n_2 = 3.27$ (InP): (a) two dimensional contour graph; and (b) three dimensional surface graph.

Chapter 4

Design Rules for Slanted-Angle Polarization Rotators

Having developed a sophisticated and versatile full-vectorial Finite Element Method (FEM) program package, in this chapter we introduce a set of simple and general design rules for slanted-angle polarization-rotating waveguides. Following these general procedures, we construct a class of single-mode Silicon-on-Insulator (SOI) polarization rotators that offer significant advantages in conversion efficiency, optical loss, fabrication tolerance, spectral response and spatial dimensions relative to III-V (semiconductors such as AlGaAs/GaAs and InGaAsP/InP) components.

As reviewed in Chapter 2, passive polarization rotators are central to optical communication systems, and generally are composed of concatenated segments, each of which rotates the light polarization a small amount, or a single-segment slanted-angle waveguide. III-V longitudinally periodic [15–20] and bent structures [21–27] were the first structures realized, followed by single-section slanted-angle polarization rotators fabricated in both GaAs and InP [40–48]. Compared with III-V waveguides of equivalent dimensions, silicon-on-insulator (SOI) waveguides [57,60–62,64–67] provide stronger optical confinement. Further, single-mode yet large cross-section SOI waveguides (with e.g., silicon film thickness of $3 \sim 10\mu$m) can be fabricated at relatively low cost. As a result, both the coupling loss to single-mode fibers (SMF) and the fabrication tolerance are enhanced.

In this chapter, we accordingly consider the design of single-section SOI slanted-angle polarization rotators. We develop a systematic design procedure that can be applied to general waveguide profiles and material systems. We first graph the maximum polarization rotation, single mode condition and modal coupling lengths as a function of various waveguide parameters, and then derive a simple empirical formula that can be employed to design SOI polarization converters over a wide range of silicon film thicknesses and to predict fabrication tolerances. We compare the performances and characteristics of SOI and III-V converters. Studies related to the fabrication tolerance, bending behavior, loss and coupling issues are to be presented in subsequent chapters.

4.1 Waveguide Geometry

The general geometry of a passive slanted-angle polarization rotator is displayed in Fig. 4.1(a). Standard III-V devices are based on either the symmetric external layer structure of Fig. 4.1(b) [18, 19, 40, 41, 49–53] or that of Fig. 4.1(e) [43–48]. In this work we however focus on the novel asymmetric external layer structure of Fig. 4.1(c).

In Fig. 4.1, H denotes the total rib height, which in the case of SOI waveguides is identical to the thickness of the silicon guiding film, so that a 3μm SOI design in this work refers to $H = 3\mu$m. Further, W is the width at the base of the rib, θ is the angle formed by the slanted-angle facet that to simplify fabrication generally coincides with a crystal plane, e.g., $\theta = 54.736°$ for the $\langle 111 \rangle$ crystallographic plane in Si and $\theta \simeq 52°$ for InGaAsP. The symbols h, h_r, d_c, d_p, d_i, and d_s denote the thicknesses of the external layer adjacent to the vertical rib facet, the external layer adjacent to the slanted facet, the region between the top of the rib and the end of the computational window, the cap, the insulator, and the substrate layers, respectively. The horizontal computational window dimensions are controlled by X_{sl} and X_{sr}. We define the ratio of the slab thickness to rib height as $r = \frac{h}{H}$ and the ratio of the rib width to rib height $s = \frac{W}{H}$ while the optical-axis rotation angle φ is taken to be positive for a clockwise rotation. In a SOI waveguide the refractive indices of rib, substrate and insulator regions are $n_1 = n_3 = 3.48$ for silicon and $n_2 = 1.45$ for SiO_2. The wavelength $\lambda = 1.55\mu$m and insulator thickness $d_i = 1.1\mu$m [1, 6, 7] are fixed throughout this thesis.

In the asymmetric SOI design of Fig. 4.1(c), one of the waveguiding layers outside the

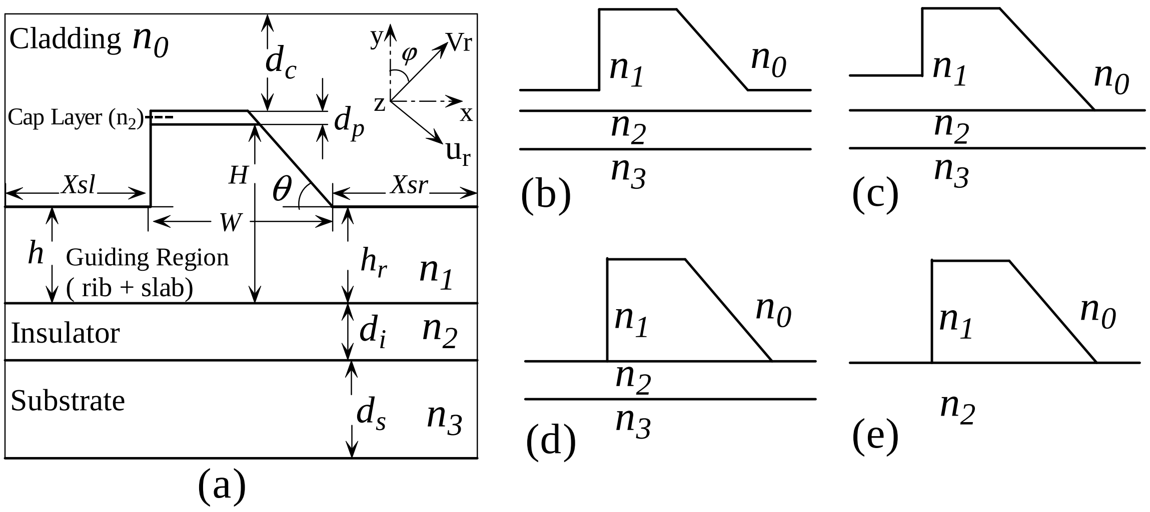

Figure 4.1: Slanted-angle polarization rotator: (a) general geometry; (b) conventional symmetric external waveguiding layer design ($h_r = h$); (c) asymmetric external layer design ($h_r = 0$); (d) design without external layers; and (e) single substrate waveguide without external layers.

rib region is etched completely to the SiO$_2$ layer unlike conventional slanted-angle polarization rotators [18,19,40,41,49–53] for which the external waveguiding layers are of the same height (although departures from symmetry caused by fabrication error occur, yielding undesired performance variations). Eliminating both external waveguiding layers [43–48] of course fully avoids such fabrication difficulties, but at the cost of a small device cross-section for single-mode operation since higher order modes then cannot radiate laterally. We will demonstrate in Section 4.3 that the single-mode region of slanted-facet waveguides, and especially waveguides with asymmetric external layers can encompass a larger region of waveguide parameters than conventional structures, increasing fabrication tolerance.

In slanted-angle waveguides, the modes are hybridized by the geometric asymmetry, becoming TE and TM with respect to the slanted facet rather than the substrate interface. In multiple section polarization rotators, the modes are typically weakly hybridized, while modes in single section devices are fully hybridized with nearly equal TE and TM components in each of the two orthogonal fundamental modes. In the latter case, the optical-axis is positioned at a 45° with respect to the lateral direction while the intensities of the two fundamental modes will be comparable. The polarization of an incoming TE or TM mode is therefore rotated by 90° after a half-beat length defined by Eq. (2.3).

As noted in Section 2.1.2 and 3.1, many simulation procedures have been applied to slanted-angle waveguides, however, certain difficulties have been noted. The finite-difference method (FDM) for example can give rise to spurious modes [152,153] and numerical instabilities [41]. Further, it is relatively computationally inefficient for slanted-angle waveguides [46, 47] and possesses large errors at high-contrast waveguide corners such as those present in Fig. 1 of [43]. In contrast, the finite-element-method (FEM), enhanced through an unstructured mesh with adaptive refinement, can be easily applied to waveguide corners and slanted facets without an appreciable increase in either memory usage or CPU time. Having developed an accurate and efficient full-vectorial FEM eigenmode solver with mixed triangular elements in Chapter 3, we here employ the $\boldsymbol{H}$-formulation since the magnetic field components are naturally continuous across dielectric interfaces [167, 188].

4.2 Design Procedure

In this and the following sections, we examine the dependence of both the conversion efficiency between the incoming TE and TM modes and the parameter limits for single mode operation on the details of the device geometry for slanted-angle polarization converters. We present both descriptive two-dimensional contour plots and simple empirical formulas from which the optimal waveguide parameters can be immediately obtained.

4.2.1 Optical-axis Rotation Contours

In our first set of simulations, we examine the rotation of the optical-axes as a function of the height and width of the slanted-angle rib waveguide as well as the thicknesses of the slab layers on both sides of the rib. The direction of the slanted waveguide facet naturally follows the $\langle 111 \rangle$ crystallographic plane. Subsequently in our magnetic field formulation the rotation of the optical-axis is identified with a suitable ratio of the TE and TM components of the lowest-order waveguide eigenmode. In the magnetic case, three possible criteria are the vectorial ratio of the x and y field components $[H_x]/[H_y]$ [49–51], the ratio of the maximum values of the x and y magnetic field components $\max(H_x)/\max(H_y)$ [49], or the rotation parameter R [40]:

$$R = \frac{\iint\limits_{\Omega} n^2(x,y) \cdot H_x^2(x,y)\, \mathrm{d}x\, \mathrm{d}y}{\iint\limits_{\Omega} n^2(x,y) \cdot H_y^2(x,y)\, \mathrm{d}x\, \mathrm{d}y} \tag{4.1}$$

where $n(x,y)$ is the refractive index distribution, and the magnetic field components $H_x(x,y)$ and $H_y(x,y)$ are the components of the specified eigenmode in the lateral and transverse directions, respectively. For a 45° optical-axis rotation, these components are almost identical so that $R = 1$.

We employ the rotation parameter to characterize the optical-axes rotation as Eq. (4.1) contains contributions from the entire field region. The rotation parameters for the two lowest-order eigenmodes are denoted as R_1 and R_2, respectively; while R without a subscript in default indicates R_1. Moreover, $R \gg 1$ designates an x-polarized lowest-order mode, while $R \ll 1$ corresponds to a y-polarized mode. Since the modes are orthogonal the optical-axis rotation angle is:

$$\varphi = tan^{-1}(R) = tan^{-1}(R_1) = cot^{-1}(R_2) \tag{4.2}$$

In Figs. 4.2 and 4.3, we present normalized contours for the optical-axis rotation-angle as a joint function of both the normalized rib height and external waveguiding layer thickness. The different cases in the figures are as follows: Fig. 4.2(a) corresponds to a conventional symmetric external waveguiding layer SOI polarization rotator, Fig. 4.2(b) to our proposed slanted-angle asymmetric external waveguiding layer SOI design, Fig. 4.3(a) to a conventional 1.3μm weakly-guided InGaAsP polarization converter [41, 49] and Fig. 4.3(b) to an InGaAsP polarization rotator with an asymmetric waveguiding layer geometry where $n_1 = 3.370$ in the rib, $n_2 = n_3 = 3.324$ in the substrate and the facet angle is $\theta = 52°$.

The optical-axes contours for SOI waveguides show very low sensitivity to the silicon film thickness, H, for $1\mu\text{m} < H < 30\mu\text{m}$. As an illustration, we show in Fig. 4.4 the contour charts for asymmetric waveguiding layer geometry with various silicon guiding film thickness of 1.3μm, 2μm, 3μm, and 5μm, respectively. These graphs display exactly the same pattern, and have negligible difference if normalized by the silicon film thickness. Same situation is with the symmetric waveguiding layer slanted-angle SOI waveguides, as is evident from Fig. 4.5 where silicon film thickness of 2μm, 3μm, and 5μm are considered.

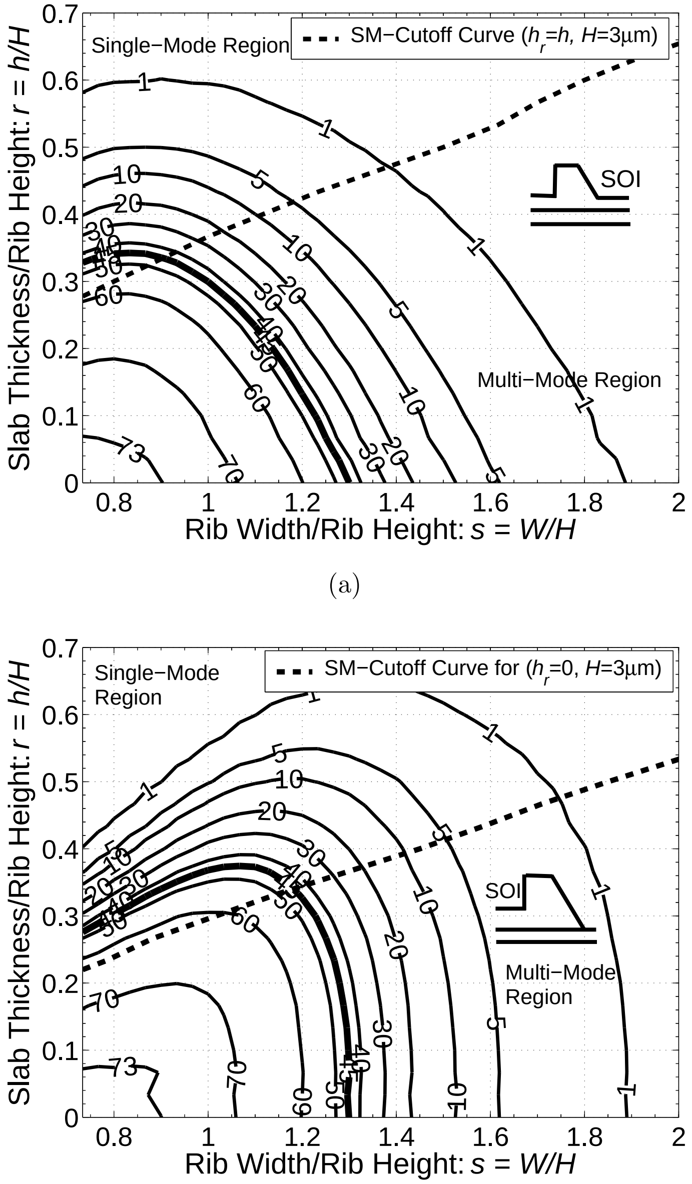

Figure 4.2: Optical-axis rotation angle (φ) contours for slanted-angle SOI waveguides: (a) symmetric external waveguiding layer SOI waveguide; and (b) asymmetric external waveguiding layer SOI waveguide.

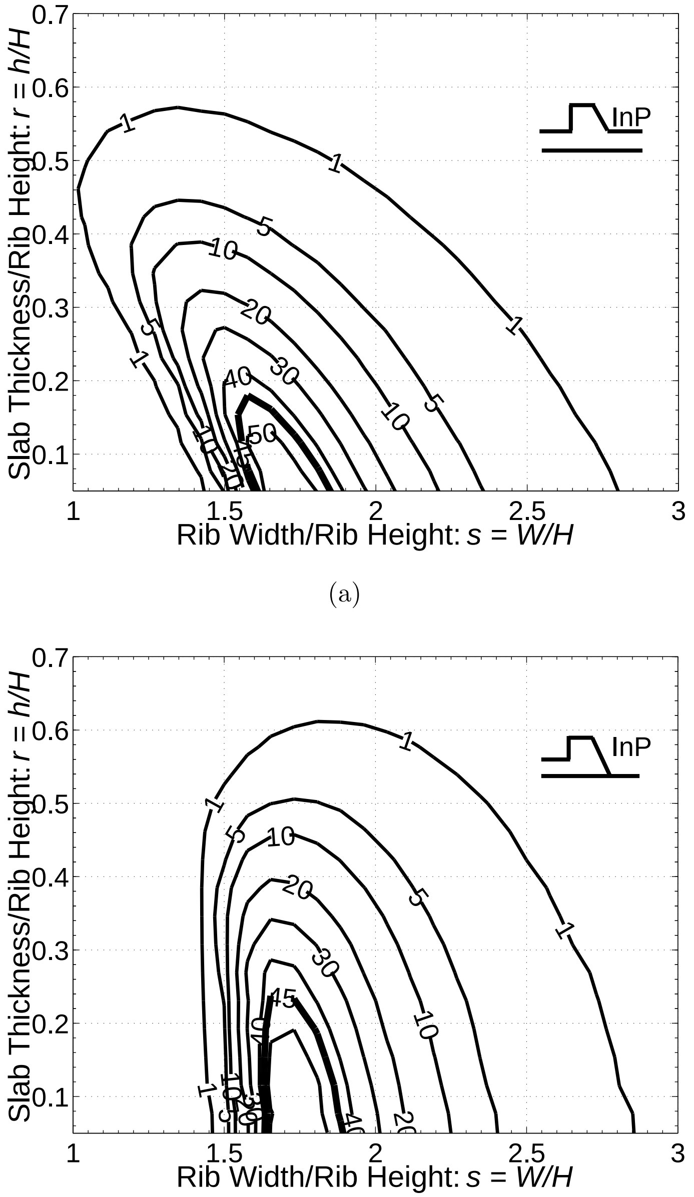

(a)

(b)

Figure 4.3: Optical-axis rotation angle (φ) contours for slanted-angle III-V waveguides: (a) symmetric external waveguiding layer III-V waveguide ($H = 1.3\mu\text{m}$, $n_1 = 3.370$, $n_2 = n_3 = 3.324$, $\theta = 52°$); and (b) asymmetric external waveguiding layer III-V waveguide ($H = 1.3\mu\text{m}$, $n_1 = 3.370$, $n_2 = n_3 = 3.324$, $\theta = 52°$). These III-V waveguides are single-mode for $\varphi = 45°$.

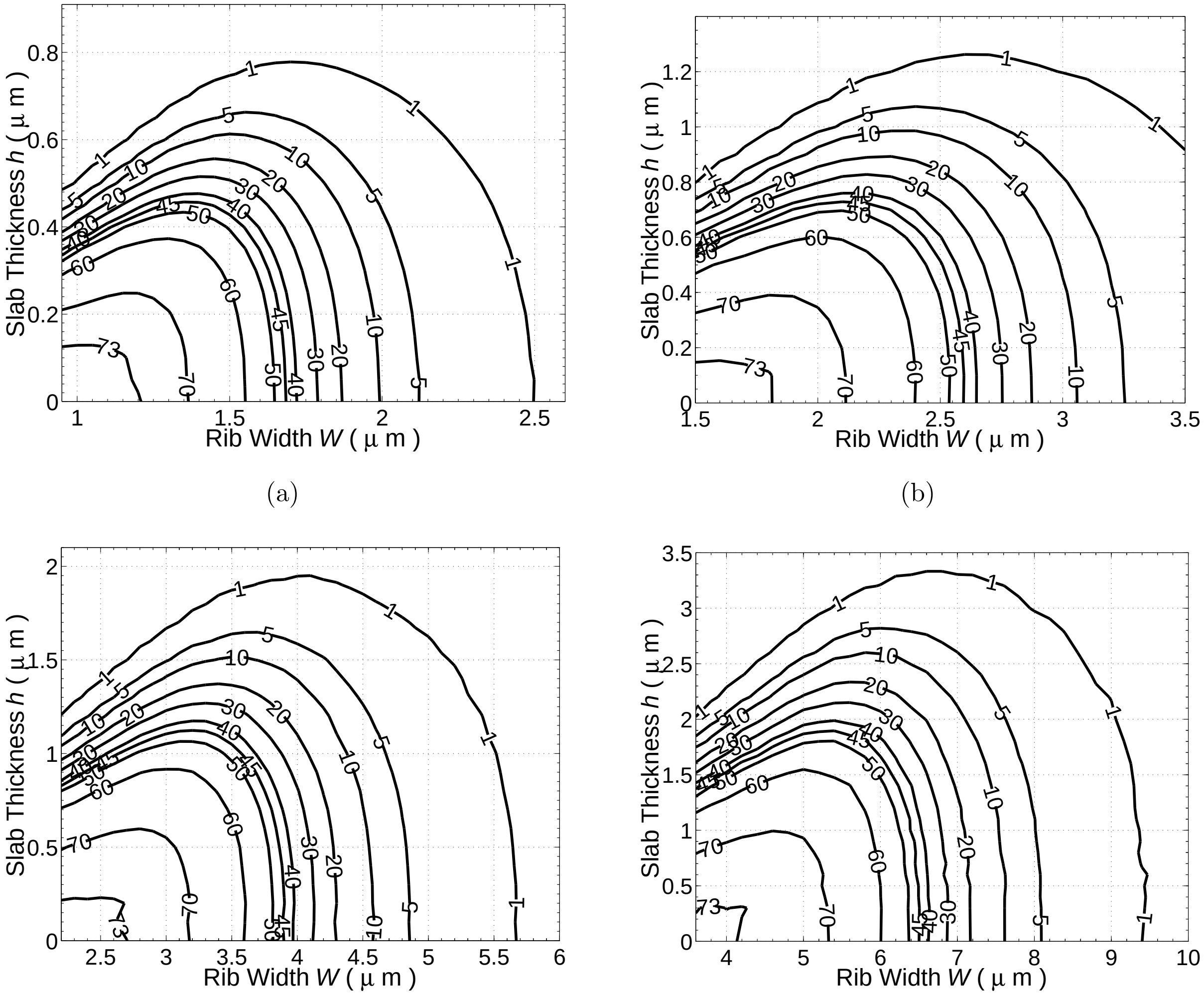

(a)

(b)

(c)

(d)

Figure 4.4: Optical-axis rotation angle (φ) contours for asymmetric external waveguiding layer slanted-angle SOI waveguides as in Fig. 4.1(c) with various silicon guiding film thickness: (a) $H = 1.3\mu$m; (b) $H = 2\mu$m; (c) $H = 3\mu$m; and (d) $H = 5\mu$m.

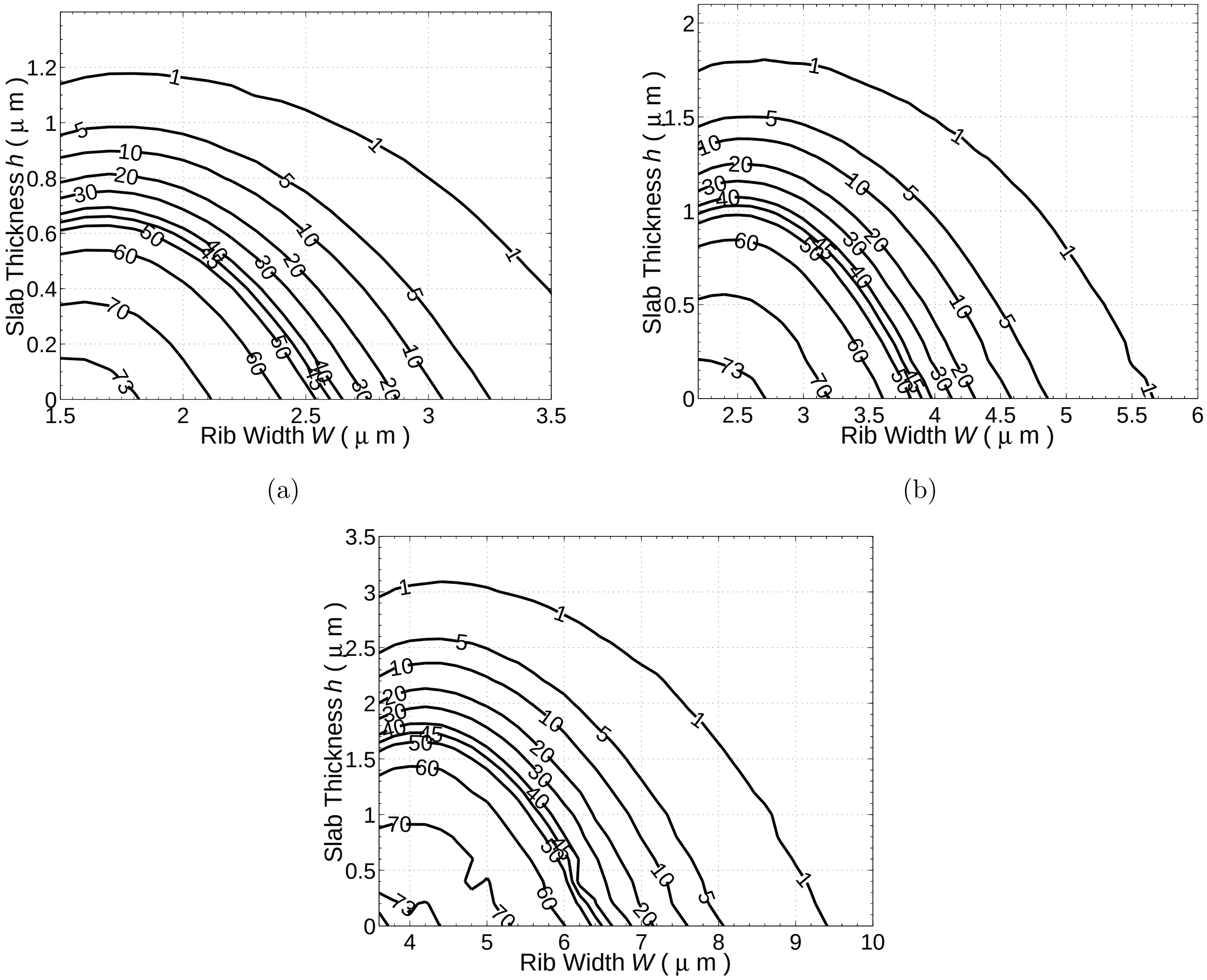

(a)

(b)

(c)

Figure 4.5: Optical-axis rotation angle (φ) contours for symmetric external waveguiding layer slanted-angle SOI waveguides as in Fig. 4.1(b) with various silicon guiding film thickness: (a) $H = 2\mu$m; (b) $H = 3\mu$m; and (c) $H = 5\mu$m.

Besides being nearly independent of the silicon layer thickness, the information in the optical-axis rotation-angle contours can be utilized for both single and multiple section rotators. That is, any waveguide exhibiting 45° optical-axis rotation can be employed as a single section polarization rotator; while e.g., a 22.5° optical-axis-rotating waveguide is suitable for a two-section rotator (c.f. Section 2.1.3 and Eq.(2) of [40]). Since in this thesis we focus on single-section components for reasons of size, loss and fabrication simplicity, the 45° contour is distinguished in the graphs by its thickness. The two dashed lines in Figs. 4.2(a) and 4.2(b) indicate the waveguide parameters corresponding to the single mode cutoff condition and will be discussed in detail in Section 4.3.

To establish the accuracy of our results, we observe from Fig. 4.3(a) that a $H = 1.3\mu$m single section III-V rotator rib width requires a waveguide width $W = 2.4\mu$m for a outer-slab height of $h = 0.1\mu$m. This result agrees well with the published value of $\sim 2.5\mu$m (Case I of Table I in [41], Fig. 4 of [49], Fig. 7 of [54]), however, Fig. 5 of [49] indicates that the maximum field ratio (H_x/H_y or H_y/H_x) occurs at $W = 2.4\mu$m. Our graph additionally yields a continuum of design parameters and explains previous observations such as the increase and the subsequent decrease of hybridization with increasing rib width (Fig. 2 of [50]) as verified from the rotation angles along lines of constant h in Fig. 4.3(a).

4.2.2 Merits of SOI Polarization Rotator

To illustrate our design procedure through a practical example, we consider the single-section SOI polarization rotating waveguide given by $h = 1.1\mu$m, $W = 3.3\mu$m, $h_r = 0$ and $H = 3\mu$m that is located on the 45° contour line and in the single-mode region of Fig. 4.2(b). The two lowest-order eigenmodes of this waveguide are shown in Fig. 4.6. Observe that the two eigenmodes are almost identical as required for a 45° optical axis rotation. The length of the corresponding polarization rotator is $L_\pi = 850\mu$m.

The additional range of parameter choices provided by SOI waveguides compared to low index-contrast III-V waveguides is evident from the lengths of the 45° contours in Figs. 4.2 and 4.3. Thus, while the 3μm SOI rotator mentioned in the previous paragraph has a length of 850μm (which is close to the reported value of $\sim 700\mu$m for equivalent 1.3μm III-V rotators [41,49]), we have found that single-mode 1.3μm SOI structures can be designed with L_π between 35 and 100μm yielding much shorter device lengths. To illustrate, a single-

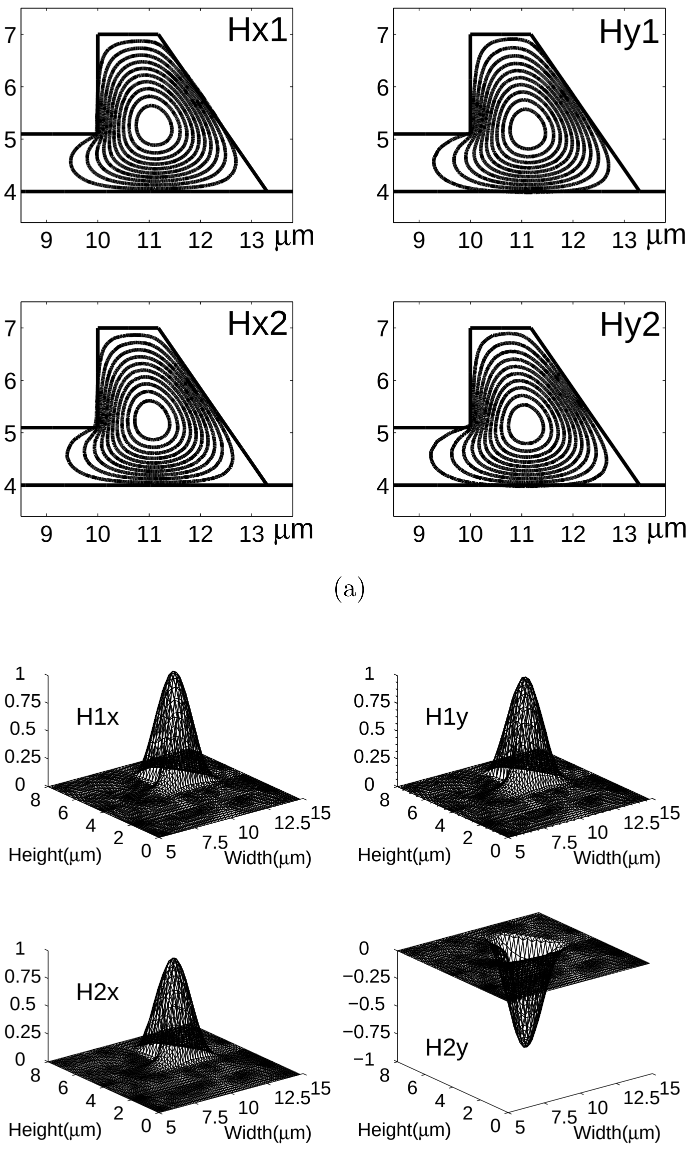

(a)

(b)

Figure 4.6: Orthogonally polarized two lowest-order modes of a $\varphi = 45°$ SOI waveguide with $H = 3\mu\text{m}$, $W = 3.3\mu\text{m}$, $h = 1.1\mu\text{m}$, $h_r = 0$, $L_\pi = 850\mu\text{m}$ and $R = 1.07$: (a) two-dimensional (2D) contour graph; and (b) three-dimensional (3D) surface plot.

mode waveguide with $H = 1.3\mu$m, $W = 1.55\mu$m, $h = 0.4\mu$m and $h_r = 0$, yields $R = 1.02$ and a half-beat length $L_\pi = 98\mu$m; while a waveguide with $H = 1.3\mu$m, $W = 0.95\mu$m, $h = 0.35\mu$m and $h_r = 0$, has $R = 0.98$ and $L_\pi = 34\mu$m.

Another feature of our SOI waveguide design is the flexible cross-section which can be easily made comparable to that of either laser diodes or single-mode fibers (SMF), reducing coupling-loss. Further, the field is effectively confined to the rib region unlike III-V waveguides, which generally require a thick ($> 5\mu$m) substrate [66]. For larger waveguides, fabrication tolerance is enhanced, while the strong optical confinement decreases the optical loss, minimum bending radius and device spacing. Together with the decreased substrate thickness, these SOI designs indicate that compact and low-price products can be fabricated that are fully compatible with CMOS integrated circuit (IC) technology.

4.2.3 Range of Validity

While the contour charts of Fig. 4.2 were calculated for a $H = 3\mu$m silicon guiding layer thickness, almost identical results are obtained for a wide range of Si thicknesses, as have been clearly illustrated in Figs. 4.4 and 4.5 for $H = 1.3$ to 5μm. Therefore, in Figs. 4.2(a) and 4.2(b), the geometric parameters W and h are normalized with respect to the silicon film thickness H, and these normalized charts (with normalized outer-slab thickness $r = h/H$ and normalized rib width $s = W/H$) can therefore be employed for general design purpose. In this section, we subsequently study the range of H values for which such a normalization yields nearly equivalent curves.

We first select a $\varphi = 45°$ asymmetric waveguiding layer structure of Fig.4.1(c) with $H = 3\mu$m, $W = 3.2\mu$m, $h = 1.1\mu$m, and $h_r = 0$ as a reference waveguide and display in Figs. 4.7(a) and 4.7(b) our FEM results for the optical-axis rotation and the half-beat length as H is varied from 1 to 30μm while $r = h/H$, $s = W/H$, and h_r/H are kept invariant. Note that the optical-axis rotation is nearly independent of the silicon layer thickness, H, in this region and in fact for $2\mu\text{m} < H < 10\mu$m the rotation angle φ varies by only $1°$. The $8°$ decrease in rotation angle at $H = 30\mu$m can be compensated by reducing W by $< 10\%$ of H, as is evident from Fig. 4.2(b). To obtain approximate parameters for a 45° optical axis rotating waveguide, our normalized charts can accordingly be applied to any commercially available wafer with $1\mu\text{m} < H < 30\mu$m. However, since the half-

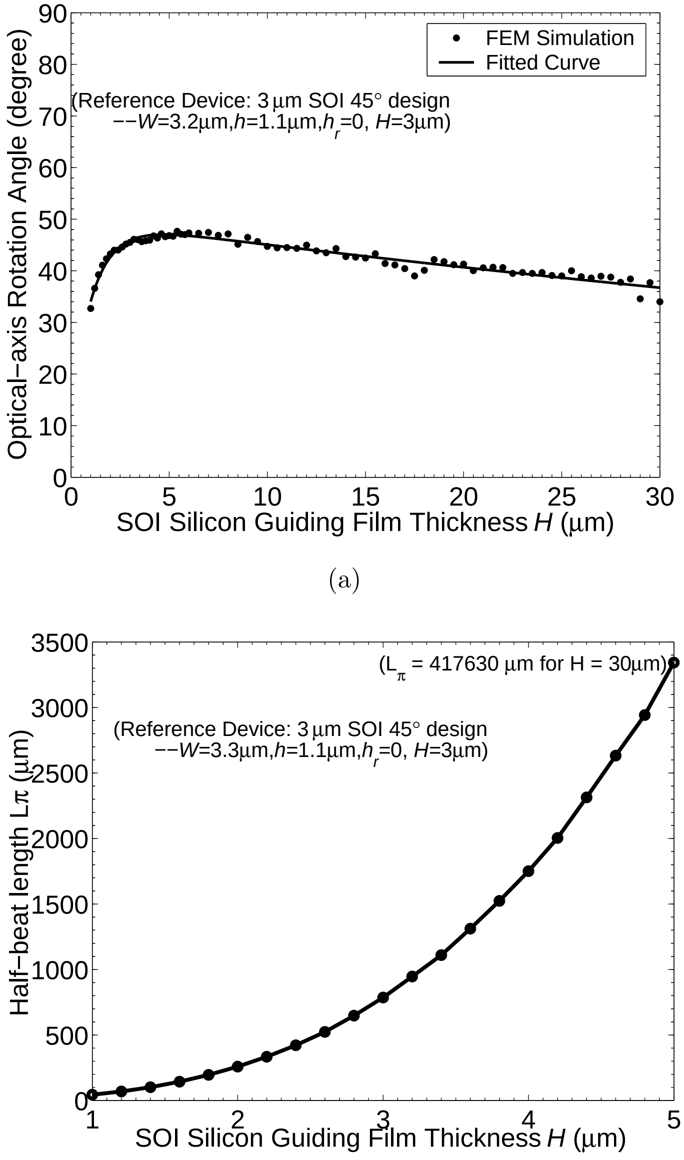

(a)

(b)

Figure 4.7: (a) The optical-axis rotation angle φ and (b) the half-beat length L_π for similar asymmetric waveguiding layer waveguides as a function of SOI silicon layer thickness H where $r = h/H$, $s = W/H$ and h_r/H are kept invariant.

beat length, illustrated in Fig. 4.7(b), increases exponentially with the silicon guiding film thickness, for short devices H should be minimized.

That the optical-axis rotation remains nearly constant as the SOI waveguide dimensions are varied can be understood from the field distributions of Fig. 4.6. Since these are almost fully contained in the rib waveguide they are influenced to almost the same degree by the SOI waveguide geometry. Hence, the modes are equally TE or TM with respect to the slanted waveguide facet. In contrast, in a standard III-V semiconductor waveguide, the depth of penetration of the modal field into the substrate region varies rapidly with changes in the waveguide dimension (as evident from Figs. 3.6 and 3.7, or Fig.6 of [40], Fig.4 of [49], and Fig.9 of [54]), so that the overall shape of the field and hence the hybridization induced by the slanted facet changes rapidly with guiding layer thickness in III-V devices.

4.2.4 Empirical Design Formula

While Fig. 4.2 can be employed to design arbitrary single or multiple section polarization rotators, for a single-section device only the 45° contour is of practical interest. As demonstrated in Figs. 4.8(a) and 4.8(b), the 45° contour line can be approximated by a simple rational polynomial:

$$r = \frac{p_1 \cdot s^2 + p_2 \cdot s + p_3}{s^3 + q_1 \cdot s^2 + q_2 \cdot s + q_3} \tag{4.3}$$

with $r = h/H$ and $s = W/H$. Equation (4.3) fits other rotation-angle contours as well. For single-section rotators, the coefficients appearing in (4.3) are $p_1 = -495.7$, $p_2 = 922.3$, $p_3 = -359.5$, $q_1 = -841.7$, $q_2 = 1431$, $q_3 = -406.7$ for the asymmetric external waveguiding layer SOI structure of Fig. 4.1(c), and $p_1 = -0.8966$, $p_2 = 1.638$, $p_3 = -0.6138$, $q_1 = -3.449$, $q_2 = 4.096$ and $q_3 = -1.223$ for the conventional symmetric external waveguiding layer SOI structure of Fig. 4.1(b). Following the considerations of the previous section, these parameters were determined for a 3μm SOI silicon film thickness but can to a good approximation be applied within the range $1\mu\text{m} < H < 30\mu\text{m}$.

4.2.5 Half-Beat Length Variation

Finally we determine the device length as a function of the rib waveguide dimension for a single-section polarization rotator. We display in Figs. 4.9(a) and 4.9(b) the variation of the

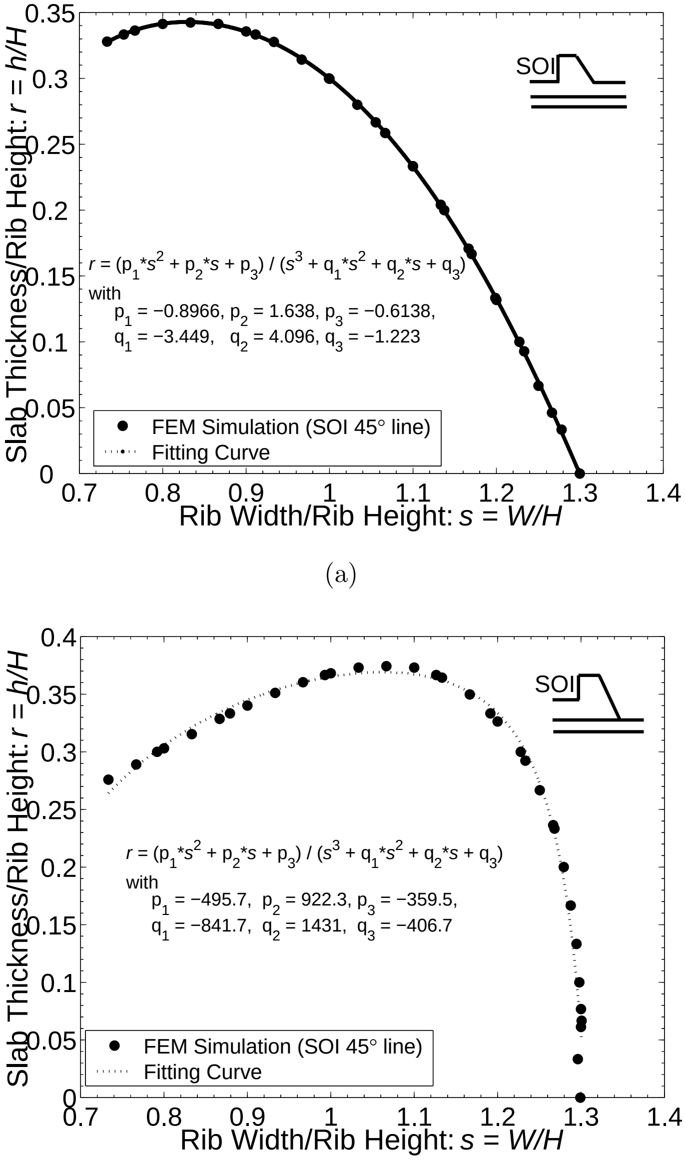

(a)

(b)

Figure 4.8: The 45° optical-axis rotation contours of Figs. 4.2(a) and 4.2(b) together with a rational polynomial approximation for: (a) a SOI polarization converter with conventional symmetric external waveguiding layer; and (b) novel asymmetric outer-slab layer SOI structure.

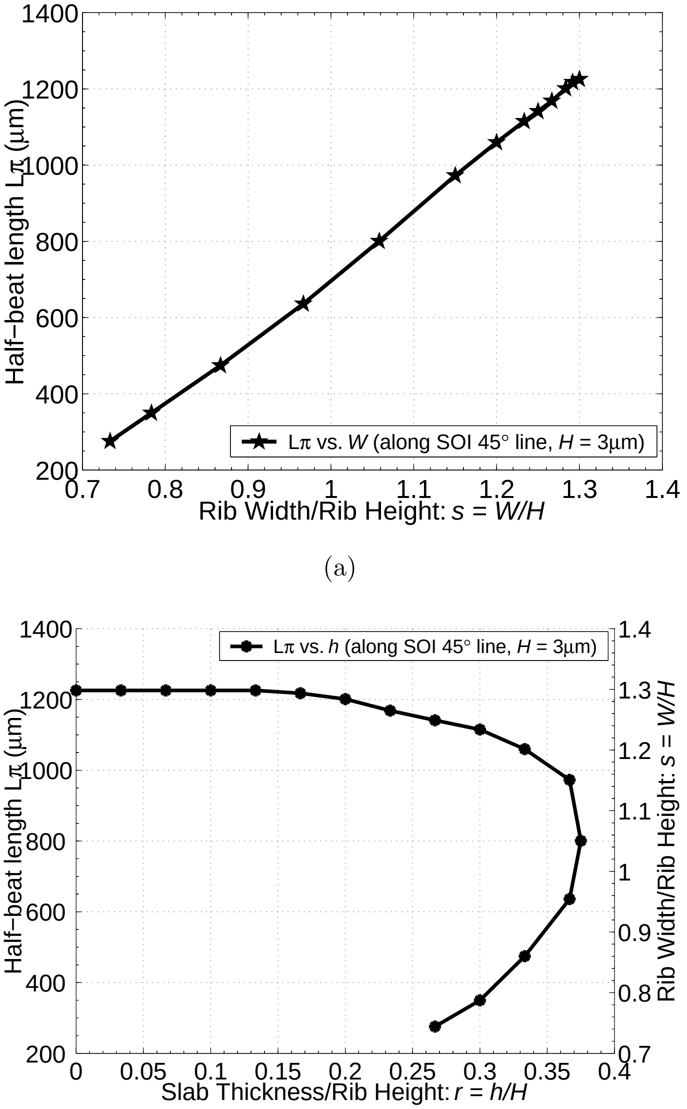

(a)

(b)

Figure 4.9: The dependence of the half-beat length L_π for asymmetric external waveguiding layer waveguides that rotate the optical-axis by 45° with: (a) rib width W; and (b) external waveguiding layer height h.

half-beat length L_π with the rib base width W and the external waveguiding layer thickness h, respectively, for asymmetric external waveguiding layer SOI waveguides on a 3μm silicon guiding layer that exhibit a 45° optical-axis rotation. Clearly the half-beat length L_π varies linearly with rib width W but reflects the path of the 45° contour in Fig. 4.8(b) with the slab thickness h. From this behavior together with the exponential relationship in Fig. 4.7(b) the device length can be estimated for any waveguide. In particular, for Si film thicknesses of 1.3μm, 2μm, 3μm and 5μm, we found that, respectively, $35\mu\text{m} \leq L_\pi \leq 100\mu\text{m}$, $125\mu\text{m} \leq L_\pi \leq 375\mu\text{m}$, $250\mu\text{m} \leq L_\pi \leq 1225\mu\text{m}$ and $1150\mu\text{m} \leq L_\pi \leq 5125\mu\text{m}$. In each of these cases, the half-beat length varies linearly with the base rib width as in Fig. 4.9(a), and with the outer-slab thickness in the same manner as in Fig. 4.9(b). Evidently a 3μm Si guiding layer encompasses L_π values that are relevant to most practical applications, while extremely short ($35\sim100\mu$m) SOI polarization rotators can in principle be designed (c.f. Section 4.2.2) with the same 1.3μm cross-section as many current III-V rotators, which typically are several hundred microns in length.

4.3 Single-Mode Condition

Low-loss, high conversion efficiency polarization rotators must support a single guided mode for each polarization in order to insure that no power is coupled into higher-order modes during propagation. The condition for single mode operation in SOI rib waveguides can be simply approximated by Soref's formulas [90,98,99], which in the case of trapezoidal cross-sections are modified in [99, 101]. However, these expressions are invalid for slanted-angle waveguides where the guided modes become strongly hybridized. Additionally, previous studies were limited to slightly-etched SOI rib waveguides with $0.5 < r = h/H < 1$, although strong polarization conversion instead requires deeply-etched waveguides with $0 < r < 0.5$, as evident from Fig. 4.2. While Pogossian [98] modified Soref's formula to improve its relevance to waveguide design, his expression is based on *predicted* (rather than *experimental*) data [95] generated from Soref's original formulae [90]. Similarly, [99] employ numerical procedures for weakly guiding structures, while [94] mistakes the deep-etching ($r \leq 0.5$) for Soref's shallow-etching ($r \geq 0.5$) condition.

Here we determine the single mode cutoff condition through a FEM mode solver by

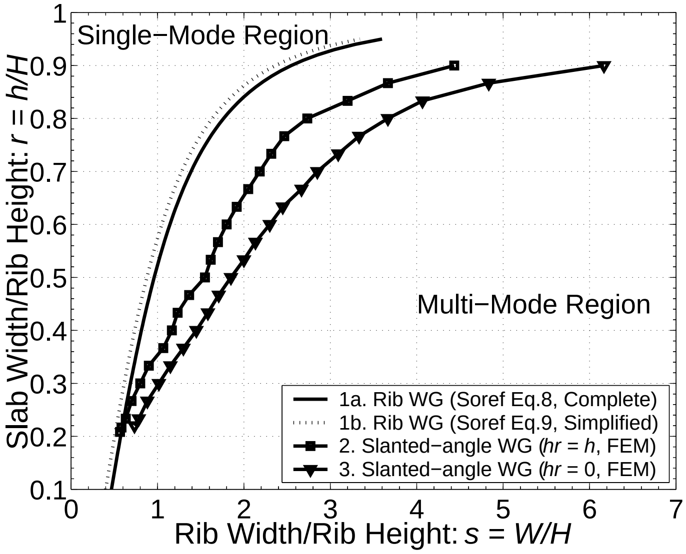

(a)

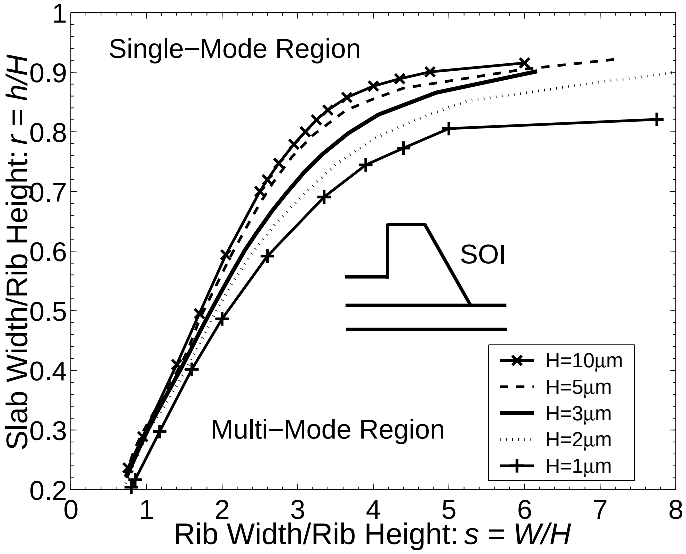

(b)

Figure 4.10: The single mode region boundary for: (a) the SOI rib waveguide and slanted-angle polarization rotators with same silicon film thickness $H = 3\mu$m; and (b) the asymmetrical external waveguiding layer waveguides with different silicon guiding film thicknesses.

increasing the rib width for a fixed slab thickness until a third mode appears. First we contrast in Fig. 4.10(a) the single-mode cut-off boundary of different waveguides with the same silicon film thickness $H = 3\mu$m. The curves marked 1 to 3 correspond to standard rib waveguides, symmetric external waveguiding layer and asymmetric external layer slanted-angle waveguides, respectively. The FEM simulation clearly verifies that Soref's equation (Eqs.(8) and (9) of [90]) is the most accurate formulation for SOI rib waveguides. From Fig. 4.10(a), we conclude that for a fixed silicon film thickness H, our asymmetric external layer design displays the greatest region of normalized waveguide parameter space, (r, s), for single-mode operation. At a fixed value of $r = h/H$ the asymmetric waveguiding layer slanted-angle structure of Fig. 4.1(c) provides the largest range of normalized widths, $s = W/H$, that yield a single-mode waveguide with a 45° optical-axis rotation.

Next, we examine in Fig. 4.10(b) the single-mode behavior of our asymmetric waveguiding layer structure as the silicon layer thickness H is varied. As expected, as the thickness is decreased, a larger region of parameter space is associated with single-mode behavior. On the other hand, to achieve a large optical-axis rotation, the waveguide must be deeply etched as evident from Fig. 4.2. The single-mode boundary curve is then nearly invariant even with respect to changes in the silicon layer thickness H.

Consequently, although the single-mode boundary curves in Figs. 4.2(a) and 4.2(b) are computed with $H = 3\mu$m, these curves are nearly unchanged for $1\mu\text{m} < H < 30\mu\text{m}$, varying by less than 1% for $r < 0.5$. In contrast, for the $H = 1.3\mu$m III-V devices discussed in Figs. 4.3(a) and 4.3(b) all waveguides that rotate the optical-axis by 45° are single-mode, however, the single-mode behavior of III-V waveguides is dependent on H as discussed in Section 4.2.3. Referring to Figs. 4.2(a) and 4.2(b), a 45° optical-axis rotating single-mode SOI waveguide requires $0.2 < r < 0.4$. Any point on the 45° optical-axis rotation contour therefore yields a realizable single-section polarization rotator as typified by Fig. 4.6.

As well, Figs. 4.2(a) and 4.2(b) indicate that the asymmetric waveguiding layer structure has an enhanced region of single-mode operation given by $1.2 > s = W/H > 0.71$ while the corresponding interval for the symmetric external layer structure is $0.9 > s > 0.71$. Coupled with the ease of fabrication of structures for which a silicon oxide insulator layer prevents further etching of the slanted facet, our results clearly indicate the potential advantages of the asymmetric structure.

4.4 Summary

In this chapter, we have mapped the optical-axis rotation and single-mode cutoff condition of slanted-angle polarization rotators onto a contour map in normalized variables. For the subset of SOI slanted-angle waveguides that rotate the optical-axis by 45° the information in the two-dimensional diagram can be summarized by a one-dimensional empirical formula for the waveguide parameters. This procedure enables the rapid design of periodic and single-section slanted-angle polarization converters with either symmetric or asymmetric external waveguiding layers for rib heights from 1 to 30μm.

We also examined the single-mode cutoff condition of SOI structures with different silicon guiding layer thicknesses and demonstrated that the asymmetric-slab structure has a considerably larger region of single mode behavior and therefore fabrication tolerance than other waveguide designs. For the same guiding layer thickness, SOI polarization rotators exhibit enhanced optical confinement and are therefore more compact than III-V components.

Chapter 5

Fabrication Tolerance of SOI Polarization Rotators

We have theoretically predicted the feasibility and advantages of employing silicon-on-insulator (SOI) material for passive polarization rotators (PR), and have also found improved performance of the asymmetric external waveguiding layer design as compared with other structures in Fig. 4.1. Such asymmetric SOI polarization rotators therefore have great potential in future optical communication systems due to the superior performance and simple geometry. However, the performance of practical devices will inevitably be affected by factors such as fabrication error and wavelength fluctuation. In low cost silicon photonics processing, there is typically 0.1μm fluctuations in geometric parameters [1,6,7]. Obviously, a thick silicon layer (e.g., $H = 10\mu$m) has a greater tolerance than a thin layer (e.g., $H = 3\mu$m) to a 0.1μm parameter change. However, even for the same silicon film thickness, the fabrication tolerance of the waveguide design varies moderately with the location on the 45° line of our optical-axis contour plots.

In this chapter, we only analyze the fabrication tolerance of several novel asymmetric external waveguiding layer SOI polarization rotators as illustrated in Fig. 4.1(c) that are of practical importance. Section 5.1 presents an analytical formula for polarization conversion efficiency. The fabrication tolerances of polarization converters made of SOI and III-V materials are compared in Section 5.2. Two typical SOI PRs of practical significance are analyzed in detail in Section 5.3. Following this, Section 5.4 studies the wavelength stability of SOI polarization converters. Finally, Scanning Electron Microscope (SEM) images of some fabricated device samples and experimental results are presented in Section 5.5.

5.1 Polarization Conversion Efficiency Formula

Some former fabrication studies on III-V slanted-angle polarization rotators [49–51] simply observe the variation of a single quantity such as the half-beat length or the polarization direction with respect to the waveguide geometric parameters. However, more closely related to the performance of polarization rotators are the polarization conversion (PC) efficiency and the polarization extinction ratio (ER), which are related to a combination of device quantities. The polarization conversion (PC) efficiency measures the percentage of power, P, transferred between the orthogonal polarization components for a given input polarization state and is therefore

$$PC_{\mathrm{TE}\to\mathrm{TM}} = P_{\mathrm{TM}}/(P_{\mathrm{TE}} + P_{\mathrm{TM}}) \times 100\% \tag{5.1}$$

for an incoming TE mode. After some algebraic manipulations (details in Appendix A and [8]), the PC is found to be in terms of the device length L, half-beat length L_π and optical-axis rotation angle φ (or rotation parameter R):

$$PC = 4\,\sin^2\varphi\,\cos^2\varphi\,\sin^2(\frac{\pi L}{2L_\pi}) \times 100\% \tag{5.2}$$

while the polarization extinction ratio ER, which is related in the absence of loss to the polarization conversion efficiency by $ER = 10\,\log[(1-PC)/PC]$, is defined as [47]:

$$ER = 10\,\log\left(\frac{P^{\mathrm{out}}_{\mathrm{TE}}}{P^{\mathrm{out}}_{\mathrm{TM}}}\right)\Bigg|_{\text{TE polarized input}} \tag{5.3}$$

The polarization conversion efficiency (PC) formula Eq. (5.2) is readily verified from the BPM data for InGaAsP devices in Figs. 12 and 13 (at $\lambda = 1.61\mu$m) of [50], Fig. 3 of [43], and Fig. 6 in [38], and is to be further verified in Section 6.4.3 with full-vectorial FE-BPM simulation results for asymmetric SOI polarization converters.

5.2 Tolerance Comparison of SOI and III-V PRs

To illustrate the magnitude of fabrication tolerances, we first consider a waveguide with $H = 3\mu$m, $h_r = 0$, $h = 1\mu$m, and $W = 3.6\mu$m, which yields a half-beat length $L_\pi = 1053.5\mu$m for a 45° optical-axis rotation according to Fig. 4.3(a), and describe the variation of the optical-axis rotation parameter R and half-beat length L_π with rib width W and external waveguiding layer thickness h. Varying W from 2.2 to 5.2μm, yields Fig. 5.1(a) and Fig. 5.2(a) for L_π and R. The dependence of these quantities on h for $0.4 < h < 1.4\mu$m is instead displayed in Fig. 5.1(b) and Fig. 5.2(b). From Figs. 5.1(a) and 5.1(b), we find that a 0.1μm fabrication error in W or h changes L_π by 80μm and 40μm, respectively. These values compare with 50μm and 20μm for the corresponding III-V waveguide with $L_\pi = 403\mu$m given by Figs. 2 and 10 of [50]. However, the relative deviation in the SOI case is 7.6% and 3.8%, which is markedly smaller than 12.4% and 5% for the III-V waveguide in [50].

From Figs. 5.2(a) and 5.2(b), we observe additionally that the rotation parameters R_1 and R_2 are inversely proportional to each other. The reciprocal relationship is a direct consequence of the orthogonality of the two lowest-order modes. From Eq. (4.2) and Fig. 5.2, the maximum variation of the optical-axis rotation angle φ is bounded by $+4°$ when either the rib width or the rib height is reduced by 0.1μm, and by $-7°$ when W or h is increased by 0.1μm.

For the above $H = 3\mu$m SOI polarization rotator, the polarization conversion efficiency and extinction ratio are $PC = 99.98\%$ and $ER = -38$dB, respectively. Even for a variation of W of 0.1μm, which yields the maximum $-7°$ rotation angle variation, we calculate $\Delta L_\pi = 7.6\%$ and $PC = 92.81\%$ corresponding to $ER = -11$dB, while a 0.1μm h variation yields $\Delta L_\pi = 3.8\%$, $PC = 97.71\%$ and $ER = -16$dB. In both of these worst cases, the performance is acceptable for many applications (c.f. Fig. 5 of [47], and $PC = 92 \sim 93\%$ after $\pm 0.1\mu$m rib width variation in [40]).

Repeating the above analysis for a 1.3μm SOI rotator with $h_r = 0$, $h = 0.4\mu$m, $W = 1.55\mu$m and $L_\pi = 98\mu$m, we find that the dependence of L_π and R on W and h is largely identical to Figs. 5.1 and 5.2. While the fabrication tolerances are decreased relative to the 3μm rotator since $PC = 87.59\%$ and $ER = -8.5$dB for $\Delta W = 0.1\mu$m, while $PC = 93.07\%$, $ER = -11.3$dB for $\Delta h = 0.1\mu$m, the conversion efficiencies improve to $PC = 96.15\%$,

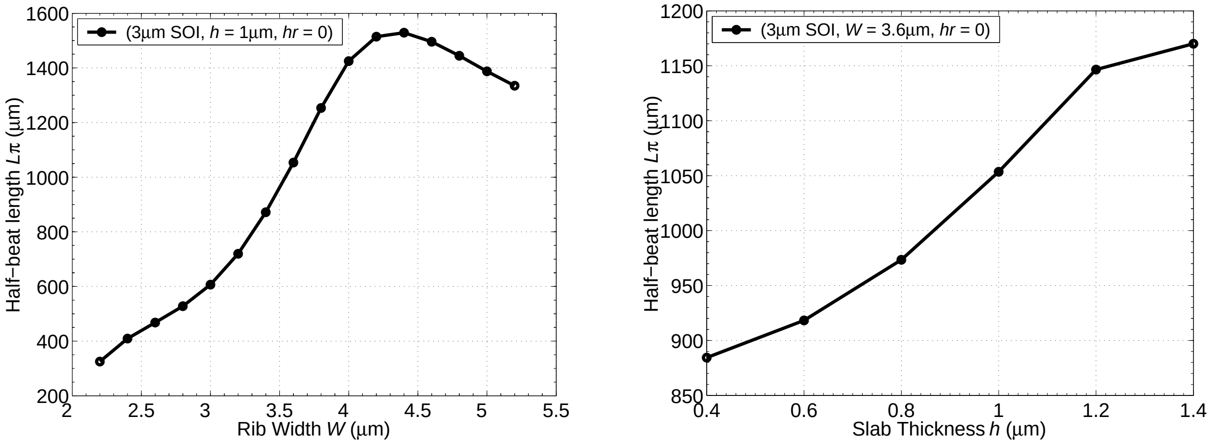

(a) (b)

Figure 5.1: The variation of the half-beat length L_π variation with respect to: (a) the width W of the rib base for an external waveguiding layer thickness for $h = 1\mu$m; and (b) h for $W = 3.6\mu$m.

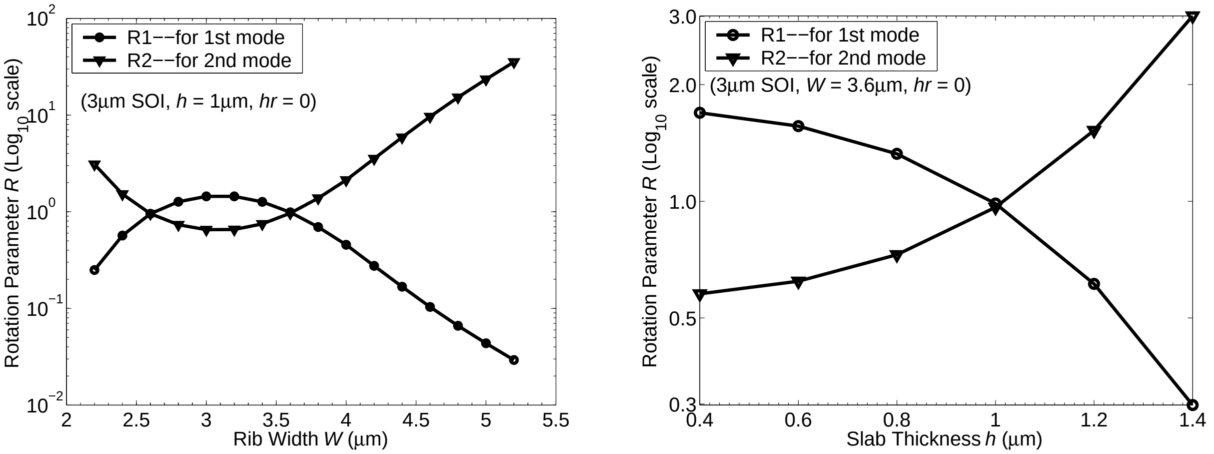

(a) (b)

Figure 5.2: Optical-axis rotation parameters R_1 and R_2 as a function of: (a) the width W of the rib base for an external waveguiding layer thickness $h = 1\mu$m; and (b) the external layer thickness h for a rib base width $W = 3.6\mu$m.

$ER = -14$dB for $\Delta W = 0.05\mu$m while $PC = 97.62\%$, $ER = -16$dB for $\Delta h = 0.05\mu$m. These compare favorably to the conversion values of 80% in 0.3mm device of [15], 85% and 45% in [21]. Since the modes of the SOI waveguides are highly confined and are therefore more influenced by geometric variations, the fabrication tolerance of the SOI rotator is slightly less than that of InGaAsP converters with equivalent guiding layer thicknesses (c.f. Fig.5 of [47]). However, ultra-compact SOI devices are more easily fabricated than similar III-V structures, which can possess certain dimensions below 50nm (c.f., Fig.2 of [15], and Fig.1 of [28] where $L_\pi = 230\mu$m). Improved silicon fabrication methods with 0.05μm resolution, possibly involving nano-photonics processing techniques [200–206], should result in ultra-short polarization rotators with conversion efficiency $> 96\%$.

5.3 Tolerance Study of Two Practical SOI PRs

In this and the next section, we consider the fabrication tolerance and wavelength stability of two asymmetrical external waveguiding layer slanted angle SOI polarization rotators which are of practical importance. These are a 3μm design with $H = 2.8\mu$m, $h = 1\mu$m, $W = 2.7\mu$m, $h_r = 0$, $R = 1.04$, and $L_\pi = 502.4\mu$m, and a 5μm design with $H = 4.8\mu$m, $h = 1.8\mu$m, $W = 4.8\mu$m, $h_r = 0$, $R = 1.01$, and $L_\pi = 2572\mu$m. The geometric parameters are rounded to the nearest tenth of a micron-meter, which models the fabrication precision in our low cost silicon processing [7]. Further, the values of H are reduced by 0.2μm from the optimal film thicknesses specified above to model the 0.2μm silicon layer loss observed experimentally after removing the top protecting layer during fabrication [7, 8]. It should be noted that improved technologies provide much better precision [200–206] such as ±50nm [200], ±20nm [204, 206] or several nanometers [201].

We first study in Fig. 5.3 the variation of the polarization conversion efficiency (PC) with respect to the base rib width W for these two devices. For the 5μm design, the PC degrades only 1% for $\pm0.1\mu$m deviation from the optimum rib width 4.8μm; while this degradation is about 2.5% for the 3μm design. The fabrication tolerance regarding to the thickness of outer-slab layer h is displayed in Fig. 5.4, from which one conclude that the variation of the external waveguiding layer thickness has a larger effect on the device performance. A $\pm0.1\mu$m variation of h from its optimal value reduces the polarization

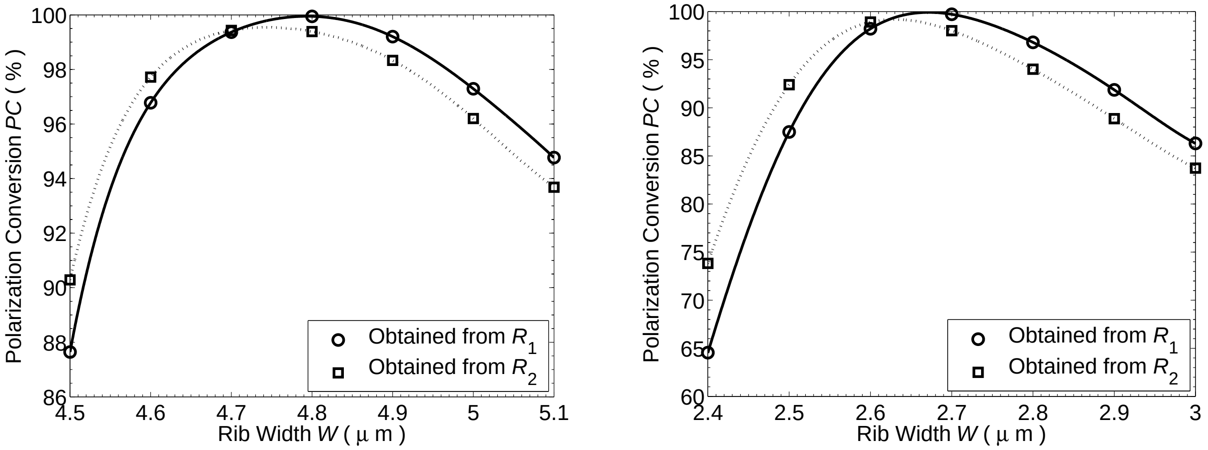

(a) (b)

Figure 5.3: Variation of the polarization conversion efficiency with the based rib width for: (a) 5μm design; and (b) 3μm design.

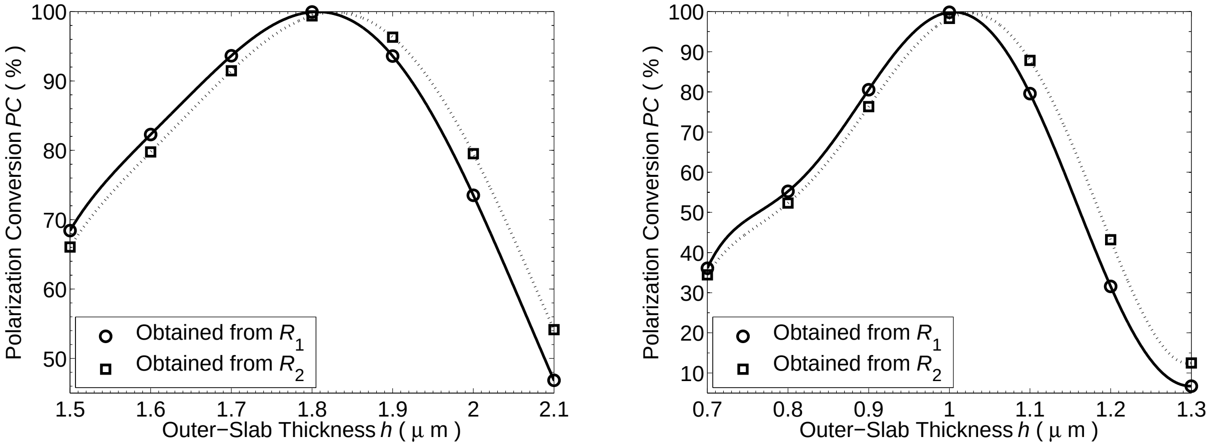

(a) (b)

Figure 5.4: Variation of the polarization conversion efficiency with the outer-slab thickness for: (a) 5μm design; and (b) 3μm design.

conversion efficiency by 5% for the 5μm device and 18% for the 3μm device. Therefore, in the fabrication, the control of outer-slab thickness should be more precise than that of rib width. However, considering a better fabrication precision of ±20nm [204, 206], the performance degradation of the 3μm device dramatically improves to less than 3%. In Figs. 5.3 and 5.4, each plot has two curves, which are obtained from the rotation parameters R_1 and R_2 of the two fundamental modes, respectively. The difference between these two sets of results are really small, indicating an excellent similarity of the field distributions. Figs. 5.3 and 5.4 consider the absolute variation of width or heights, therefore the relative error from the optimal values cannot be established. In Fig. 5.5 the geometric variations in terms of percentage error from the optimal values of rib width, outer-slab thickness and silicon guiding layer height are studied. From Fig. 5.5, we find that 5% variation in these geometric parameters leads to no more than 5% reduction in the polarization conversion efficiency.

Next, we analyze in Fig. 5.6 the degradation of the polarization conversion efficiency with respect to the variation of the angles of the rib sidewalls. Fig. 5.6(a) studies the angle of the slated-facet, which equals to 54.736° for etching along the $\langle 111 \rangle$ crystal plane of silicon. A 1° error in this slant angle lowers PC by 3%; however, since the slope sidewall of the rib can be made very precisely by tetramethyl ammonium hydroxide (TMAH) procedure [7, 8] we need not worry about this variation at all. The only one to be considered seriously is the angle of the vertical wall, whose effect on the device performance is illustrated in Fig. 5.6(b). We see that a 5° off from the exact 90° causes 6% reduction in PC, while a 10° deviation leads to 25% degradation or more. Therefore, for practical yet economic considerations, a fabrication technology which controls this angle within ±5° precision should be chosen for the fabrication of slanted-angle polarization rotators; otherwise, one may have to adjust the geometric parameters H, W, or h in advance to compensate this degradation by using the general design procedures discussed earlier in Chapter 4.

Finally, we consider the variation of the refractive index of the silicon guiding film as a result of different doping density. Since the refractive index difference between the silicon ($n_1 = 3.48$) and silicon oxide ($n_2 = 1.45$) is rather large, the small change in the refractive index of silicon layer has little effect on the device performance, as obvious from

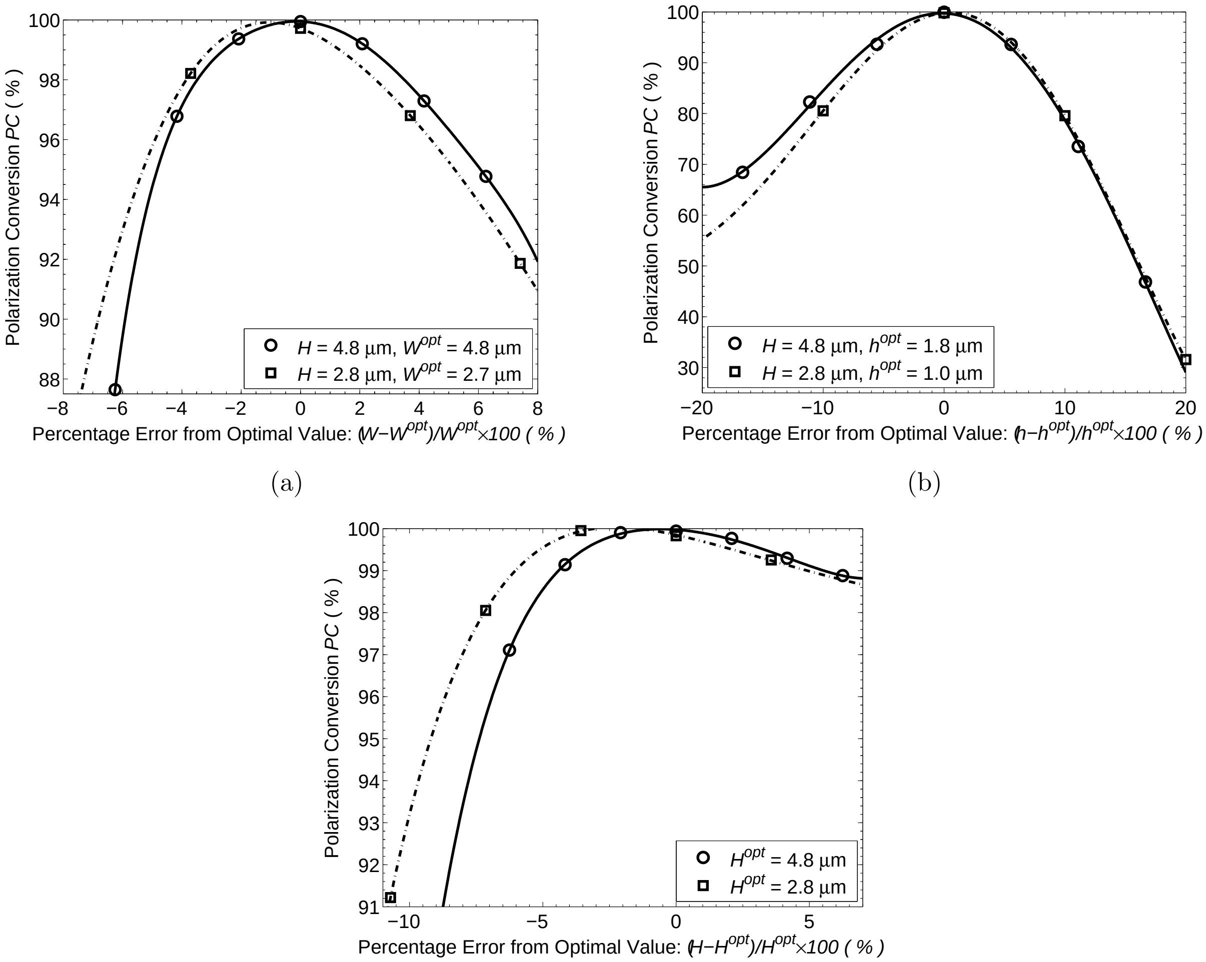

(a)

(b)

(c)

Figure 5.5: Variation of the polarization conversion efficiency with the percentage error from optimal value for: (a) rib width W; (b) outer-slab thickness h; and (c) silicon guiding layer thickness H.

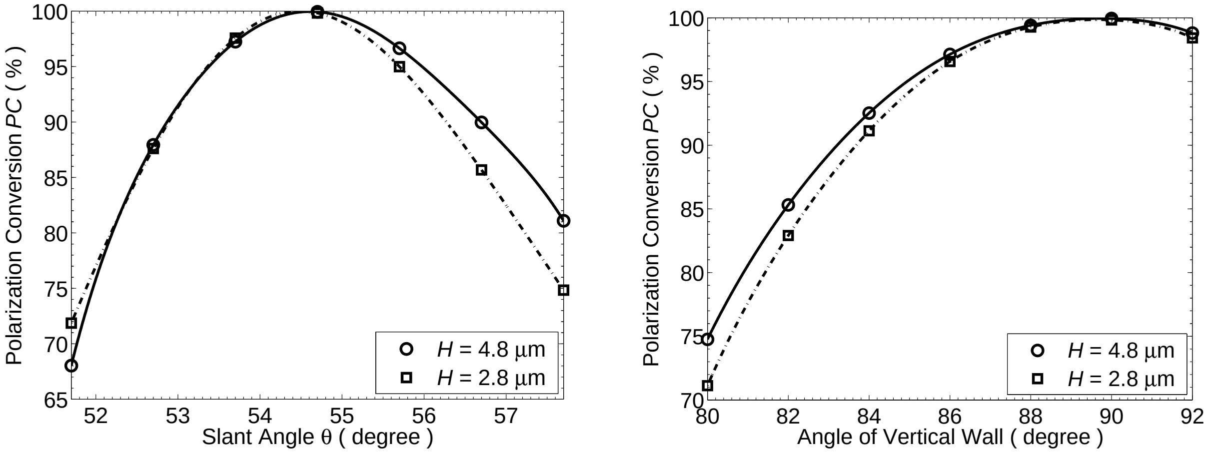

(a) (b)

Figure 5.6: Variation of the polarization conversion efficiency with the rib angle: (a) angle of the sloped wall; and (b) angle of the vertical wall.

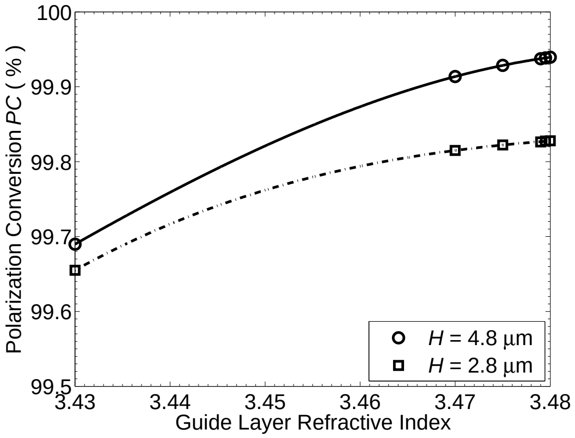

Figure 5.7: Variation of the polarization conversion efficiency with the refractive index of the silicon guiding layer.

Fig. 5.7. If the index is modified to 3.43 instead of 3.48, there is only 0.3% reduction in the polarization conversion efficiency. As a comparison, the variation in index contrast could lead to dramatic performance changes for polarization converters made from low-index-contrast III-V semiconductors [49, 50].

5.4 Spectral Properties

To determine the applicability of the polarization rotator design to Wavelength Division Multiplexing (WDM) systems, we now study the behavior of the two representative devices in the C-band (1528.77nm∼1563.86nm) and L-band (1573.71nm∼1604.03nm), as defined by the International Telecommunications Union Telecommunication Standardization Sector (ITU-T) G.692 standard.

In Figs. 5.8(a) and 5.8(b) we respectively display R and L_π as a function of wavelength for the 3μm design. In a wavelength range of 1.50μm to 1.60μm the rotation parameter R varies by ±0.5% from its center value at 1.55μm, corresponding to a maximum change of 0.15° in the optical-axis rotation angle while L_π varies by ±6%. While between 1.55 and 1.60μm the variation of R is far smaller than the 6% predicted for the III-V converter in Fig.12 of [50], L_π varies slightly more than the 5% reported in this reference.

The polarization conversion efficiencies and crosstalk for $1.50 < \lambda < 1.60\mu$m for the 3μm and 5μm components are plotted together in Fig. 5.9. Although in principle a 3μm rotator can display the same performance as the 5μm device with $PC = 99.98\%$ and $ER = -37$dB, for 0.1μm fabrication tolerance, the larger layer thickness is clearly preferable. That the SOI polarization converters are highly wavelength-independent is evident from $PC > 99\%$ in the wavelength range of $1.50 < \lambda < 1.60\mu$m, while $PC > 99.7\%$ in the C-band where the 3μm and 5μm components display < -25dB and < -30dB polarization crosstalk, respectively.

As a result, the insensitivity to wavelength fluctuation makes the SOI polarization converters quite suitable for Dense Wavelength Division Multiplexing (DWDM) applications and Planar Lightwave Circuit (PLC).

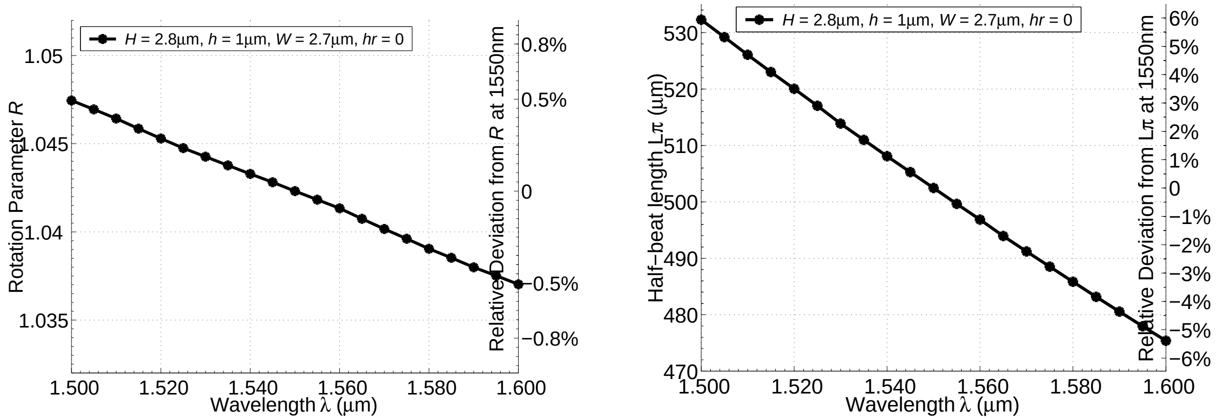

(a) (b)

Figure 5.8: The wavelength dependence of (a) the rotation parameter (optical-axis rotation angle) and (b) the half-beat length (required device length).

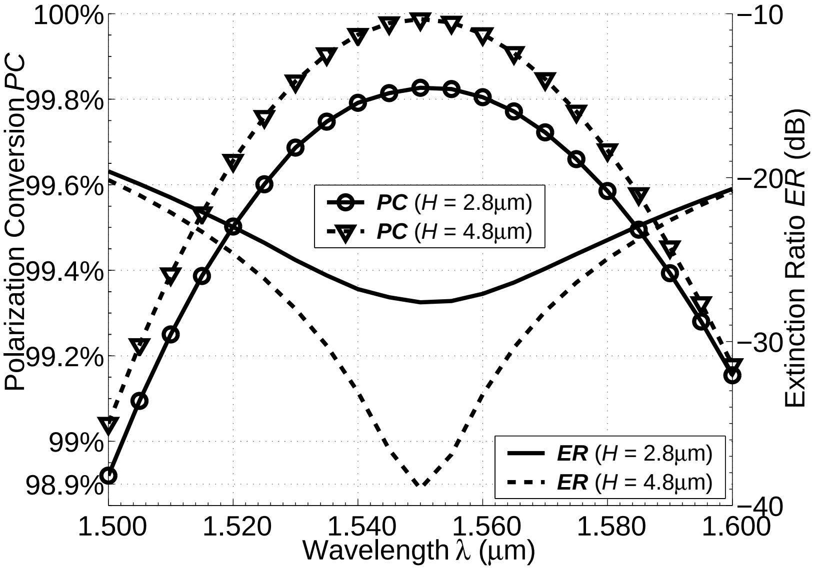

Figure 5.9: The wavelength dependence of the polarization conversion efficiency and polarization extinction ratio for the 3μm and 5μm designs.

5.5 Fabricated Devices

The fabrication of asymmetric slanted-angle SOI polarization converters was finished by Chris Brooks and Prof. Paul E. Jessop at McMaster University [8]. The manufacturing was jointly collaborated with Prof. Garry Tarr at Carleton University, who provided high quality plasma etching systems for silicon. The SOI wafer was manufactured by the bond and etch-back technique (BESOI), and the oxide mask was patterned by ultraviolet photolithography and reactive ion etching (RIE). The vertical rib wall was etched with electron cyclotron resonance reactive ion (ECR-RIE); while the angled-facet of the device was obtained with tetramethyl ammonium hydroxide (TMAH) wet etching along the $\langle 100\rangle$ direction of the silicon, exposing the $\langle 111\rangle$ crystallographic plane.

The Scanning Electron Microscope (SEM) graphs of two fabricated device samples [8] of 3μm and 5μm devices are shown in Figs. 5.10(a) and 5.10(b), respectively. Measured waveguide parameters are illustrated in Fig. 5.10; and for comparison, desired optimum values are shown in brackets. Due to blurred edges in the SEM graphs, measurement error is $\pm 0.1\mu$m for lengths and heights, and $\pm 1^\circ$ for sidewall angles [8]. As shown in Fig. 5.10(c), the angled-facet along the crystal angle is very smooth by wet chemical etching; however, unavoidable vertical wall roughness could lead to unpredictable degradation of the device performance.

The measured excess loss of the 5μm polarization rotator is only 0.6 ± 0.1dB/mm and 0.5 ± 0.1dB/mm for TE- and TM-input, respectively [8]. Without considering the error in sidewall angles, the optical-axes rotation of the 3μm device with $(H, W, h, h_r) = (3.1, 2.7, 1.2, 0)$ is estimated from Fig. 4.2(b) or Fig. 4.4(c) to be about 30°, leading to a maximum polarization conversion efficiency (PC) of 75% according to Eq. (5.2). For the 5μm device with $(H, W, h, h_r) = (5.0, 4.9, 1.9, 0)$, the estimations are 35° optical-axes rotation and 88% maximum PC from Fig. 4.4(d) and Eq. (5.2). However, in the experimental results in [8], the measured maximum PC is 78% for TE $\rightarrow$ TM conversion. The 10% difference between the prediction and experimental results may arise from the $\pm 0.1\mu$m measurement precision, the deviation of sidewall angles, the roughness of sidewalls, the nonuniform of outer-slab thickness, and the imperfect cleaving of the sample, etc. A more detailed study of the device performance will be presented in Section 6.5 by illustrating the polarization conversion effects along the propagation direction.

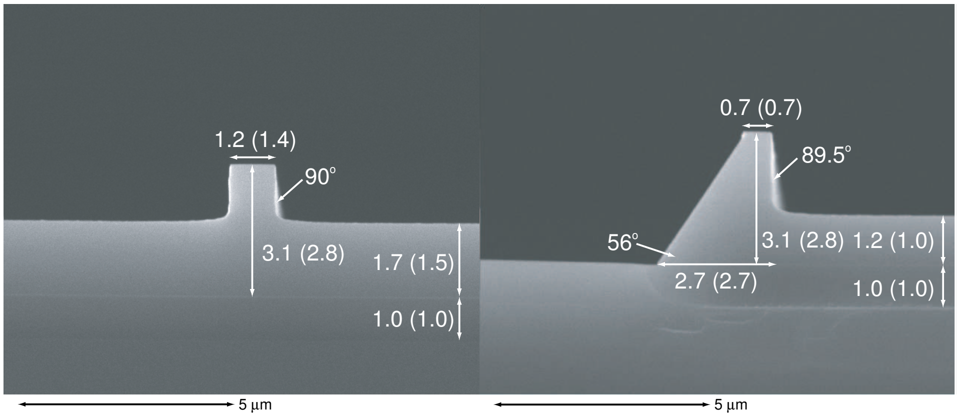

(a) 3μm device

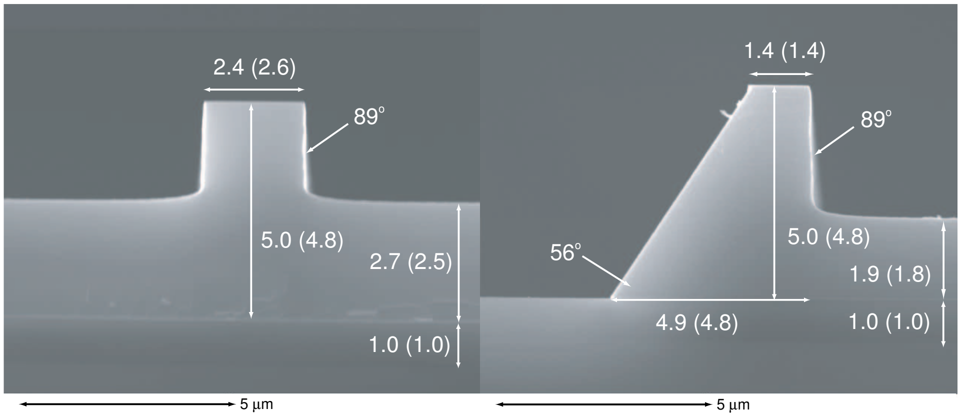

(b) 5μm device

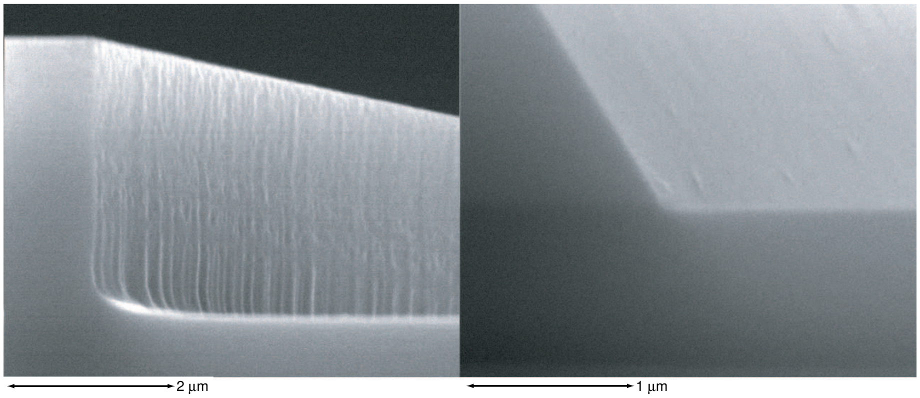

(c) sidewall roughness of the 5μm device

Figure 5.10: SEM images of fabricated SOI polarization converters. (After [8])

5.6 Summary

In summary, slanted-angle polarization converters fabricated on SOI have stronger tolerance to geometric variations as compared with III-V counterparts. Among all these parameters, the thickness of the outer-slab layer and the perfectness of the vertical sidewall contribute more to the variation of the device performance; while the refractive index of the silicon guiding film has the least effect on the performance fluctuation.

Additionally, such components display small coupling losses (0.2dB), flat spectral response ($|\Delta R| < 0.5\%$ for $1.50 < \lambda < 1.60\mu$m), high conversion efficiency (99.98%) and low polarization extinction ratio (-38dB). SOI polarization rotators, which can easily be produced with electronic device fabrication technology, should therefore find numerous applications in Photonic Integrated Circuit (PIC) and Dense Wavelength Division Multiplexing (DWDM) systems.

While our design methodology enables, at least in principle, the design of short polarization rotators with nearly 100% polarization conversion and < -30dB extinction ratio, the realization of short ($< 100\mu$m) components can require technological precision of 0.05μm (50nm) or less.

Fabricated SOI polarization rotators from low-cost silicon processing have already shown strong conversion efficiency as predicted, and can be further improved with more advanced processing techniques.

Chapter 6

FE-BPM Analysis

Eigenmode solvers (guided-mode analysis) [113–115] play an important role in finding stationary solutions for z-invariant waveguides or in obtaining local normal modes for z-variant devices. However, to study the propagation characteristics of a z-variant optical waveguide, such as taper [145, 161, 162, 207–217], Y-branch [82] or Mach-Zehnder Interferometer (MZI) [79, 80], the Beam Propagation Method (BPM) [141–146] analysis is mandatory.

In this chapter, procedures related to the Finite-Element Beam-Propagation Method (FE-BPM) are first discussed in Section 6.1. The anisotropic Perfectly Matched Layer (PML) boundary condition (BC) essential for absorbing outgoing waves is subsequently introduced in Section 6.2, and its efficiency is verified with both straight and tilted Gaussian beam propagations. In Section 6.3, the intrinsic non-unitarity associated with the propagation operator is carefully studied. BPM calculations of polarization conversion and power exchange in an asymmetric SOI PR are presented in Section 6.4. Finally, experimentally measured results are compared with theoretical propagation in Section 6.5.

6.1 FEM Beam Propagation Method

Due to their versatility and efficiency, BPM algorithms employing finite-element procedures (FE-BPM) are superior to finite-difference BPM (FD-BPM) [129] and fast-Fourier-transform BPM (FFT-BPM) schemes [147] in analyzing anisotropic, inhomogeneous, or arbitrary-cross-section waveguides.

6.1.1 FE-BPM Numerical Scheme

Using an approximate reference refractive index n_0 (the closer to effective index n_{eff}, the better) and slowly varying envelop approximation (SVEA) [125], the field has the form

$$\psi = \phi(x, y, z) \exp(-jk_0 n_0 z) \tag{6.1}$$

with an implied time dependence $\exp(j\omega t)$.

After applying finite-element procedures to the transverse xy-plane, the following matrix equation is obtained

$$[M]\frac{d^2\{\phi\}}{dz^2} - 2jk_0n_0[M]\frac{d\{\phi\}}{dz} + \left([K] - k_0^2n_0^2[M]\right)\{\phi\} = \{0\} \tag{6.2}$$

where $[K]$ and $[M]$ are given in Eqs.(3.11-3.12), Eqs.(3.20-3.21), and Eq.(3.42) for scalar, semi-vectorial and full-vectorial analysis, respectively. Utilizing the Fresnel approximation for paraxial analysis,

$$\frac{d^2\{\phi\}}{dz^2} = 0 \tag{6.3}$$

or utilizing the Padé recurrence relation [125, 153, 218, 219] by rewriting Eq.(6.2) to

$$2jk_0n_0[M]\frac{d\{\phi\}}{dz} = \frac{\left([K] - k_0^2n_0^2[M]\right)\{\phi\}}{1 - \frac{1}{2jk_0n_0}\frac{d}{dz}} \tag{6.4}$$

for wide-angle analysis, we obtain

$$-2jk_0n_0[\widetilde{M}]\frac{d\{\phi\}}{dz} + \left([K] - k_0^2n_0^2[M]\right)\{\phi\} = \{0\} \tag{6.5}$$

where

$$[\widetilde{M}] = \begin{cases} [M] + \frac{1}{4k_0^2n_0^2}\left([K] - k_0^2n_0^2[M]\right), & \text{for wide-angle analysis} \\ [M], & \text{for paraxial analysis} \end{cases} \tag{6.6}$$

We find from Eq.(6.5) that the z derivative can be expressed as

$$\frac{d}{dz} = \frac{1}{2jk_0n_0}[\widetilde{M}]^{-1}\left([K] - k_0^2n_0^2[M]\right) \tag{6.7}$$

Since the z-derivative of an eigenmode (stationary solution) is zero, for guided-mode analysis Eq.(6.5) exactly reduces to the eigenmode matrix equation of Eqs.(3.10), (3.19) and

(3.41). However, for propagation-field analysis, applying Galerkin's procedure along the longitudinal direction leads to

$$[A]_k\{\phi\}_{k+1} = [B]_k\{\phi\}_k \tag{6.8}$$

with

$$\begin{aligned} [A]_k &= -2jk_0n_0[\widetilde{M}]_k + \alpha\Delta z\left([K]_k - k_0^2n_0^2[M]_k\right) && (6.9) \\ [B]_k &= -2jk_0n_0[\widetilde{M}]_k - (1-\alpha)\Delta z\left([K]_k - k_0^2n_0^2[M]_k\right) && (6.10) \end{aligned}$$

where Δz is the propagation step-size, and the subscripts k and $k+1$ denote the k-th and $(k+1)$th propagation steps, respectively. The weighting factor (difference parameter) α is related to program stability, and $\alpha \geq 0.5$ is the stability range of the propagation scheme [220]. In the Crank-Nicholson algorithm $\alpha = 0.5$, the power dissipation is the least but unstable results may appear for full-vectorial BPM due to the intrinsic non-self-adjointness of the full-vectorial propagation operator [2]. The quasi-Crank-Nicholson scheme [129] with $\alpha = 0.5 + \epsilon$, where ϵ is a very small positive value, is usually stable because of the small artificial power dissipation.

To increase the numerical accuracy and efficiency, the reference refractive index n_0 is renewed after each step [197, 221]

$$n_0 = \frac{\{\phi^*\}^T[K]\{\phi\}}{k_0^2\{\phi^*\}^T[M]\{\phi\}} \tag{6.11}$$

so as to make it as close to the effective index of the local normal mode as possible. For simplicity, one can take the real part of Eq. (6.11) as the reference index [194], however, the complex reference index minimizes the numerical error [221].

As seen from Eqs. (3.10), (3.19) and (3.41), we have generalized the FEM eigenmode problem into the same generalized eigenvalue matrix equation $\left([K] - \beta^2[M]\right)\{\phi\} = \{0\}$ for scalar (SC-), semi-vectorial (SV-) and full-vectorial (FV-) analysis. In the generalized propagating-beam matrix problem Eq. (6.8), SC-BPM, SV-BPM and FV-BPM are therefore distinguished by the corresponding FEM global matrices.

6.1.2 Imaginary-Distance BPM as Eigenmode Solver

In addition to the propagation-field analysis, BPM has also been widely employed for the guided-mode analysis [115, 128, 222–224]. The impetus for this mostly came from the fact that directly solving large-scale generalized eigenvalue matrices could require tremendous computer memory and CPU time when one does not have an efficient eigenvalue solver. Using iterative eigenvalue solvers [122, 184–186] could be one solution, and employing iterative propagation schemes could be another effectively way to find eigenmodes.

The imaginary-distance beam-propagation method (ID-BPM) [222–224] has been widely accepted as an efficient eigenmode solver. After propagating the field along the imaginary axis for a few steps, the resultant converged field is the fundamental mode of an optical waveguide, since the amplification factor for this mode is the largest. This technique can be generalized for higher order modes [222, 225–228]. Denoting the effective index and the corresponding field of the i-th eigenmode as $n_{eff,\,i}$ and h_i, from Eq. (3.41) we have

$$[K]\{h_i\} - \beta^2[M]\{h_i\} = \{0\} \tag{6.12}$$

After the k-th step according to Eq. (6.8), field distribution of the i-th mode becomes

$$\{h_i\}_{k+1} = \frac{-2jk_0n_0 - (1-\alpha)\Delta z k_0^2\left(n_{eff,\,i}^2 - n_0^2\right)}{-2jk_0n_0 + \alpha\Delta z k_0^2\left(n_{eff,\,i}^2 - n_0^2\right)}\{h_i\}_k \tag{6.13}$$

If there are N eigenmodes in the waveguide, the field $\{\phi\}_k$ at the k-th propagation step is $\{\phi\}_k = \sum\limits_{i=1}^{N} C_{i,k}\{h_i\}$, where $C_{i,k}$ is the complex weight factor. After sufficient steps, $\{\phi\}_k$ will converge to the eigenmode $\{h_i\}$ if the propagation step-size is chosen imaginary as

$$\Delta z = j\frac{4n_0}{k_0\left(n_{eff,\,i} - n_0^2\right)} \tag{6.14}$$

The effective index $n_{eff,\,i}$ can be obtained according to a similar pattern as Eq. (6.11). To calculate the m-th higher-order mode, all lower-order components should be filtered out from the initial input field such that

$$\{\phi\}_k^{new} = \{\phi\}_k - \sum_{i=1}^{m-1}\frac{\{h_i^*\}^T[M]\{\phi\}_k}{\{h_i^*\}^T[M]\{h_i\}}\{h_i\} \tag{6.15}$$

Using $\{\phi\}_k^{new}$ as a new starting field, it will converge to the desired m-th higher-order mode; while without this filtering procedure the field will converge to the fundamental mode.

6.2 Perfectly Matched Layer Boundary Condition

In the propagation-field analysis, absorbing boundary conditions (ABC) [121] and transparent boundary conditions (TBC) [229] are generally employed to reduce field reflections; however, most recently a new anisotropic absorbing layer called perfectly matched layer (PML) [230–239] has been introduced to efficiently eliminate the field reflection at computational windows.

Bérenger [230] first introduced the PML to absorb outgoing radiation field by dividing the magnetic field component H_z into two subcomponents H_{zx} and H_{zy}, so that the interface of PML and free space is refectionless for all wavelengths, polarizations and incident angles. However, Bérenger's technique violates the Maxwell's equation therefore Sacks [231] instead used the anisotropic material properties (ε, μ, σ_E, σ_H) to describe the absorbing PML layer, where ε and μ are the permittivity and permeability, respectively, and σ_E and σ_H are the electric and magnetic conductibility, respectively.

6.2.1 Impedance Matching Condition

Considering the complex diagonal relative permittivity and permeability tensors

$$[\varepsilon_r] = \begin{bmatrix} \varepsilon_r^x + \frac{\sigma_E^x}{j\omega} & 0 & 0 \\ 0 & \varepsilon_r^y + \frac{\sigma_E^y}{j\omega} & 0 \\ 0 & 0 & \varepsilon_r^z + \frac{\sigma_E^z}{j\omega} \end{bmatrix}, \ [\mu_r] = \begin{bmatrix} \mu_r^x + \frac{\sigma_H^x}{j\omega} & 0 & 0 \\ 0 & \mu_r^y + \frac{\sigma_H^y}{j\omega} & 0 \\ 0 & 0 & \mu_r^z + \frac{\sigma_H^z}{j\omega} \end{bmatrix} \tag{6.16}$$

to match the intrinsic impedance of the free space, the condition

$$\frac{\varepsilon_0 \, [\varepsilon_r]}{\varepsilon_0} = \frac{\mu_0 \, [\mu_r]}{\mu_0} \tag{6.17}$$

should be satisfied. Therefore,

$$[\varepsilon_r] = [\mu_r] = \begin{bmatrix} a & 0 & 0 \\ 0 & b & 0 \\ 0 & 0 & c \end{bmatrix} = [\Lambda] \tag{6.18}$$

Here, $a = \varepsilon_r^x + \frac{\sigma_E^x}{j\omega} = \mu_r^x + \frac{\sigma_H^x}{j\omega}$, $b = \varepsilon_r^y + \frac{\sigma_E^y}{j\omega} = \mu_r^y + \frac{\sigma_H^y}{j\omega}$, and $c = \varepsilon_r^z + \frac{\sigma_E^z}{j\omega} = \mu_r^z + \frac{\sigma_H^z}{j\omega}$.

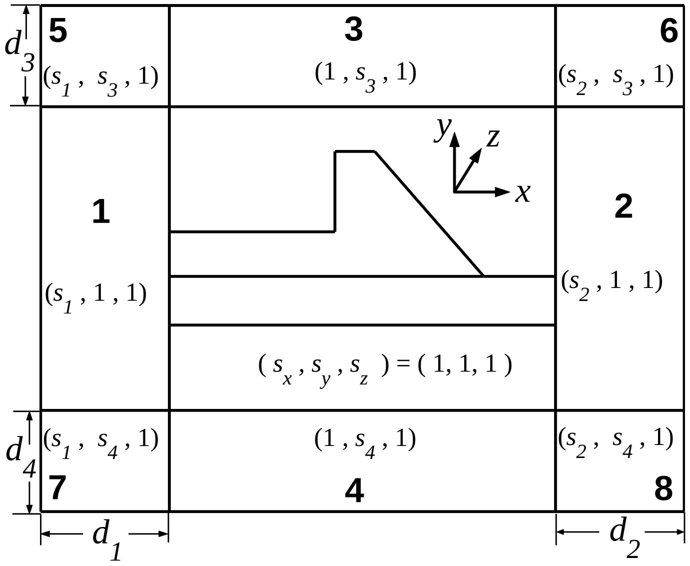

Figure 6.1: SOI polarization converter surrounded by perfectly matched layer (PML).

By studying the reflection coefficients for interfaces of PML region and the free space, we find that in certain circumstances the reflection could be zero. For the PML region with an interface where $x = const$ and $y = const$, $[\Lambda]$ is required to be [123, 232, 234]

$$[\Lambda]_x = \begin{bmatrix} a & 0 & 0 \\ 0 & \frac{1}{a} & 0 \\ 0 & 0 & \frac{1}{a} \end{bmatrix} \text{ for } x = const \text{ , and } [\Lambda]_y = \begin{bmatrix} \frac{1}{b} & 0 & 0 \\ 0 & b & 0 \\ 0 & 0 & \frac{1}{b} \end{bmatrix} \text{ for } y = const \tag{6.19}$$

For the PML regions at the four corners of the computational window, the PML tensor is obtained by the products of the above two tensors as

$$[\Lambda]_{xy} = [\Lambda]_x \cdot [\Lambda]_y = \begin{bmatrix} \frac{a}{b} & 0 & 0 \\ 0 & \frac{b}{a} & 0 \\ 0 & 0 & \frac{1}{ab} \end{bmatrix} \text{ for PML corners} \tag{6.20}$$

6.2.2 Determination of PML Parameters

For the full-vectorial formulation in Section 3.2.3, we accordingly modify the permittivity- and permeability- tensors $[p]$ and $[q]$ to [226, 237–241]

$$[p] = [p] \cdot [s]^{-1} \text{ and } [q] = [q] \cdot [s] \tag{6.21}$$

where

$$[s] = \begin{bmatrix} \frac{s_y s_z}{s_x} & 0 & 0 \\ 0 & \frac{s_z s_x}{s_y} & 0 \\ 0 & 0 & \frac{s_x s_y}{s_z} \end{bmatrix} \text{ and } [s]^{-1} = \begin{bmatrix} \frac{s_x}{s_y s_z} & 0 & 0 \\ 0 & \frac{s_y}{s_z s_x} & 0 \\ 0 & 0 & \frac{s_z}{s_x s_y} \end{bmatrix} \tag{6.22}$$

When the PML parameters (s_x, s_y, s_z) are assigned for each PML region according to Fig. 6.1, the resulting permittivity- and permeability- tensors satisfy the conditions of Eqs. (6.19) and (6.20). For the non-PML regions, the PML tensor $[s]$ is an identity matrix; while in the PML regions the parameters are given by

$$s_i = 1 - j\frac{\sigma_E^{max}}{\omega\varepsilon_0\varepsilon_r^{PML}}\left(\frac{\rho}{d_i}\right)^m \ , \ i = 1, 2, 3, 4 \tag{6.23}$$

where ρ is the distance from the PML boundary, d is the thickness of the PML layer, and m controls the profile of the conductivity. Generally, linear ($m = 1$), *parabolic* ($m = 2$) and cubic ($m = 3$) conductivity profiles are assumed. The maximum electric conductivity σ_E^{max} and the permittivity of the PML layers are determined from the required reflection coefficient [230, 242] according to [243]

$$R_i = \exp\left(-\frac{2\sigma_E^{max} d_i}{3\varepsilon_0 c\sqrt{\varepsilon_r^{PML}}}\right) \tag{6.24}$$

Where R_i is the reflection coefficient of the i-th PML region and c is the light velocity in vacuum. Typically R_i is chosen in the order of 10^{-4} [243] and σ_E^{max} is in the order of $0.01\Omega^{-1}(\mu\text{m})^{-1}$ [232, 242, 244] when the permittivity is chosen as one.

Repeating the above analysis for the semi-vectorial analysis in Section 3.2.2, we simply need to modify the permittivity and permeability in Eqs. (3.20) and (3.21) as

$$p_x = p_x\frac{s_y}{s_x^3} \ , \ p_y = p_y\frac{1}{s_x s_y} \ , \ p_z = p_z\frac{s_y}{s_x} \ , \text{ and } \ q = q\frac{s_y}{s_x} \tag{6.25}$$

The parameters (s_x, s_y, s_z) are still all ones for non-PML regions and assigned according to Fig. 6.1 for PML regions.

The technique of applying transformations of Eqs. (6.21) and (6.25) is intrinsically equivalent to modify the nabla operator of Eq. (3.23) to

$$\nabla^s = \boldsymbol{i}_x s_x \frac{\partial}{\partial x} + \boldsymbol{i}_y s_y \frac{\partial}{\partial y} + \boldsymbol{i}_z s_z \frac{\partial}{\partial z} = \nabla_t^s + \boldsymbol{i}_z s_z \frac{\partial}{\partial z} \tag{6.26}$$

However, this does not introduce extra programming complexity, since all the following procedures related to eigenmode solver and propagation technique remain unchanged.

6.2.3 Efficiency of PML Boundary Condition

To test the efficiency of the PML absorber, we compare the Gaussian beam propagation in the free space with both Neumann and PML boundary conditions (BC). The free space region is a $12\mu\text{m} \times 12.3\mu\text{m}$ rectangular region, and the input TM-polarized Gaussian beam has a mode field diameter (MFD) [232, 245] of 4μm.

First, we display in Fig. 6.2(a) an off-axis Gaussian beam propagation in the free-space when the boundary condition is chosen as Neumann BC. The input beam is launched at an angle of 30° with respect to the longitudinal axis on the (x, z)-plane. Obviously, the beam is reflected when approaching the computational boundary and after some distance the reflection strongly interferes with the incident beam, although the total power within the computational window is conserved. As a result, this introduces tremendous error to the BPM calculations. In contrast, when the free space is surrounded by the anisotropic PML absorber, at the interface of the PML and the free space, the reflection is completely eliminated, as obvious in Fig. 6.2(b). In this calculation, the propagation step $\Delta z = 0.1\mu$m, and the conductivity distribution inside the PML region has a parabolic profile (i.e., $m = 2$ in Eq. (6.23)) with a maximum value $\sigma_E^{max} = 0.07(\Omega^{-1}\cdot\mu\text{m}^{-1})$ at the computational window border.

Next, we launch the same Gaussian beam with zero phase tilt and show its propagation in Fig. 6.3(a). As the beam propagates, the mode field diameter of the Gaussian beam expands, and after some distance, the beam approaches the four free space boundaries simultaneously. However, we numerically realize reflectionless interfaces with the incorporation of anisotropic PML absorbers.

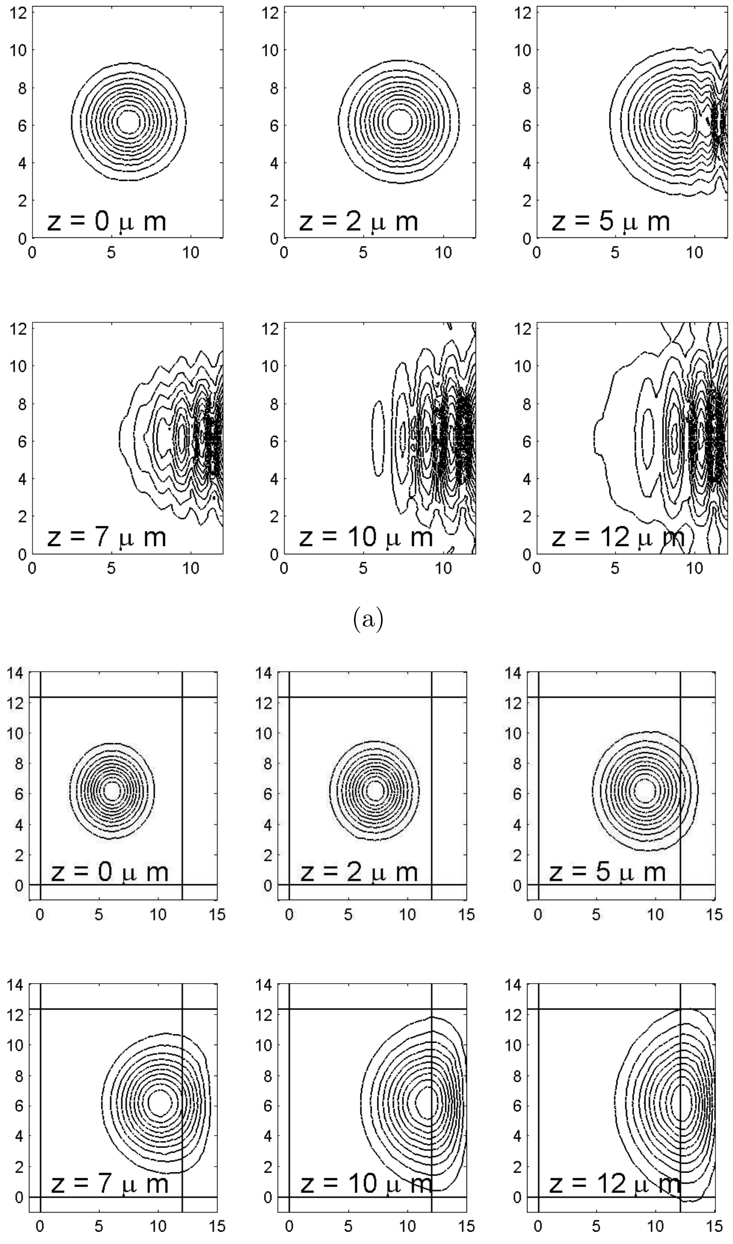

(a)

(b)

Figure 6.2: Off-axis Gaussian beam propagation in the free space: (a) Neumann boundary condition; and (b) PML boundary condition.

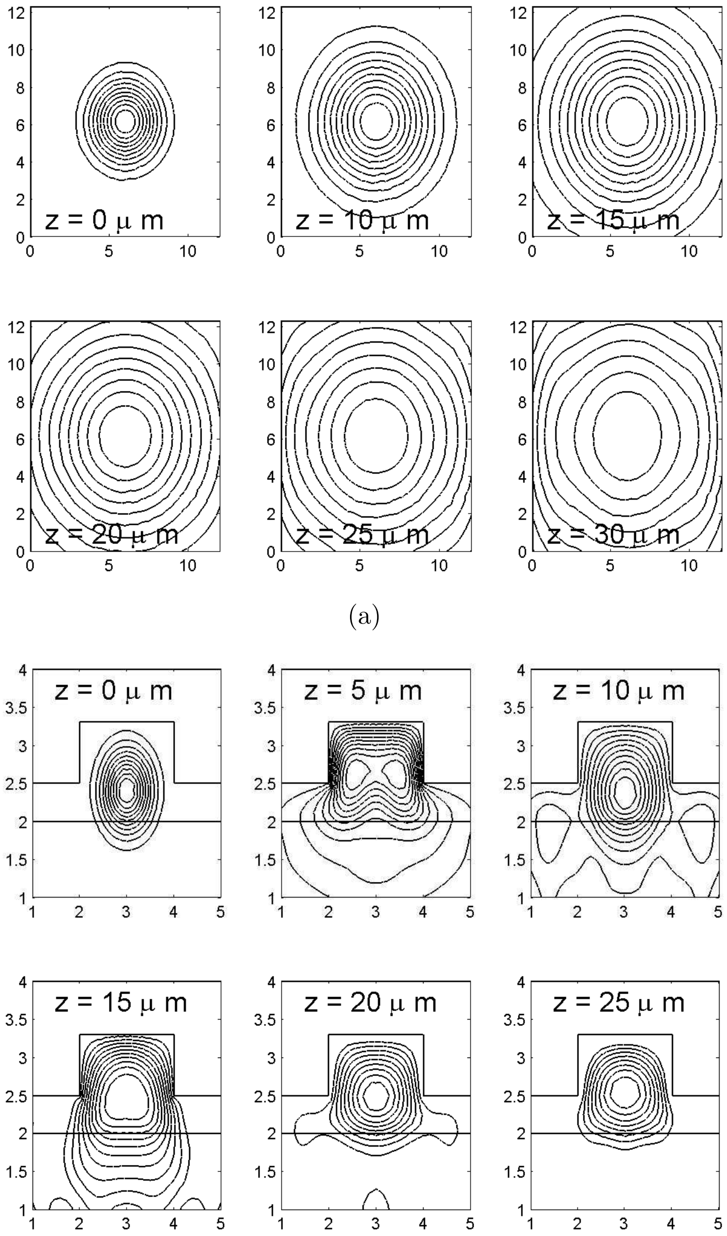

(a)

(b)

Figure 6.3: On-axis Gaussian beam propagation with PML boundary condition: (a) in the free space; and (b) in a rib waveguide.

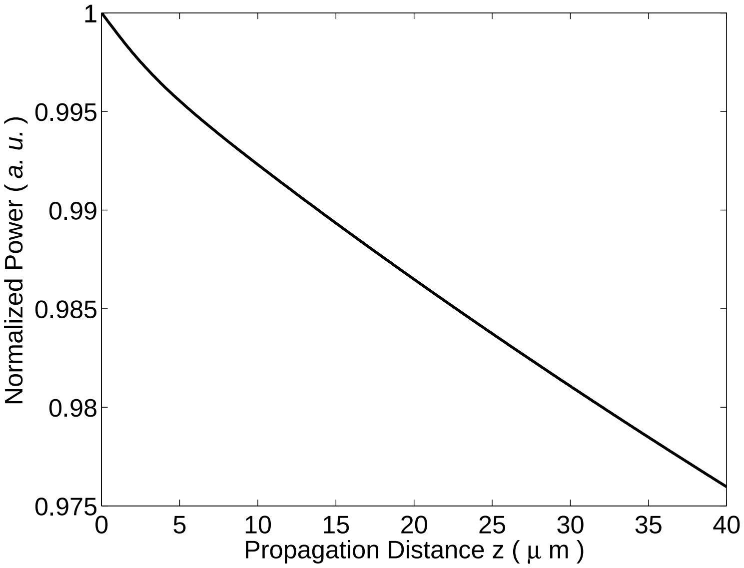

Figure 6.4: Variation of the normalized power in the window surrounded by the PML layer with respect to the propagation distance.

Finally, we study the Gaussian beam propagation in a rib waveguide with the PML boundary condition. The refractive indices of the rib waveguide are $n_1 = 3.44$ in the guiding region and $n_2 = 3.34$ in the substrate. The rib height, rib width and outer-slab thickness are $(H, W, h) = (1.3, 2, 0.2)$ μm, respectively. The Gaussian beam has a mode field diameter (MFD) of 1μm. As shown in Fig. 6.3(b), the input Gaussian beam is eventually coupled into the fundamental mode of the rib waveguide after sufficiently large distance.

As the anisotropic PML layer completely absorbs the field approaching the PML interface, there exists some power loss as shown in Fig. 6.4. However, since these field components usually come from high-order modes, the total power loss after 40μm propagation is only 0.0897dB in Fig. 6.4.

6.3 Non-Unitarity of BPM Algorithms

While numerous numerical simulations of optical devices have been performed with explicitly stable one-way scalar finite-difference electrical field propagation methods, electric field polarization evolution in complex waveguiding geometries is often better described by vectorial finite-element procedures. However, as discussed below, these intrinsically violate power-conservation. While this effect can be reduced by e.g., absorbing propagators or boundary conditions, power losses still cannot be reliably estimated.

6.3.1 Power Definition

The power per unit length transmitted by the waveguide is defined in terms of the Poynting vector [145]

$$P = \frac{1}{2}\Re\left(\iint_{-\infty}^{\infty} \boldsymbol{E}\times\boldsymbol{H}^{*}\cdot\boldsymbol{i}_z\,\mathrm{d}S\right) = \frac{1}{2}\iint_{-\infty}^{\infty}\left(E_xH_y^{*} - E_yH_x^{*}\right)\mathrm{d}S \tag{6.27}$$

where $\Re(\cdot)$ means taking the real part, and the asterisk means complex conjugate. For the Quasi-TE (E^x) and Quasi-TM (E^y) modes (Section 3.2.2), the power is

$$P_{\mathrm{TE}} = \frac{1}{2}\iint_{-\infty}^{\infty}\left(E_xH_y^{*}\right)\mathrm{d}x\,\mathrm{d}y = \frac{1}{2}\frac{n_{eff}}{Z_0}\iint_{-\infty}^{\infty}\left|E_x\right|^2\mathrm{d}x\,\mathrm{d}y \tag{6.28}$$

$$P_{\mathrm{TM}} = \frac{1}{2}\iint_{-\infty}^{\infty}\left(-E_yH_x^{*}\right)\mathrm{d}x\,\mathrm{d}y = \frac{1}{2}n_{eff}Z_0\iint_{-\infty}^{\infty}\frac{\left|H_x\right|^2}{n^2}\mathrm{d}x\,\mathrm{d}y \tag{6.29}$$

where $Z_0 = \sqrt{\frac{\mu_0}{\varepsilon_0}} = 376.73\Omega$ is the intrinsic impedance of vacuum.

Returning to the scalar and semi-vectorial FEM algorithms using nodal triangular elements described in Sections 3.2.1 and 3.2.2, the power is derived in terms of the eigenvalue matrices as

$$P = \{\phi^{*}\}^T[M]\{\phi\} \tag{6.30}$$

For the full-vectorial FEM scheme with mixed-type triangles as in Section 3.2.3, the power is

$$P = \{\phi_t^{*}\}^T[M_{tt}]\{\phi_t\} + \{\phi_t^{*}\}^T[M_{tz}]\{\phi_z\} \tag{6.31}$$

Note that in Eqs. (6.30) and (6.31), the constant related to the intrinsic impedance Z_0 is dropped for convenience, as it does not affect calculations of normalized power.

6.3.2 Intrinsic Non-Unitarity of FV-BPM

Researchers have tried to propose various unitary (power-conserving) BPM algorithms, however, they are limited to scalar cases and weakly guiding waveguides. Derived exactly from Maxwell's equation, the scalar Helmholtz equation for TE waves [141, 246, 247]

$$\left(\frac{\partial^2}{\partial x^2}+\frac{\partial^2}{\partial y^2}+\frac{\partial^2}{\partial y^2}+n^2k_0^2\right)\boldsymbol{E}=0 \tag{6.32}$$

can be transformed into power-conserving one-way propagation procedures [141, 246–248] although the field power is normally identified with e.g., the L_2 norm in the paraxial approximation, rather than the Poynting vector [145, 146, 197, 249]. On the other hand, the corresponding approach for TM waves generally violates power conservation when the derivative of the refractive index in the propagation direction is neglected [250] although methods have recently been found to include this term [251, 252].

By separating the transverse components from Eq. (3.22), a full vectorial (FV-) one-way description of the modes of a guided electromagnetic field is given by the magnetic field eigenvalue equation [129, 253]

$$\nabla_t^2\boldsymbol{H}_t+k_0^2n^2\boldsymbol{H}_t+\frac{1}{n^2}[\nabla_t n^2\times(\nabla_t\times\boldsymbol{H}_t)]=\beta^2\boldsymbol{H}_t \tag{6.33}$$

or the equivalent electric field formalism [146,253]. However, the third operator in the LHS (left-hand-side) of (6.33) is not self-adjoint in Hilbert space and hence neither symmetric nor Hermitian (c.f. [146,254] and Theorem 1 of [253]), and may contribute to the occurrence of complex modes [58, 253] in vectorial algorithms. This problem is especially severe at discrete index steps where field patterns may in certain circumstances become singular [250, 252]. As a result, in finite difference algorithms directly solving the differential form (6.33), matrices are non-Hermitian [129] once the third operator is included. However, in finite-element schemes with appropriate variational techniques [254], from the functional of (6.33) we can obtain the generalized eigenvalue equation (i.e., Eq. (3.41))

$$[K]\{\phi\}-\beta^2[M]\{\phi\}=\{0\} \tag{6.34}$$

with *symmetric sparse* matrices $[K]$ and $[M]$, which are real (therefore Hermitian) for lossless isotropic dielectrics subject to Dirichlet or Neumann boundary condition (BC), and complex (not Hermitian) for lossy anisotropic PML BC. Here $\{0\}$, β and $\{\phi\}$ represent the null vector, propagation constant, and $\boldsymbol{E}$ or $\boldsymbol{H}$ in the electric or magnetic field formalisms, respectively. For the mixed element procedure, $[K]$ and $[M]$ are constructed according to Eq. (3.42). With Crank-Nicholson scheme, i.e., $\dfrac{d\{\phi\}}{dz} = \dfrac{\{\phi\}\mid_{z+\triangle z} - \{\phi\}\mid_z}{\triangle z}$, the propagation pattern is constructed according to Eq. (6.8) by setting the weighting factor α to 0.5 in Eqs. (6.9) and (6.10).

When $[K]$ or $[M]$ is non-Hermitian, complex modes may present [58], resulting in divergences of associated propagation algorithms [141,250]. By introducing artificial dissipation into the Crank-Nicholson procedure [129] or applying highly absorbing boundary conditions [153], the divergence can generally be suppressed but physical losses then cannot be reliably estimated. Complex Padé approximations [153], or non-physical dissipative operators [249] are better techniques for ensuring stability but still possess the same intrinsic difficulty.

However, even though $[K]$ and $[M]$ are both real and symmetric, complex modes could still appear [58, 254]. This happens if neither $[K]$ nor $[M]$ is positive- or negative-definite [58]. In the mixed element procedure [181, 194, 255], the determinants of both $[K]$ and $[M]$ are zero, enabling complex conjugate pairs. The propagation matrices $[A]$ and $[B]$ are symmetric but not Hermitian due to the multiplication of an imaginary unit j in Eqs. (6.9) and (6.10).

The BPM scheme of Eq. (6.8) can be rewritten as

$$\{\phi\}\mid_{z+\triangle z} = e^{-j[Q]\triangle z}\{\phi\}\mid_z \tag{6.35}$$

with Cayley's form [256]

$$e^{-j[Q]\triangle z} = \frac{1-\frac{1}{2}j[Q]\triangle z}{1+\frac{1}{2}j[Q]\triangle z} + O(\triangle z)^3 \tag{6.36}$$

where

$$[Q] = \frac{-1}{2k_0 n_0}[\widetilde{M}]^{-1}\left([K] - k_0^2 n_0^2 [M]\right) \tag{6.37}$$

According to [257] (pp.185), $e^{j[Q]}$ is unitary only when $[Q]$ is Hermitian. An unitary propagation therefore requires $[Q]$ to be Hermitian, which is generally not the case even though $[K]$, $[M]$ and $[\widetilde{M}]$ are all Hermitian.

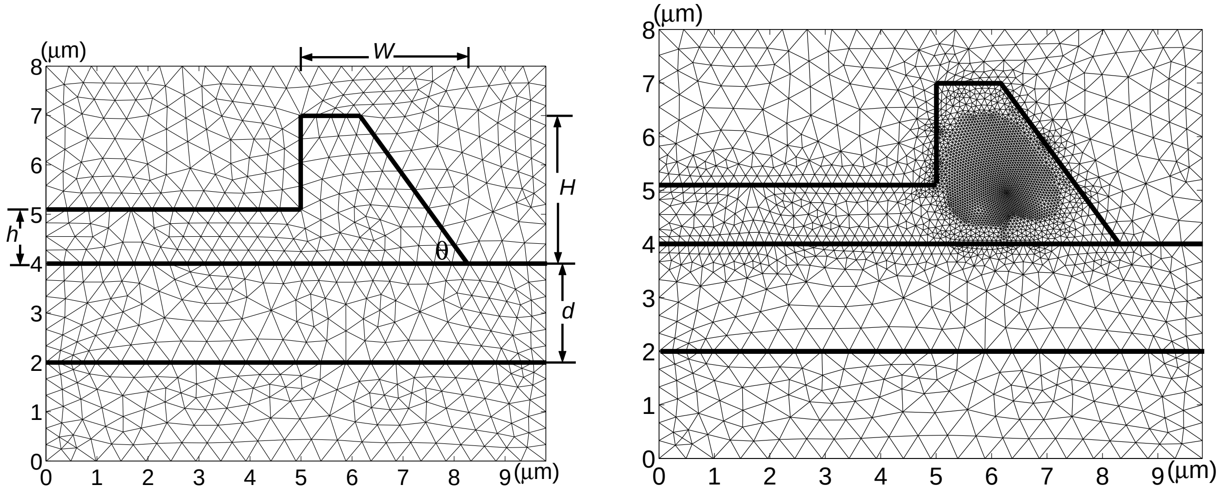

(a) (b)

Figure 6.5: Geometry and discretization of the waveguide crosssection. Finite element discretizations for the slanted-angle rib waveguide discussed in the text for: (a) a regular mesh with 1156 elements, 622 nodes and minimum triangle area $1.47 \times 10^{-2} \mu\text{m}^2$; and (b) an adaptive mesh with 6413 triangles, 3253 points and minimum triangle area $2.40 \times 10^{-4} \mu\text{m}^2$.

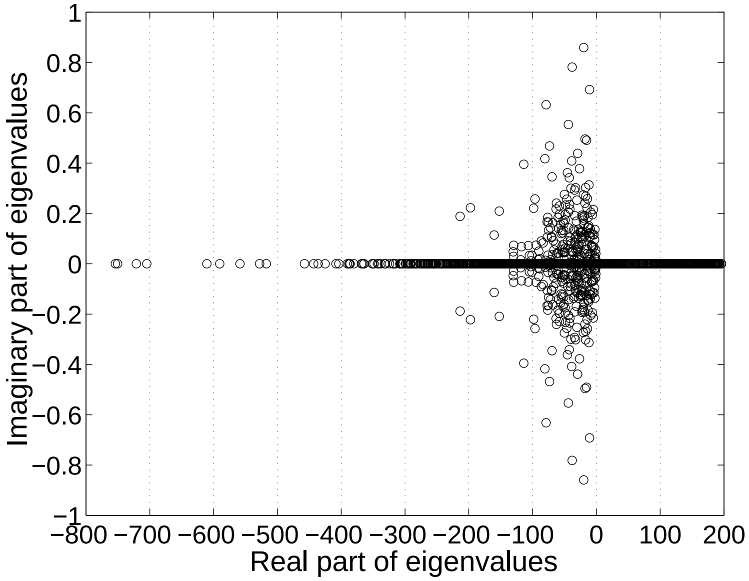

Figure 6.6: The eigenmode spectrum for the mesh of Fig. 6.5(a).

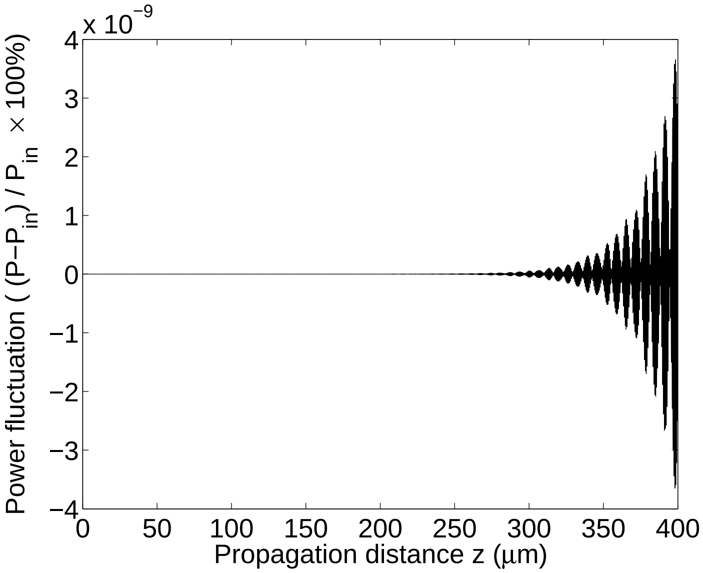

Figure 6.7: The power fluctuation for the lowest-order fundamental mode as a function of propagation distance for the mesh of Fig. 6.5(a).

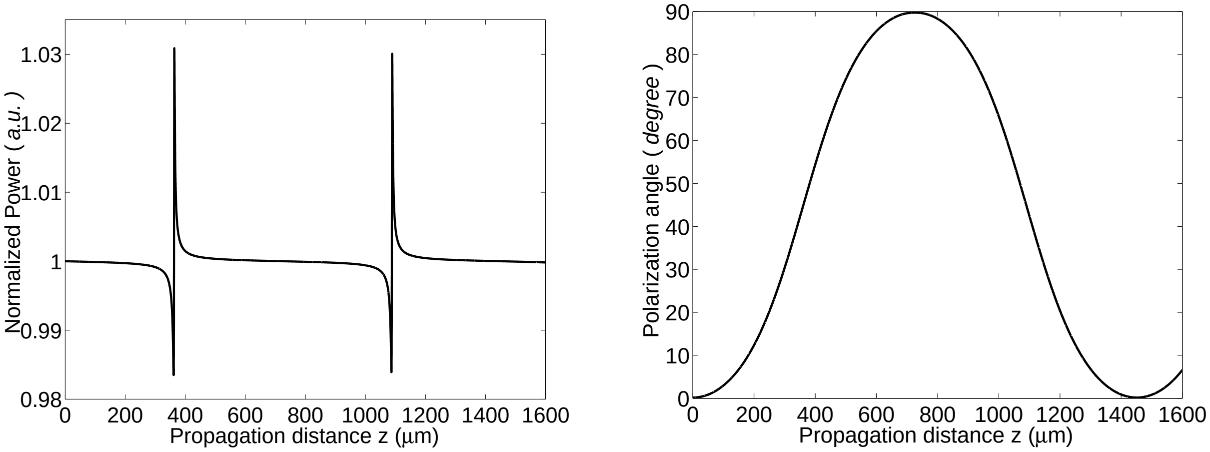

(a)

(b)

Figure 6.8: (a) The normalized power and (b) polarization exchange of the slanted angle waveguide excited by a TE polarized mode as a function of propagation distance based on Crank-Nicholson scheme and the mesh of Fig. 6.5(a).

While at least one vectorial mixed element FE-BPM has been reported to be fully energy-conserving [182] it should be noted that in the presence of complex-conjugate eigenmode pairs, the Poynting vector of the field can be preserved [58,253] although the magnetic and electric fields individually may approach infinity and zero with an accompanying large field profile error [152, 153, 250, 251]. In fact, for $[A]^{-1}[B]$ in the propagation formalisms of [182] to be Hermitian, $[A]^{-1}[B] = [B][A]^{-1}$ should be satisfied in addition to Hermitian $[A]$ and $[B]$. Furthermore, after the transformation $\phi_z = j\frac{\partial}{\partial z}\phi_z{}'$ is employed in [182], even though the Poynting vector of the modified field $\{\phi_t, \phi_z{}'\}$ is preserved, this may not be the case for the physical field $\{\phi_t, \phi_z\}$.

6.3.3 Eigenmode Spectrum and Power Fluctuation

We now illustrate the above considerations by examining the numerical instabilities associated with the high-index-contrast asymmetric SOI PR with facet angle $\theta = 54.736°$, rib height $H = 3\mu$m, rib base width $W = 3.3\mu$m, and outer-slab thickness $h = 1.1\mu$m.

We apply Dirichlet BC in the full-vectorial mixed-element $\boldsymbol{H}$-formulation FEM eigenmode solver together with the BPM procedure. Our calculations are performed both on the uniform mesh of Fig. 6.5(a) with 1156 elements, 622 nodes and minimum triangle area $1.47 \times 10^{-2}\mu\text{m}^2$; and on the adaptive mesh of Fig. 6.5(b) with 6413 triangles, 3253 points and minimum area $2.40 \times 10^{-4}\mu\text{m}^2$. This adaptive grid, generated from the uniform mesh through our dedicated MATLAB package, concentrates elements in regions with large fields and at the material interfaces.

In Fig. 6.6, we display the eigenmode spectrum of the slanted angle waveguide for the regular mesh. The propagation constant of the lowest-order fundamental eigenmode was also verified by the Crank-Nicholson imaginary distance beam propagation method (ID-BPM) [222–224] in Section 6.1.2 with a propagation step-size $\triangle z = 0.1\mu$m, establishing the consistency of the propagation and eigenvalue methods. Real eigenvalues can be solved from $\frac{([K]\{\phi\}, \{\phi\})}{([M]\{\phi\}, \{\phi\})}$ [58,110], where $(a\,,\, b)$ means the norm of vectors a and b. The subspace iteration algorithm [254] (also known as simultaneous iteration [121]) is capable of finding a set of real or complex eigenvalues around a given value. However, it is difficult to find complex modes using iteration methods since proper initial guesses for complex values are hard to produce. Fortunately, in many cases, people are only interested in finding several lowest-order guided-modes with real positive propagation constants for a waveguide [122,127] (note that in Fig. 6.6 all positive eigenvalues are real). Using advanced numerical packages such as ARPACK, or the numerous eigenvalue solves (sparse or full) in MATLAB, one is able to obtain complex eigenvalues or the whole eigenvalue spectrum as Fig. 6.6.

The numerous complex-conjugate eigenmode pairs lead as expected to divergences in real Crank-Nicholson field propagation as evident from Fig. 6.7, which shows the power in the propagating field normalized to the input power. Diverging oscillations in the power are first apparent at a 250μm propagation distance for the uniform mesh while a corresponding instability (not shown) appears at 33μm for the adaptive mesh due to the smaller grid point spacing for elements near index discontinuities.

Despite the divergences that appear at longer propagation lengths, our propagation method can still be employed to solve practical modeling problems. For example, the adaptive z-dependent complex reference index technique of [221] yields the normalized power for a TE-input field shown in Fig.6.8(a). While this result is affected by the field divergence, similar calculations for low index contrast InGaAsP slanted-angle polarization rotators remain stable. Further, the power transfer between the TE and TM modes is correctly predicted, as evidenced from Fig. 6.8(b) which displays the polarization angle θ_p obtained from the ratio of the power in the two polarization components

$$\theta_p = tan^{-1}\left(\frac{P_y}{P_x}\right) \tag{6.38}$$

While mixed finite element propagation procedures generally do not conserve power, practical calculations can still be performed for many waveguide profiles. Large discontinuous refractive index steps or small numerical grid spacings however result in rapid field divergences. Unfortunately, our results indicate that such divergences can easily occur for adaptive grids, for which the grid sizes near discontinuities typically become uncharacteristically small. While a solution similar to that of [152, 248] may exist, the required analysis would be complicated and therefore beyond the scope of this thesis.

6.4 BPM Simulation on Asymmetric SOI PR

In this section, we study the beam propagation characteristics of the slanted-angle SOI polarization rotator (PR). We consider the asymmetric external waveguiding layer SOI angled-facet waveguide with rib height $H = 2.8\mu$m, rib width $W = 2.7\mu$m and outer-slab thickness $h = 1\mu$m. We subdivide the calculation region into non-uniform unstructured mesh like in Fig. 6.5(a) with 2252 second-order mixed triangular elements (LT-QN), 4597 nodes (1173 vertexes) and 6848 tangential edges. With Neumann boundary condition, we construct 11445 × 11445 eigenvalue matrices $[K]$ and $[M]$, where nonzeros are 67,744 in $[K]$ and 201,339 in $[M]$, respectively.

The fundamental eigenmodes calculated from this mesh have refractive indices of $n_{eff1} = 3.4433225$ and $n_{eff2} = 3.4416837$, respectively, corresponding to a half-beat length of $L_\pi = 472.93\mu$m. The H_x, H_y, and H_z components of the fundamental modes in this asymmetric SOI slanted-angle waveguide are plotted in Fig. 6.9, from which we are able to generate two input fields with TE- and TM-polarizations, respectively. As displayed in Fig. 6.10, the top two field components H_x and H_y are for a Quasi-TE field, while the bottom two components are for a Quasi-TM field.

In the following BPM simulations, to avoid power fluctuation arising from the intrinsic non-unitarity discussed in Section 6.3, we adopt the quasi-Crank-Nicholson propagation scheme [129] by choosing $\alpha = 0.5+\epsilon = 0.55$ in Eqs. (6.9) and (6.10). The propagation step is chosen sufficiently small $\Delta z = 0.1\mu$m in order to minimize discretization error [197], and the complex reference index n_0 is recalculated after each step so as to increase the numerical efficiency and accuracy [197, 221]. The discretization is chosen as the regular mesh of Fig. 6.5(a) instead of the adaptive mesh of Fig. 6.5(b) since with the latter the instability related to the Crank-Nicholson scheme could appear earlier as having been discussed in Section 6.3.

Despite the large matrix dimensions (e.g., 11445 × 11445) in our full-vectorial BPM calculation, each single step of propagation takes only 6.48 seconds on a 1.3GHz IBM R6000 AIX51 computer with our sophisticated and versatile MATLAB 6.5 code.

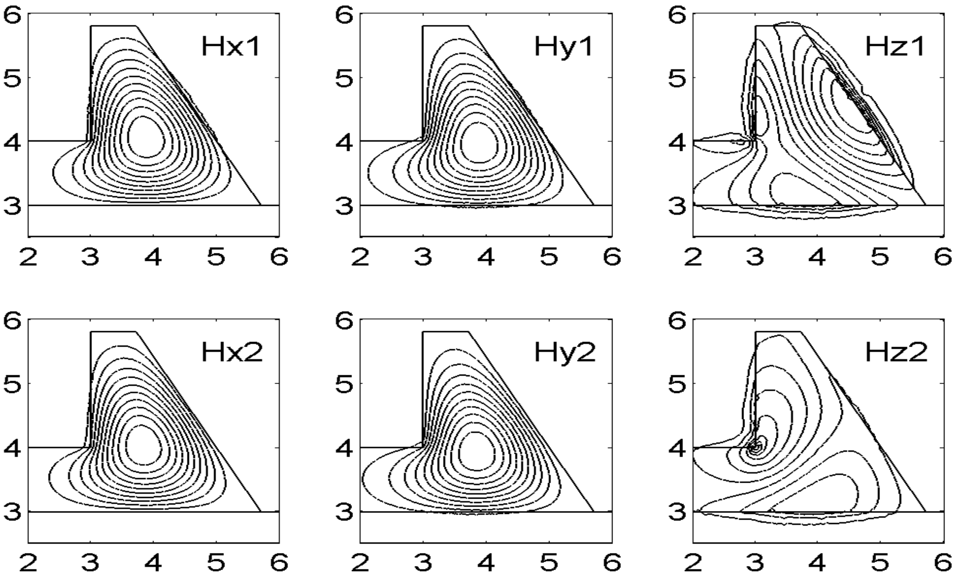

Figure 6.9: Fundamental modes of the SOI polarization rotator.

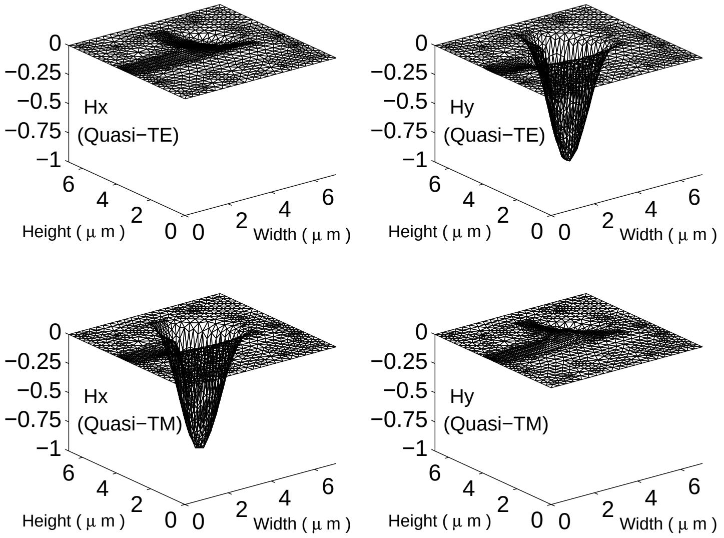

Figure 6.10: Field to launch into the SOI polarization rotator: (a) top: H_x and H_y components of a TE-polarized field; and (b) bottom: H_x and H_y of a TM-polarized field.

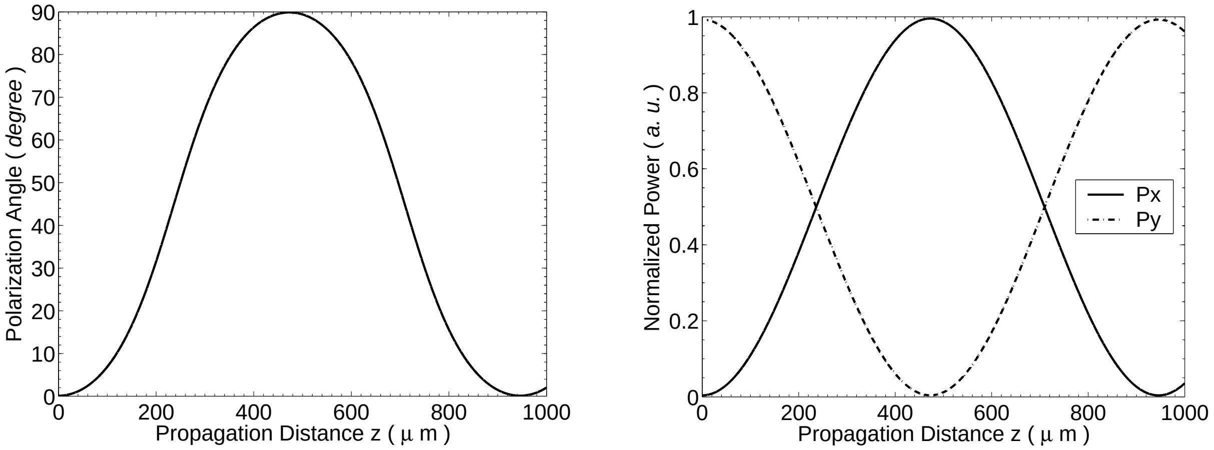

(a) (b)

Figure 6.11: BPM simulation of the polarization conversion for a Quasi-TE input: (a) variation of the polarization angle θ_p during propagation; and (b) power exchange between the transverse field components.

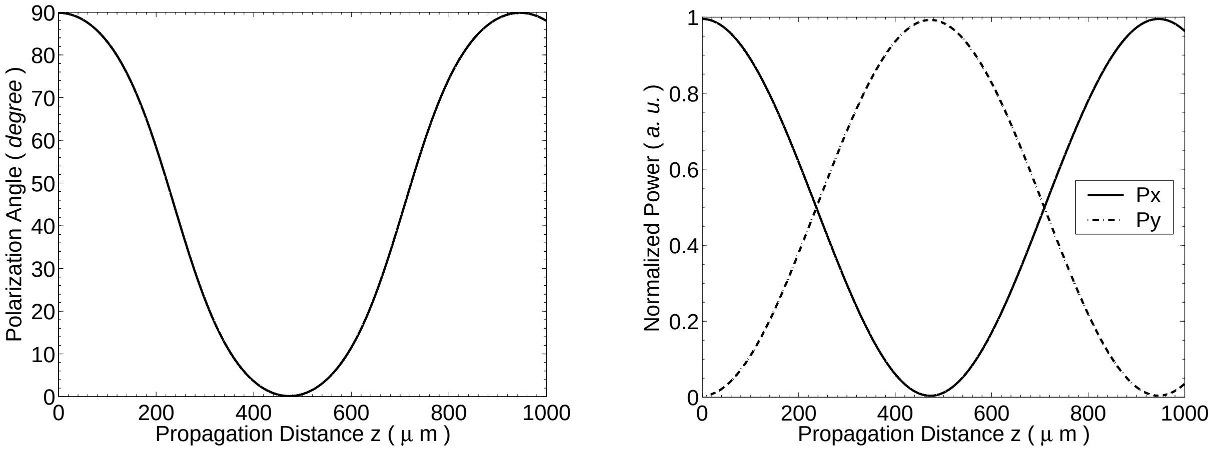

(a) (b)

Figure 6.12: BPM simulation of the polarization conversion for a Quasi-TM input: (a) variation of the polarization angle θ_p during propagation; and (b) power exchange between the transverse field components.

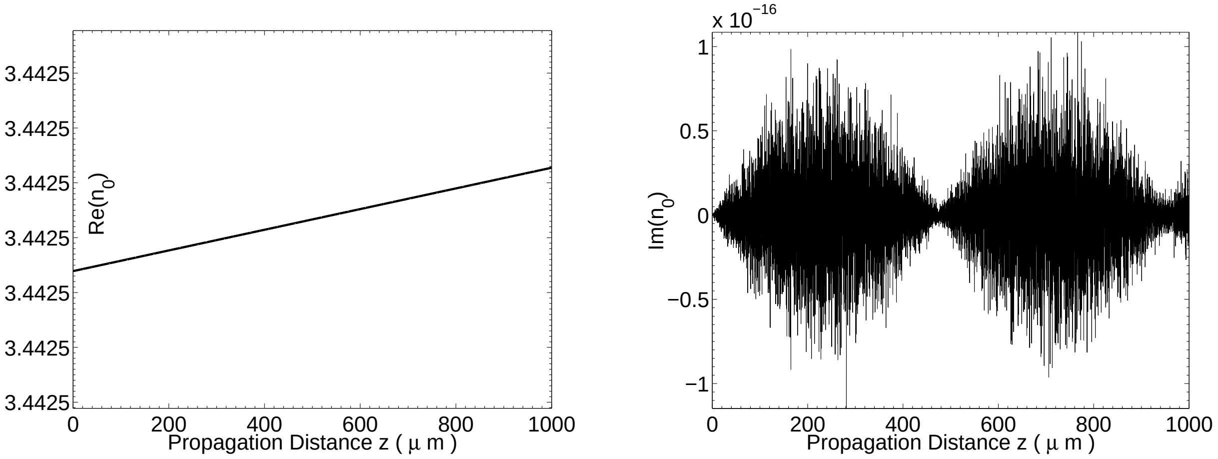

(a) (b)

Figure 6.13: Variation of the reference index n_0 with respect to the propagation distance: (a) real part of n_0; and (b) imaginary part of n_0.

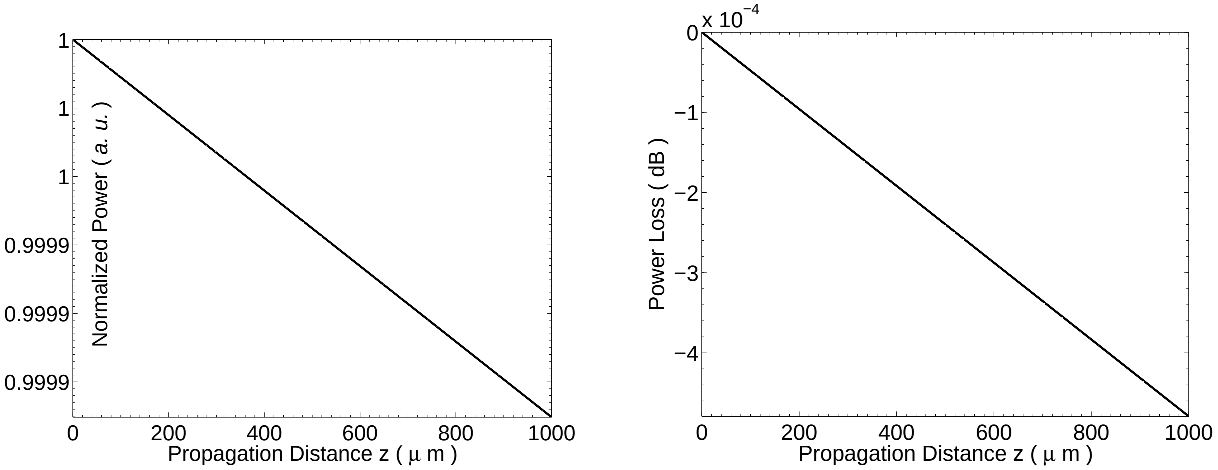

(a) (b)

Figure 6.14: Variation of (a) the normalized power and (b) the power dissipation with respect to the propagation distance.

6.4.1 Polarization Conversion and Power Exchange

We first launch the Quasi-TE field into the input port of the SOI polarization converter and propagate it for 1000μm with a step-size of 0.1μm. The polarization angle θ_p with respect to the horizontal direction (Eq. (6.38)) and the exchange of the power carried by transverse field components H_x and H_y are displayed in Fig. 6.11. We clearly observe from Fig. 6.11 that the TE-polarized input light with the dominant field H_y is first completely ($PC = 99.60\%$) converted to a TM-polarized field with a dominant field H_x after a propagation distance of 473μm, which is exactly equal to the device half-beat length obtained from the FEM eigenmode solver. The polarization rotating phenomenon continues, and after another 473μm the TM-polarized field is reconverted into a TE-polarized out. Results obtained for a Quasi-TM field launched into the input of the SOI PR are illustrated in Fig. 6.12, from which we draw the same conclusion. The polarization conversion efficiency for the TM-polarized input is $PC = 99.61\%$, with a negligible difference compared with $PC = 99.60\%$ for a TE-polarized input. In contrast, this difference is obvious in previous III-V slanted-angle polarization rotators with symmetric external waveguiding layers [40, 53] or periodically-loaded devices [15, 40]. We therefore find one more advantage of our single-section SOI PR design utilizing asymmetric outer-slab layer.

6.4.2 Numerical Dissipation and Adaptive Reference Index

In Fig. 6.13, we display the adaptation of the complex reference refractive index n_0 according to Eq. (6.11). Although most applications take only the real part [194, 219, 240, 241] of this reference index, the complex value [197, 221, 258, 259] could minimize the numerical error. The complex reference index method is an alternative to the complex Padé approximation [153] for reducing the inaccuracy and instability of BPM algorithms [258]. The real part of n_0 varies slightly from 3.44250396343899 to 3.44250396362747, which is very close to the average of the effective indices of the fundamental eigenmodes, since any TE- or TM-polarized field can be expressed in terms of certain combinations of these 45°-rotated eigenmodes. However, as shown in Fig. 6.13(b), the imaginary part of the reference index fluctuates periodically with a period equal to the beat length of the device. Though this fluctuation is fairly small, ignoring the imaginary part causes deviation from the best optimum reference value, which is chosen to minimize power fluctuation [197].

In Fig. 6.14, we show the power dissipation [162, 260–262] associated with the quasi-Crank-Nicholson scheme. Theoretically, the Crank-Nicholson algorithm with $\alpha = 0.5$ is unconditionally stable and zero power dissipating subject to unitary BPM operators [256]. Researchers have observed unstable field evolution with mixed finite elements [262] and nonphysical power loss with nodal elements [261] in full-vectorial BPM simulations; however, they did not question these phenomena for underlying intrinsic reasons, which have been studied thoroughly in Section 6.3 of this thesis. To predict the guided power in the waveguide as correctly as possible, the quasi-Crank-Nicholson scheme with α slightly larger than 0.5 is preferred. In our BPM calculations for the asymmetric SOI slanted-angle polarization converter, we accordingly set $\alpha = 0.55$. When $\Delta z = 0.1\mu$m the nonphysical power loss is only 0.00048dB/mm, as shown in Fig. 6.14(b). With this extremely small numerical dissipation, our FV-FE-BPM program is quite reliable for predicting the above-discussed power exchange and polarization conversion behaviors in SOI polarization rotators.

6.4.3 Validation of PC Formula

We now examine the variation of polarization conversion efficiency (PC) with respect to the device length of the SOI polarization converter. For a TE-polarized input light, the definition of this efficiency is given by Eq. (5.1); while for a TM-polarized input, it is defined by $PC_{\mathrm{TM}\rightarrow\mathrm{TE}} = P_{\mathrm{TE}}/(P_{\mathrm{TM}} + P_{\mathrm{TE}}) \times 100\%$. From the power of the transverse components, we are able to plot the PC variation regarding to propagation distance in Fig. 6.15. To check the accuracy of our calculations, Figs. 6.15(a) and 6.15(b) compare these BPM numerical calculations for both TE- and TM-polarized inputs with values obtained from the analytical formula of Eq. (5.2). The numerical and theoretical results agree fairly well; therefore, the simple polarization conversion efficiency formula Eq. (5.2) could play a very important role in predicting polarization exchange behavior of longitudinally-invariant polarization converters.

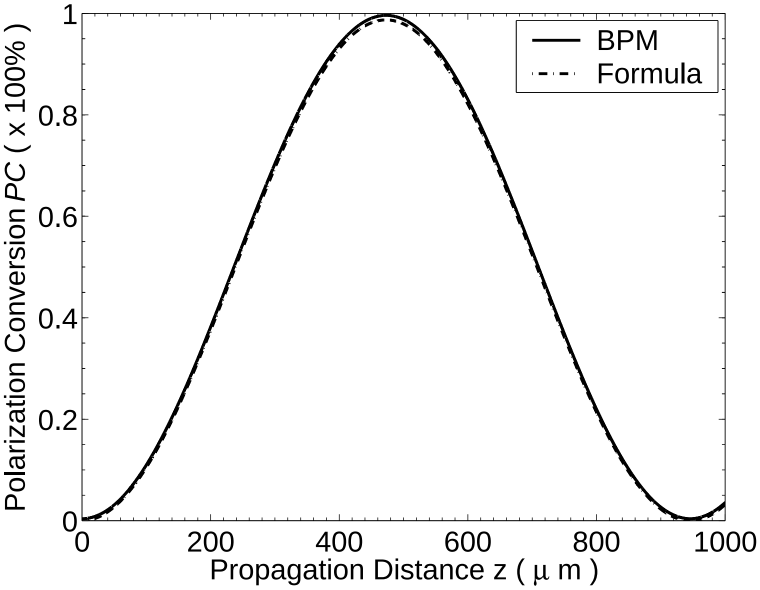

(a)

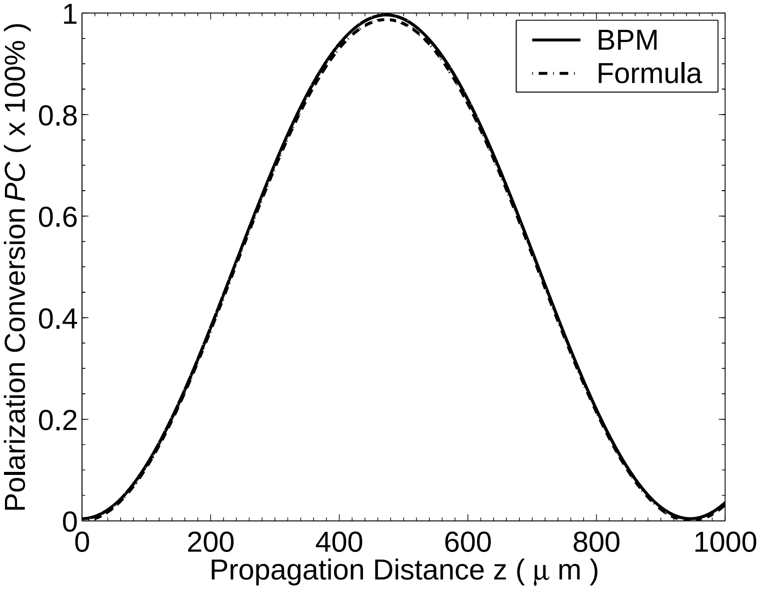

(b)

Figure 6.15: Comparison of polarization conversion efficiency (PC) obtained from BPM and analytical formula Eq. (5.2) for the SOI polarization rotator: (a) TE-polarized input; and (b) TM-polarized input.

6.5 Performance of Fabricated Devices

Having numerically studied the performance of the above 3μm SOI polarization rotator, here we turn to the actual fabricated 5μm device shown in Fig. 5.10(b) of Section 5.5. As studied in Section 5.3, an ideal design with $(H, W, h, h_r) = (4.8, 4.8, 1.8, 0)\mu$m has a rotation parameter $R = 1.01$, optical-axes rotation angle $\varphi = 45.29°$, half-beat length $L_\pi = 2572\mu$m and maximum polarization conversion efficiency $PC = 99.98\%$. However, due to unavoidable manufacturing errors, geometrical parameters of the actual fabricated device discussed in Section 5.5 are $(H, W, h, h_r) = (5.0, 4.9, 1.9, 0)\mu$m, and the sidewall angles are 89° and 56° for the vertical and slanted walls, respectively [5, 8]. As a result, the rotation parameter and optical-axes rotation angle are degraded to 1.122 and 41.72°, respectively, while the half-beat length increases to 2940μm.

In the fabrication, the photomask is divided into multiple sets, each having ten rotator sections with equally-increasing longitudinal lengths [8]. Therefore, we study the polarization conversion efficiency (PC) with respect to the device length in Fig. 6.16, where both TE → TM and TM → TE conversions are measured. The maximum conversion efficiencies are $PC_{\mathrm{TE}\rightarrow\mathrm{TM}} = 75\% \pm 3\%$ and $PC_{\mathrm{TM}\rightarrow\mathrm{TE}} = 62\% \pm 3\%$, respectively; and the excess loss is only 0.6 ± 0.1dB/mm and 0.5 ± 0.1dB/mm for TE- and TM-input, respectively. The difference between both conversions could possibly be a result of the imperfect optical-axes rotation or the vertical sidewall roughness which affects each polarization differently.

In addition, the rotator section lengths with maximum PC in the simulation and the measurement are 2940μm and 3256μm, respectively. When the optical-axes rotation angle deviates from 45°, the TE ↔ TM polarization conversion effects become weaker; therefore, the distance required to achieve maximum polarization increases while the maximum TE ↔ TM conversion efficiency reduces. The junctions formed by the butt-coupling to input/output SOI rib waveguides might also contributes to this shift.

We observe considerable difference between experimental measurements and theoretical predictions. However, this mismatch is a result of the weakened polarization conversion due to possible factors such as measurement misalignment, butt-coupling offset, end-facet cross-section roughness, longitudinal perturbation, or other reasons explained previously in Section 5.5. To illustrate, we extend the fabrication tolerance study in Chapter 5 by considering the variation of polarization conversion efficiency versus rotator lengths.

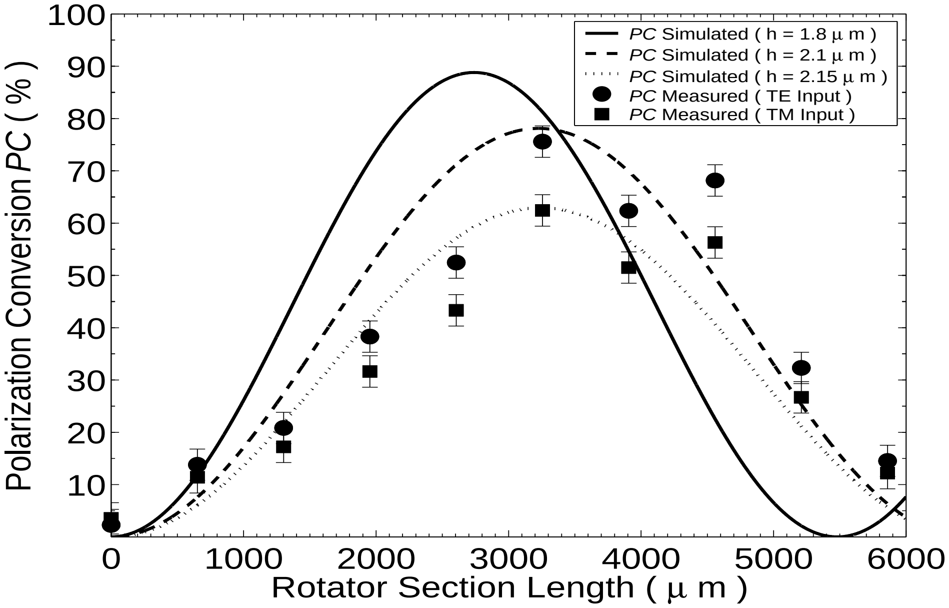

Figure 6.16: Comparison of theoretical propagation with measured polarization conversion.

We have learned from Section 5.3 that the uncertainty of outer-slab layer thickness ($\pm 0.1\mu$m) contributes most to the deviation of performance, therefore we simply consider this factor here for brevity. In Fig. 6.16, the solid, dashed, and dotted lines are for outer-slab thickness of $h = 1.8\mu$m, 2.1μm, 2.15μm, respectively, which leads to the device performances of $(R, \varphi, L_\pi, PC_{\max}) = (1.416, 35.23°, 2740\mu\text{m}, 88\%)$, $(0.602, 31.05°, 3227\mu\text{m}, 78\%)$, and $(0.493, 26.24°, 3243\mu\text{m}, 62.9\%)$, respectively. Although measured results deviate from designed ideal performance, they can be better fitted by considering the geometric uncertainty (fabrication precision $\pm 0.1\mu$m, and measurement error $\pm 0.1\mu$m for lengths and 1° for angles). Measured outer-slab thickness is $h = 1.9 \pm 0.1\mu$m in the actual fabricated device; however, simulations with very close values $h = 2.1\mu$m and 2.15μm fit these experiments fairly well. This could be well explained with the rounding of the vertical sidewall corner, which effectively increases the slab thickness. We therefore believe that the fabrication quality and measurement accuracy could be further improved significantly with nano-photonics processing technologies [200–203] or techniques suggested in [8].

6.6 Summary

In this chapter, we have developed general BPM codes for scalar, semi-vectorial, and full-vectorial analysis. To efficiently absorb outgoing fields, we employed the anisotropic PML boundary condition and examined its efficiency with on- and off-axis Gaussian beam propagations in both free space and a rib waveguide.

We also thoroughly analyzed the intrinsic non-unitarity in full-vectorial BPM algorithms with mixed-type finite elements. Though the non-unitarity could cause power fluctuation in numerical simulations, its impact can be reduced by methods such as quasi-Crank-Nicholson scheme and adaptive complex reference index. Our calculations were performed for the asymmetric SOI polarization converter without outer-slab layer at the angle-facet side. We showed excellent polarization exchange behavior of this device with both TE- and TM- polarized input fields, and also found negligible difference between these two inputs, indicating excellent optical-axis rotation of such polarization converters.

The validation of the analytical formula for polarization conversion efficiency (PC) has been checked by BPM results. Numerical and analytical results agree precisely for longitudinally-invariant polarization converters, therefore the simple PC formula could play an important role in characterizing such devices.

Finally, experimental results are compared with our theoretical prediction. Measurements display slightly weaker polarization conversion effects due to limited fabrication and measurement precisions; however, this discrepancy could be further improved with more precise processing techniques.

Chapter 7

Bending Characteristics of Slanted-Angle SOI Polarization Rotators

In this chapter, with full vectorial finite element analysis, we discuss the polarization conversion behavior of the novel asymmetric slanted-angle passive silicon-on-insulator (SOI) polarization rotator. Its loss characteristics such as the bending radiation loss and the transition loss to a straight waveguide are also studied. We compare the asymmetric bending characteristics of such a device and demonstrate that the bending- and transition-losses and polarization conversion are relatively insensitive to the radius of curvature when the sloped sidewall is at the outer bend radius.

7.1 Conformal Mapping Method

Integrated passive polarization rotators (PR) employ material anisotropy or geometric asymmetry to couple light from TE to TM polarization states. Asymmetrically-loaded periodic [15, 19] or single-section slanted-angle [1, 6, 7] passive PRs have recently attracted much attention for the simple geometry and strong conversion efficiency. An alternative way to achieve full polarization rotation while maintaining low insertion loss in a passive device is through periodically bent waveguides as has been demonstrated on InGaAsP

[21,22]. In such polarization converters constructed from bending waveguides, the insertion loss is 0.4dB for 45% polarization conversion (PC) efficiency and 2.7dB for 85% efficiency [21]. A microring resonator realization was similarly performed in [26].

Bending devices can be theoretically analyzed in either cylindrical [263,264] or Cartesian coordinates with a conformal transformation [265–267], which maps the bent waveguide onto an equivalent straight waveguide (ESW). Such ESW analyses have been carried out with finite-difference and coupled mode procedures [23–25], scalar FD-BPM [268], semi-vectorial FD-BPM [269], finite-element BPM [27,240], eigenmode expansion method [270] and WKB (Wentzel-Kramers-Brillouin) analysis [271]. The ESW method has been found to be accurate for bending radii larger than 1μm for an InGaAsP waveguide with base width 1.4μm and total thickness 0.9μm [23]. Mathematically, this method transforms the refractive index of the waveguide cross-section according to the following pattern

$$n_t(x, y) = n(x, y)(1 + \frac{x}{R_c}) \tag{7.1}$$

where R_c is the radius of bending curvature, $n(x, y)$ is the refractive index of the original straight waveguide and $n_t(x, y)$ is the modified index of the equivalent straight waveguide for the bend. Therefore, even for a symmetric waveguide, bending is mathematically equivalent to causing the asymmetry of the refractive index and therefore the birefringence.

7.2 Polarization Conversion of Bent Devices

The SOI polarization rotating waveguide that we will examine is depicted in Fig. 7.1. One side of the silicon rib guiding layer is etched completely to the insulating oxide layer along the $\langle 111 \rangle$ crystallographic plane so that the angle of the slanted-facet is 54.736° regarding to the horizontal direction. The refractive indices of Si and SiO_2 are $n_1 = 3.48$ and $n_2 = 1.45$, respectively. When the cross-section of the straight waveguide is given by rib height $H = 2.8\mu$m, rib width $W = 2.7\mu$m and outer-slab thickness $h = 1\mu$m [1], the TE and TM components of its two fundamental modes are comparable and the optical-axis, denoted by (u_r, v_r) in Fig. 7.1, is rotated by $\varphi = 46.24°$, corresponding to maximum 99.81% polarization conversion efficiency [1] so that a TE polarized input is nearly completely converted to a TM field after a half-beat length $L_\pi = \frac{\pi}{\beta_1 - \beta_2} = 490.08\mu$m.

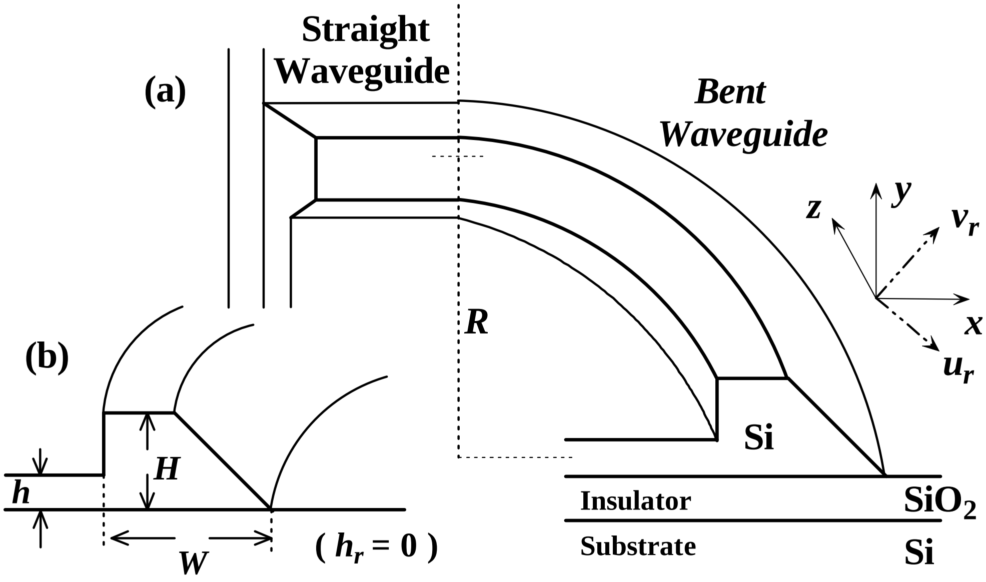

Figure 7.1: Bend orientations for the slanted-angle SOI polarization rotator: (a) slanted facet at outer bend radius; and (b) vertical facet at outer bend radius.

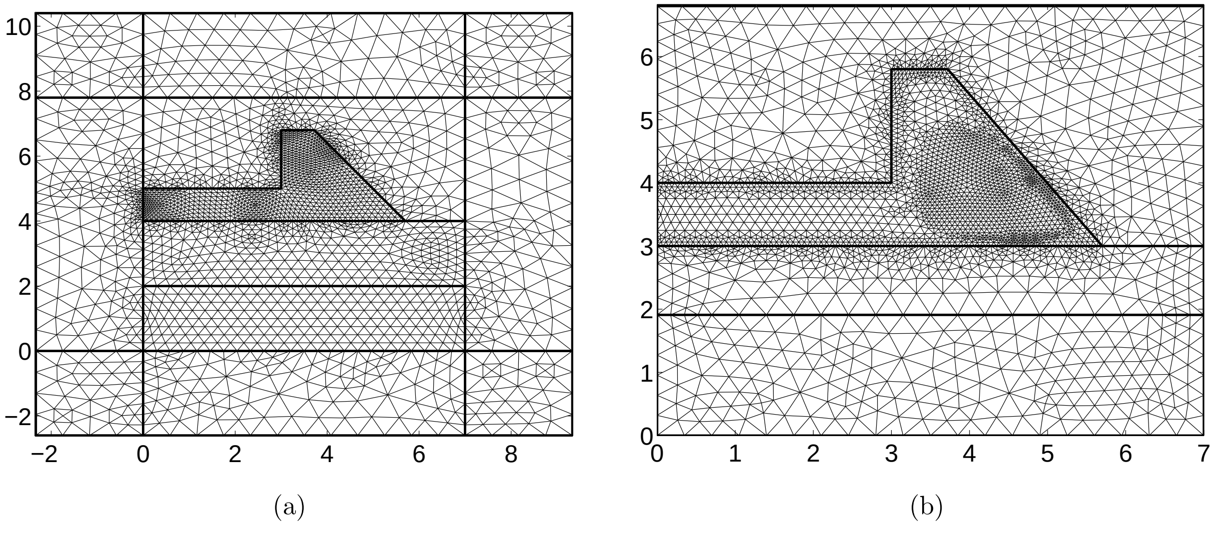

(a)

(b)

Figure 7.2: Nonuniform grid employed in the finite-element calculations: (a) for the waveguide surrounded by anisotropic PML layers; and (b) adaptive mesh according to the field distributions. (units in microns)

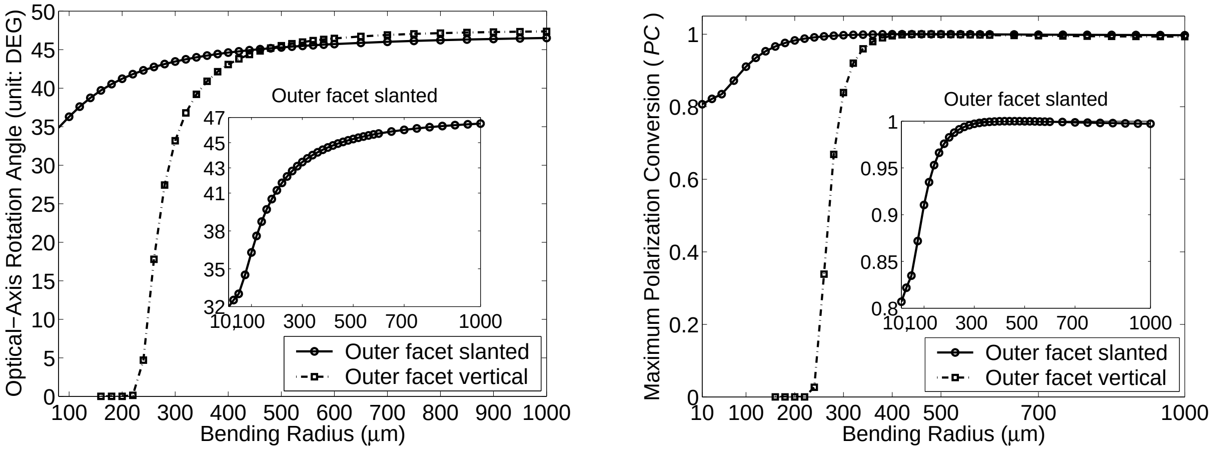

(a)

(b)

Figure 7.3: (a) The optical-axis rotation angle φ and (b) the maximum polarization conversion efficiency (PC) as a function of bending radius.

There exist two possible bend orientations as show in Fig. 7.1. In Fig. 7.1(a), the slanted-facet of the rib is located at the outer bend radius, while in Fig. 7.1(b) it is the vertical sidewall that is positioned at the outer bend radius. Obviously, because of the asymmetric waveguide geometry, the two possible bending orientations illustrated in Figs. 7.1(a) and (b) yield physically different results. Our calculations are performed on the nonuniform mesh of Fig. 7.2(a) with 4724 hybrid triangles, 2404 vertex nodes and 7127 edges, and the adaptive mesh of Fig. 7.2(b) according to the field distribution.

We first consider the effect of waveguide bending on the additional optical-axis rotation. In particular, Fig. 7.3(a) displays the optical-axis rotation angle φ as a function of bending radii. As expected, the variation of the rotation angle differs markedly depending on whether the sloped or the vertical waveguide facet forms the outer radius of the bend. In the first case, we have adjusted the rotation-angle to be exactly $\varphi = 45°$ and the half-beat length to be $L_\pi = 400\mu$m at a bending radius $R = 450\mu$m. At $R = 200\mu$m, the half-beat length is $L_\pi = 317.79\mu$m, corresponding to a 90° bend which performs almost complete TE↔TM conversion as the optical-axis rotation is $\varphi = 41.22°$ and the conversion efficiency is 98.27%. Decreasing the bending radius to 100μm still results in a maximum conversion efficiency of 91.04%, as illustrated in Fig. 7.3(b). The half-beat length variation with

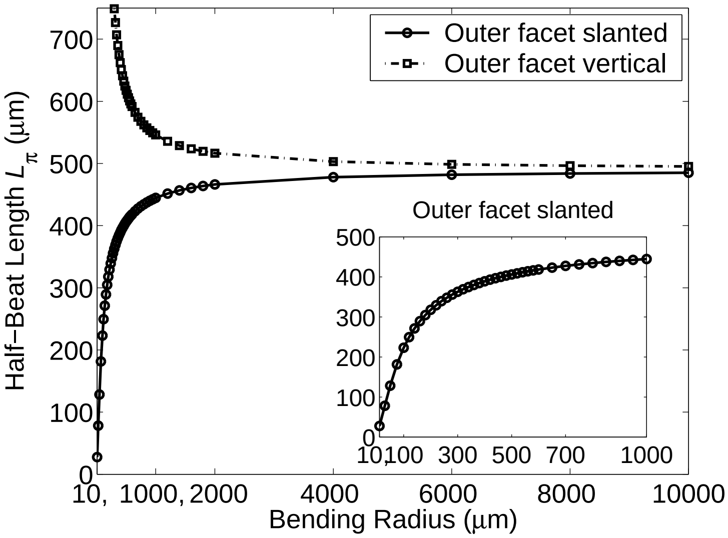

Figure 7.4: The half-beat length L_π as a function of bending radius.

respect to the radius of curvature is plotted in Fig. 7.4.

In contrast, if the vertical facet is situated at the outer radius, the optical axis rotation decreases rapidly with bending radius for $R < 400\mu$m. Exact 45° optical-axis rotation is obtained at $R = 470\mu$m for this bend orientation, however, L_π increases to 628μm. At $R = 264.76\mu$m, where the half-beat length $L_\pi = 415.88\mu$m equals to a 90° arc length, the optical-axis rotation and polarization conversion are only about 18° and 34%, respectively.

To understand the origin of this behavior, consider the magnetic field amplitudes of Fig. 7.5, which are obtained for a $R = 50\mu$m radius of curvature (the corresponding field distribution in the straight waveguide is illustrated in Figs. 4.6 and 6.9). When the slanted facet describes the outer bending radius, the field shifts toward the facet, changing the field patterns and propagation constants of both waveguide modes by nearly the same amount. Hence, the bent waveguide still functions as a single-section polarization converter. However, if the vertical facet is located at the outer bending radius, the electromagnetic field instead radiates into the outer-slab layer. As shown at the right side of Fig. 7.5, for $R = 50\mu$m bending radius the first lowest order mode is a radiating Quasi-TE-like mode for which H_x is the non-dominant component. Accordingly, at small bending radii, acceptable polarization conversion is achieved only when the sloped sidewall is the outer facet.

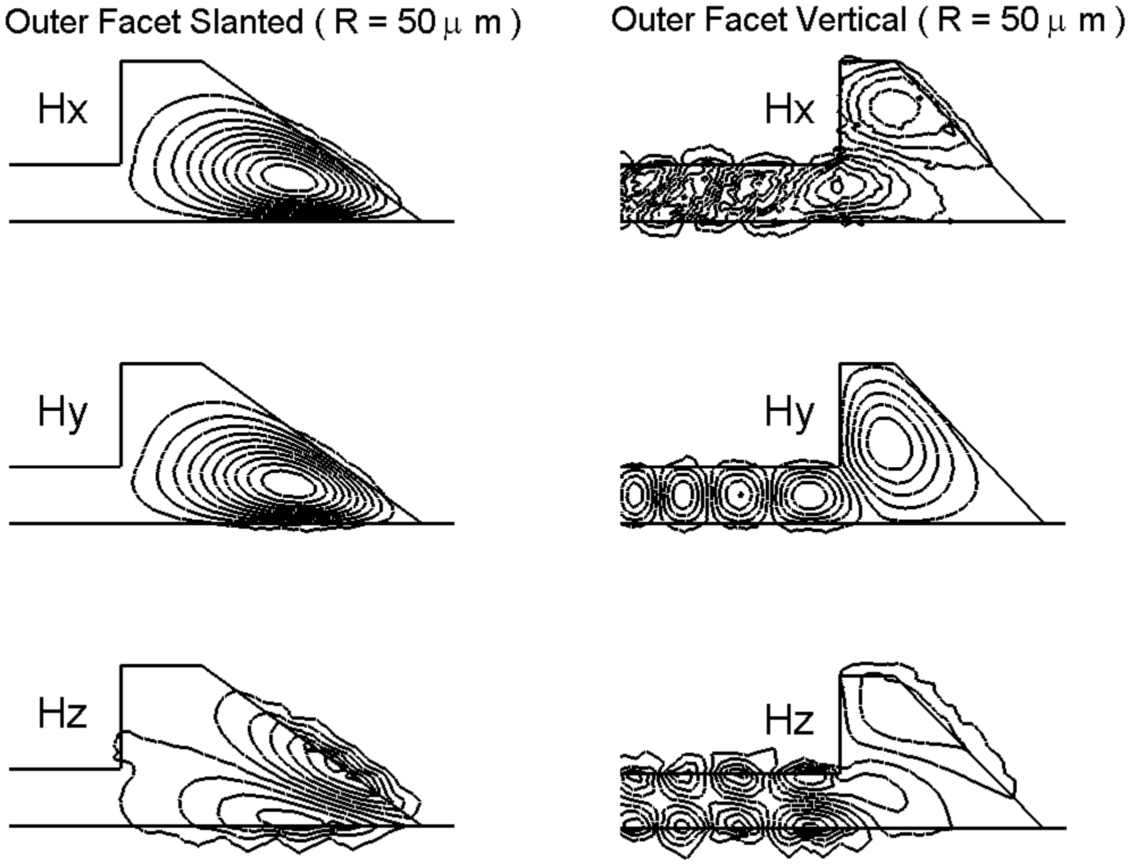

Figure 7.5: The magnetic field distribution of the first lowest-order mode in a bent slanted-angle SOI waveguide with a $R = 50\mu$m radius of curvature. In the three diagrams on the left the slanted facet constitutes the outer radius of the bend as Fig. 7.1(a), while in the right diagrams the vertical facet is instead the outer radius as illustrated in Fig. 7.1(b).

7.3 Bending Waveguide Losses

As shown in Figs. 7.5 and 7.6, bending will cause radiation loss when the vertical sidewall is positioned at the outer bend radius, since the field tends to be coupled into the outer waveguiding slab layer. However, Fig. 7.6 indicates that the pure bending loss is negligible when the slanted facet is at the outer bend radius, since the field is displaced toward the slanted wall without generating radiation modes as obvious from the left side of Fig. 7.5. The bending loss is calculated from the imaginary part of the propagation constant [22, 263, 264, 271],

$$L_b = 20\log_{10}\left[\exp(k_0 \mathrm{Im}(n_{eff}) \times 10^4)\right] \ \text{(dB/cm)} \tag{7.2}$$

where $k_0 = \dfrac{2\pi}{\lambda}$ is the wave number, λ is the wavelength in microns, n_{eff} is the effective index, and $\mathrm{Im}(\cdot)$ means taking the imaginary part.

If the bent waveguide is butt-coupled with input and output straight waveguides as Fig. 7.1, there exists transition loss due to the mismatch of the fields. The transition loss is evaluated from the overlap of the these fields according to [22, 208, 269, 271]:

$$L_T = 10\log_{10}\left[\frac{\left|\iint\limits_{\Omega} \phi_s(x,y)\phi_b^*(x,y)\mathrm{d}x\mathrm{d}y\right|^2}{\left|\iint\limits_{\Omega} \phi_s(x,y)\phi_s^*(x,y)\mathrm{d}x\mathrm{d}y\right| \cdot \left|\iint\limits_{\Omega} \phi_b(x,y)\phi_b^*(x,y)\mathrm{d}x\mathrm{d}y\right|}\right] \ \text{(dB)} \tag{7.3}$$

where ϕ_s and ϕ_b denote the field distributions of the straight and bent waveguides, respectively. In Fig. 7.7, we show the transition loss for the asymmetric slanted-angle SOI polarization rotator as a function of bending radius. Evidently, the transition loss increases rapidly if the vertical facet is located at the outer bending radius for $R < 260\mu$m, although in this case we are evaluating the overlap of the input field with the radiation field which generates a somewhat spurious result. However, the transition loss remains less than 1dB for bending radii $R > 100\mu$m if the waveguide is bent to the opposite direction. The transition loss for a 90° bend with $R = 200\mu$m and $L_\pi = 317.79\mu$m is only 0.24dB. Therefore, the asymmetric SOI PR design exhibits both low radiation loss and transition loss when the slanted-facet is situated at the outer bend radius.

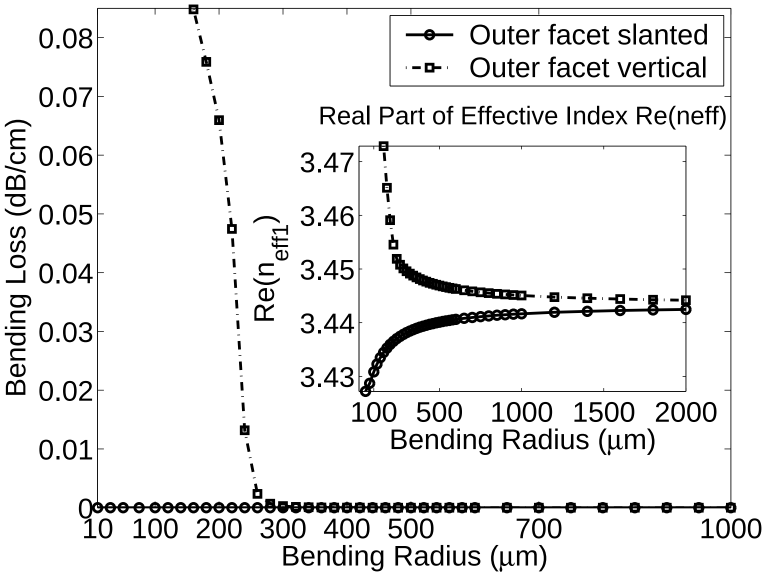

Figure 7.6: The bending loss as a function of bending radius. The inset shows the variation of the real part of the effective index of the lowest-order fundamental mode.

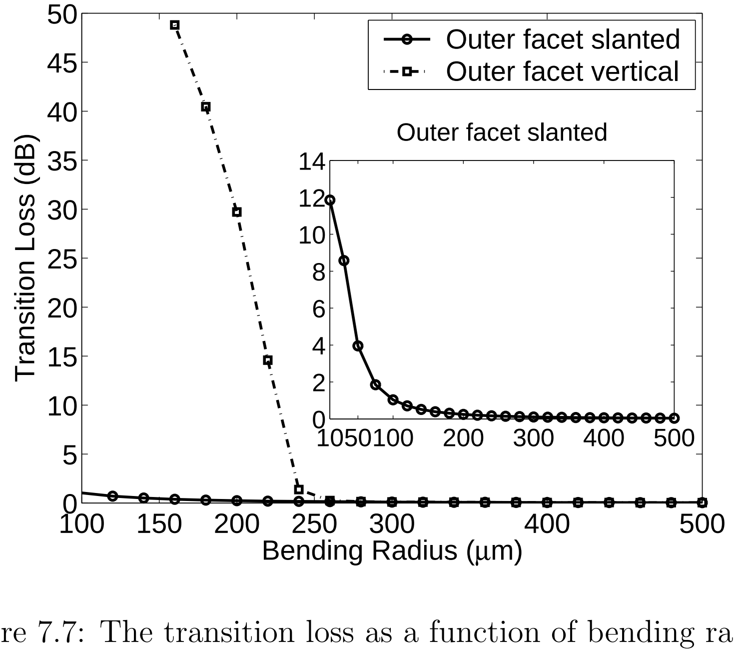

Figure 7.7: The transition loss as a function of bending radius.

7.4 Summary

We have found that asymmetric SOI slanted-angle waveguides could possess a high degree of insensitivity to bending loss while maintaining a large coupling coefficient to external waveguides and fibers. Consequently, such waveguides are important if both the direction of light propagation and the polarization are to be altered. A bending polarization rotator can function as a combination of a half-wave plate and a mirror, and its asymmetrical bending characteristics could also be utilized for some special applications such as sensors. In addition, the slanted-angle SOI polarization rotators possess very small bending radius and low bending loss, which enable ultra-compact devices for photonic integrated circuits PIC. Unlike the half-wave plate [272] which introduces large insertion loss due to significant mode mismatch, such waveguides can be well designed with negligible extra loss and are therefore quite suitable to substitute the half-wave plate used in polarization-insensitive arrayed-waveguide gratings (AWG) [272]. Fabrication problems associated with maintaining a constant slanted facet angle along a curved waveguide [22, 273–275] are clearly significant; however, our general design rules [1, 6] work for arbitrary slanted-angle which relaxes the restrictions on fabrication requirements.

Chapter 8

Loss and Coupling Analysis

This chapter briefly analyzes the coupling and loss issues associated with the asymmetric slanted-angle SOI polarization rotator. Section 8.1 discusses the insertion losses when the device is butt-coupled to single-mode fibers or rib waveguides of equivalent dimensions. Section 8.2 studies the coupling between adjacent channels when multiple devices are aligned as a parallel array. Section 8.3 presents a simple short SOI taped mode-size converter for enhancing the coupling efficiency to butt-coupled single-mode fibers (SMF).

8.1 Loss of Butt-Coupled Output

Large cross-section SOI polarization converters display reduced loss as a result of both the small measured fiber-coupling losses, e.g., 0.17dB per facet [94], and the small material losses, which were found to be below 0.5dB/cm [95] and 0.1dB/cm [94] for large cross-section waveguides. The low coupling losses reflect both the high degree of field confinement to the guiding layer as in Fig. 4.6 and the large single-mode waveguides cross-sections that properly match the mode-diameters of standard single-mode fibers [66, 90, 94, 95, 98, 99].

Our SOI polarization rotator designs display low insertion loss. For example, taking into account only the calculated modal field overlaps [22, 208, 269, 271], the coupling between our asymmetric external layer SOI polarization converter with $h_r = 0$ and a Corning® SMF-28® fiber with core diameter of 8.3μm, and core and cladding indices of 1.5362 and 1.5306 is 0.5dB for $(H, h, W) = (15, 5, 13)\mu$m, 2dB for $(H, h, W) = (10, 3, 8.5)\mu$m, 5.7dB

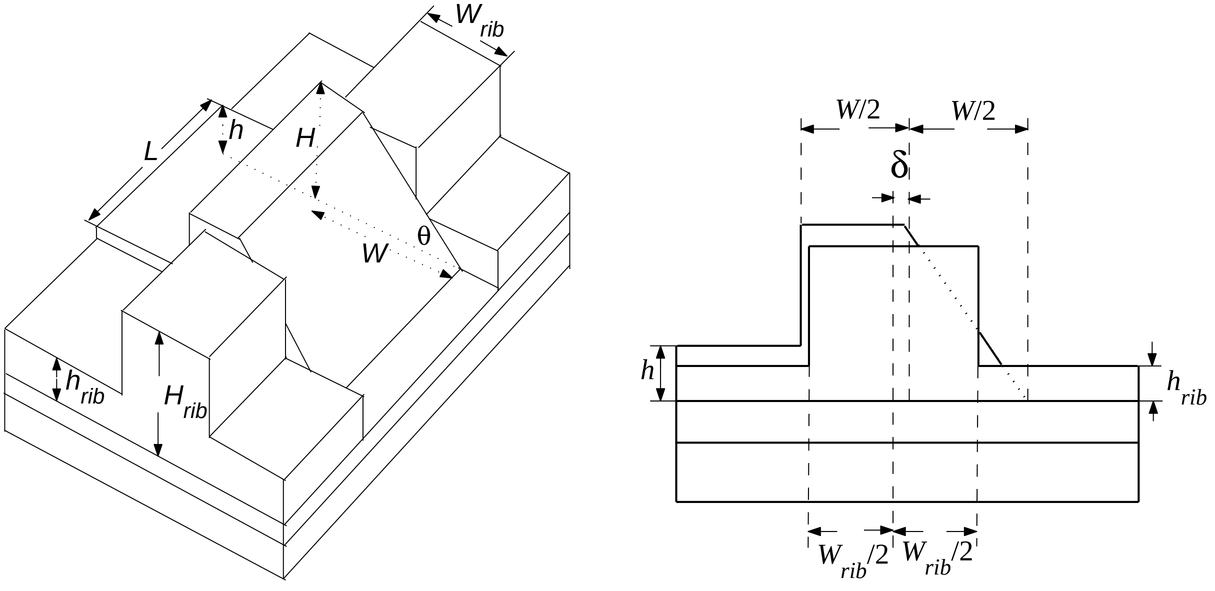

(a) (b)

Figure 8.1: Polarization rotator butt-coupled with input and output waveguides: (a). three-dimensional view; and (b). two-dimensional view.

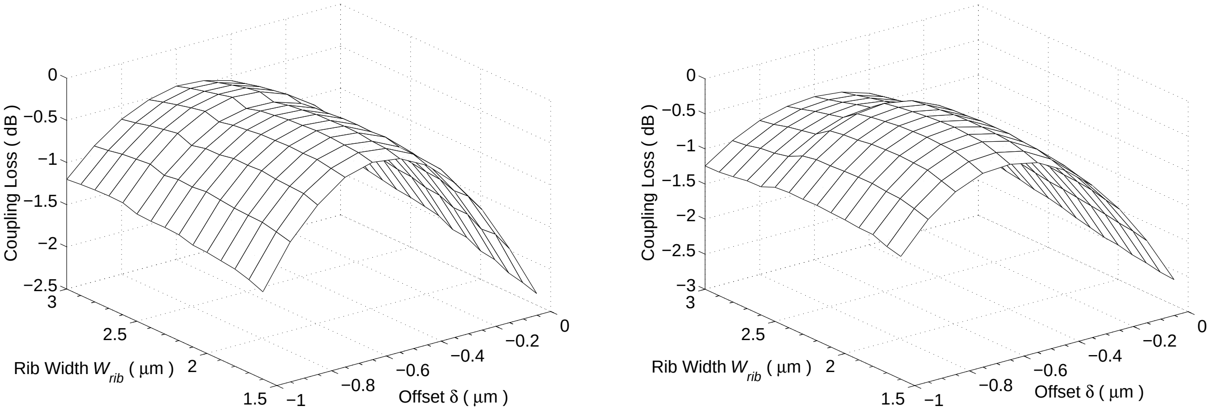

(a) (b)

Figure 8.2: Coupling loss of the butt-coupled SOI polarization converter: (a). TE-polarized input; and (b). TM-polarized input.

for $(H, h, W) = (5, 1.8, 4.8)\mu$m, and 8.7dB for $(H, h, W) = (3, 1.1, 3.3)\mu$m. This compares with our calculated value of 7dB for the III-V component discussed in [49] and [41]. If the converter is instead coupled to a tapered and lensed fiber which yields, for example, a spot diameter of 2.5μm, the polarization rotator with the most closely matched field size (here the 3μm design) will instead yield lowest loss, in this case < 2dB.

In many applications, the converter is butt-coupled [41, 43, 49, 50, 53] to rib waveguides (Fig. 8.1(a)) rather than directly coupled to the single-mode fiber. The input/output (I/O) rib waveguide, with a rib height H_{rib}, rib width W_{rib} and outer-slab layer thickness h_{rib}, is positioned with a horizontal offset δ with respect to the slanted-angle polarization converter, as illustrated in Fig. 8.1(b). The reason we consider a lateral shift between the I/O waveguides and the polarization rotating waveguide (PRW) is that the eigenmode profiles in these waveguides are different. To study the effect of this lateral offset on the coupling efficiency between the I/O waveguides and the PRW, we take the 3μm design as an example. That is, the parameters for the polarization rotator are given by $(H, W, h, h_r) = (3, 3.3, 1.1, 0)\mu$m. We consider the case when both the I/O waveguides and the angled-facet polarization converter have the same vertical dimensions, i.e., $H_{rib} = H$ and $h_{rib} = h$, which is of practical significance and is easiest to fabricate.

We vary the I/O rib width W_{rib} from 1.6μm to 3μm and the lateral shift δ from -1μm to 0. The coupling losses obtained for both TE- and TM-polarized inputs are displayed in Fig. 8.2. The minimum loss, -0.2114dB for TE-input and -0.1939dB for TM-input, is obtained for a rib width $W_{rib} = 2\mu$m and a lateral offset of $\delta = -0.6\mu$m. As obvious from Fig. 8.2, $\delta = -0.6\mu$m always corresponds to the minimum insertion loss for a specific I/O rib width.

If the vertical walls of the SOI rib waveguide and the slanted-angle SOI polarization converter coincide, we obtain a minimum coupling loss of 0.2dB for both polarizations in the 3μm design. This is achieved for a SOI rib waveguide with rib height $H_{rib} = 3\mu$m, slab thickness $h_{rib} = 1.1\mu$m, and rib width $W_{rib} = 2\mu$m. As a comparison, the total insertion loss for a III-V converter is 0.5dB [49] or 0.6dB [50] in the same configuration. If we increase W_{rib} to 3μm, the losses are 0.45dB for an incoming TE mode and 0.68dB for a TM mode.

8.2 Coupling of Parallel Configuration

In Dense Wavelength Division Multiplexing (DWDM) communication systems multiple channels exist, which may require the fabrication of an array of identical channel waveguides. In the asymmetrical-outer-slab configuration for slanted-angle polarization converters, the external waveguiding layers at the vertical and slanted sidewalls are of different thickness. If the vertical wall of one polarization converter faces the angled facet of its neighbor as shown in Fig. 8.3(a), there has to be a trench (either air or other dielectric material) between adjacent waveguides. Ideally, this configuration has negligible power coupling between neighboring channels since each waveguide is isolated separately; however, this trench imposes some extra fabrication difficulty. An alternative for parallel alignment is illustrated in Fig. 8.3(b), where the vertical walls are placed face to face. However, the outer-slab layers at the side of vertical walls are now connected, which introduces coupling between adjacent polarization rotators, e.g., B and C. This coupling occurs because the tail of the optical beam in one waveguide continually carries a small amount of power into the opposite waveguide through the jointed outer-slab layer, and after sufficiently long distance (named coupling length L_c) the power in one channel will be completely transferred into its neighboring channel.

To study this behavior, we plot the coupling length versus the waveguide separation of this configuration in Fig. 8.4. In this example, the vertical walls of adjacent waveguides are facing each other, and the waveguide separation is defined as the distance between the centers of rib bases. The geometric parameters of the asymmetric slanted-angle SOI polarization converter are rib height $H = 2.8\mu$m, rib width $W = 2.7\mu$m and outer-slab thickness $h = 1\mu$m, same as the one previously studied in Chapter 7. Fig. 8.4 shows that coupling between adjacent channels is very weak since the coupling length L_c dramatically increases to centimeters once the separation is over merely 4μm. This is a direct result of the extremely strong optical confinement in SOI waveguides, as clearly illustrated in Figs. 4.6 and 6.9. Therefore, our SOI polarization converters could be placed very closely to each other, enabling extremely compact and large-scale photonic integrated circuits (PIC).

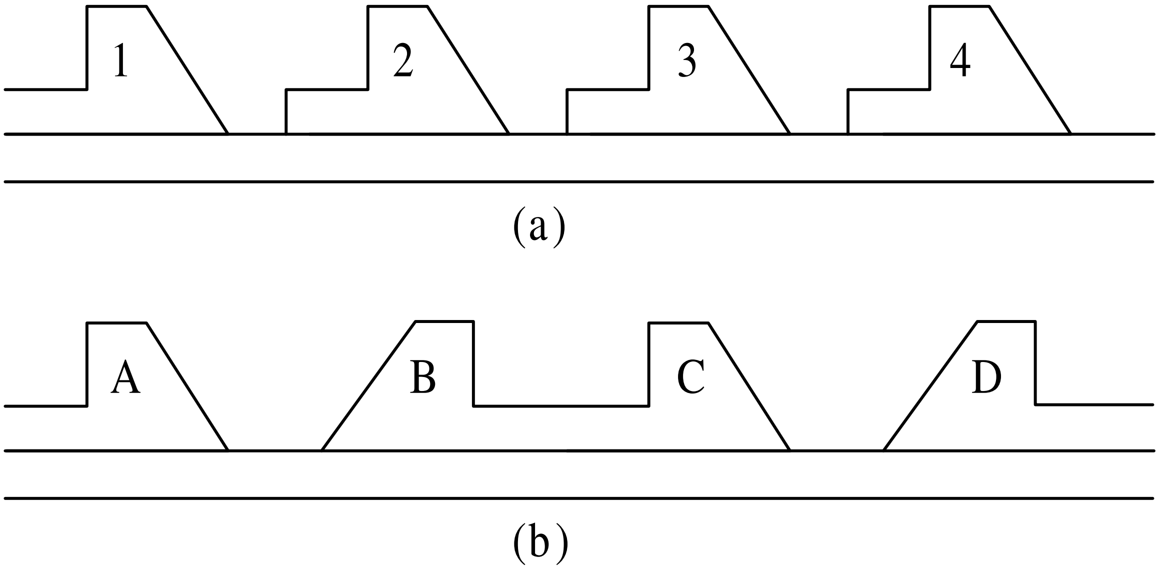

Figure 8.3: Parallel alignment of polarization converter arrays.

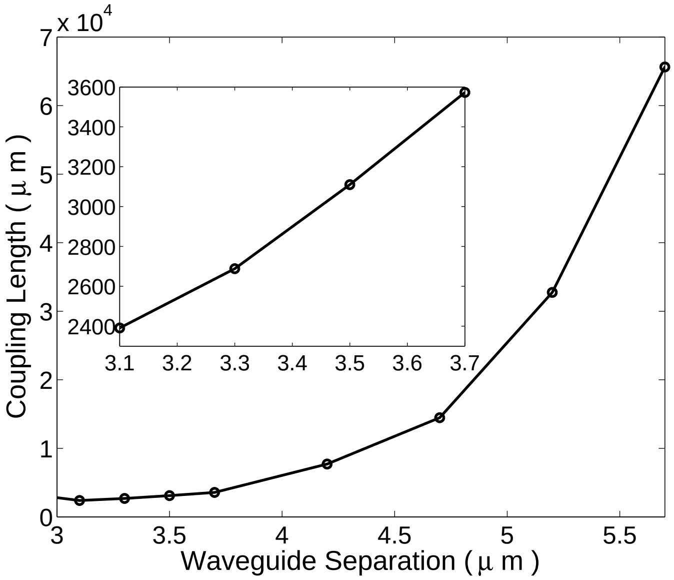

Figure 8.4: Coupling length of two parallel slanted-angle SOI polarization converters when vertical walls are facing each other.

8.3 Loss of Tapered Output

Commercial single-mode fibers (SMF) generally have a core around $8 \sim 10\mu$m, while the beam spot size from the channel waveguides of a dense integrated photonic circuit is usually submicron or a few micron meters. In addition, modal fields in integrated semiconductor waveguides can be of arbitrarily asymmetric shape rather than the circularly profile in a fiber. The distinctive difference between the modal fields, i.e., the mode mismatch, leads to poor coupling efficiency and therefore large power loss when light is launched from the SMF to integrated waveguides or vice versa. The micro-lenses or tapered/lensed fibers can be employed to improve the coupling efficiency by converting the size of the optical mode. However, they do not transform modal shapes, and packaging costs for these parts can be as high as 90% of the total device cost. Therefore, to improve both the coupling efficiency and the alignment tolerance, tapers [207, 211, 212, 217], or spot-size converters (SSC) [161, 162, 208, 209, 213, 214], or optical-mode transformers (OMT) [215], or integrated optical modeshape adapters (IOMA) [216], have been widely employed in integrated photonics.

Existing tapers can have slowly varying dimensions in either the horizontal, vertical, or both directions; consequently, they can be classified into lateral tapers, vertical tapers, combined tapers, and some special tapers [208, 209, 211]. Among these, the lateral tapers are the simplest to fabricate with standard photolithography subsequently etched by wet and dry etching processes such as the reactive ion etching (RIE) or the reactive ion beam etching (RIBE) [211]. The vertical tapers, however, can be fabricated with technologies [209, 211, 215, 216] such as dip-etch process, shallow mask techniques, or epitaxial growth techniques.

In this section, we propose a simple vertical taper design for efficiently coupling light between the asymmetrical slanted-angle SOI polarization rotators and rib waveguides or single-mode fibers (SMF). The geometry of the proposed SOI taper is plotted in Fig. 8.5, where the most notable characteristics is that each cross-section has same normalized geometric parameters, i.e., $r = h/H$ and $s = W/H$ are kept invariant. By choosing $r = 0.7$ and $s = 1$, the single-mode condition given by Eq. (2.4) is always satisfied for each cross-section, therefore power coupling between the fundamental and higher-order modes is avoided.

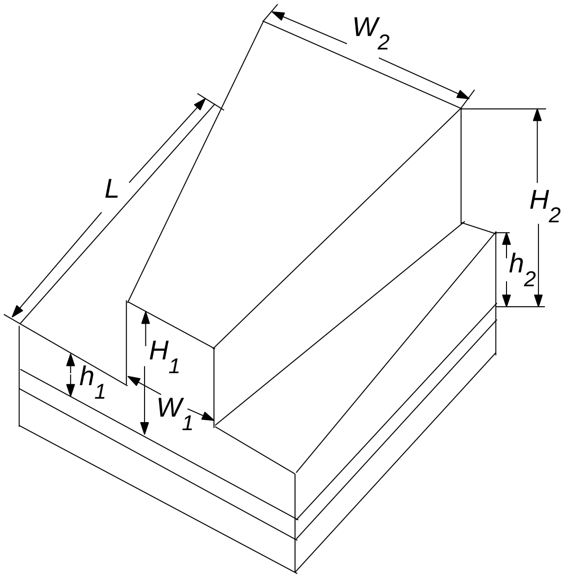

Figure 8.5: Geometry of the vertical SOI taper.

Fig. 8.6 shows the field propagation when the fundamental eigenmode of a SOI rib waveguide with $H = 5\mu$m, $W = 5\mu$m and $h = 3.5\mu$m is launched into this vertical SOI taper. The slope of the z-direction, i.e., $\frac{H_2 - H_1}{L}$, is chosen as $\frac{1}{50}$ in Fig. 8.6(a) and $\frac{1}{12.5}$ in Fig. 8.6(b). The field pattern at each cross-section of the taper looks like the local normal mode. As a fact of the extremely high index-contrast SOI material, the field is well confined in the silicon guiding region (refractive index $n_{\mathrm{Si}} = 3.48$). Consequently, the effective index of the field is far above the refractive index of the air ($n_{\mathrm{air}} = 1$), the buried silicon oxide ($n_{\mathrm{SiO_2}} = 1.45$), and the PML layer ($\Re(n_{\mathrm{PML}}) = 1$). In addition, the rib height of the smaller port is as large as 3μm in this taper example. Therefore, in both Fig. 8.6(a) and Fig. 8.6(b), we did not observe the expansion of the mode field diameter during the propagation, although such a field expansion phenomenon is commonly encountered in low index-contrast III-V tapers.

Fig. 8.7 displays calculated power loss of the monomode vertical SOI taper for various slopes along the longitudinal z-direction. When the gradient is as small as $\frac{1}{100}$, the loss of the taper is only 1.8×10^{-3}dB/mm for the field propagating from the smaller port ($H_1 = 3\mu$m) to the larger port ($H_2 = 5\mu$m), and 2.43×10^{-3}dB/mm vice versa. The losses for longitudinal slopes of $\frac{1}{50}$, $\frac{1}{25}$ and $\frac{1}{12.5}$ are 9.6×10^{-3}dB/mm, 5.32×10^{-2}dB/mm and 0.28dB/mm, respectively.

To tell the modal mismatch, Fig. 8.8 illustrates the overlap integral between the initial input eigenmode and the field at each cross-section of the taper. If two SOI rib waveguides with heights $H_1 = 3\mu$m and $H_2 = 5\mu$m are butt-coupled together, due to the obvious modal mismatch, the coupling loss is near 3dB, which means 50% power loss. However, these two waveguides can be connected smoothly by the taper structure of Fig. 8.5 with only 0.01dB insertion loss for a slope as large as $\frac{1}{12.5}$. Therefore the power transfer is dramatically enhanced.

The above analysis is limited to a linearly varying profile, improved profiles such as exponential or Gaussian shape [210] can further decrease taper length without introducing much extra loss. However, since the linear taper connecting 3μm and 5μm SOI polarization converters displays extremely low loss and can be as short as 25μm (which compares favorably with 80μm or 110μm in an InP taper [209] that changes cross-section dimensions by 2μm), we did not work further on other complicated profiles as they go beyond the focus of this thesis and can be studied elsewhere.

Moreover, in Figs. 8.7 and 8.8 there are small bumps in the curves for long tapers. These could come from the different meshes used for each cross-section, or from errors accumulated from the stair-case assumption along the longitudinal direction. The former could be solved with improved adaptive remeshing techniques since the adaptive refinement methods employed here simply add points to the mesh; and to guarantee calculation speed the maximum limit of total element number may lead to very different meshes for neighboring cross-sections. The latter could be improved with modified BPM algorithms incorporating the continuous condition in the longitudinal direction and higher-order Padé approximations. Although tapered-BPM [217] and structure-related BPM [156, 163, 276] have been proposed for FDM techniques, these have not been considered in FE-BPM so far, which can be a good future research topic.

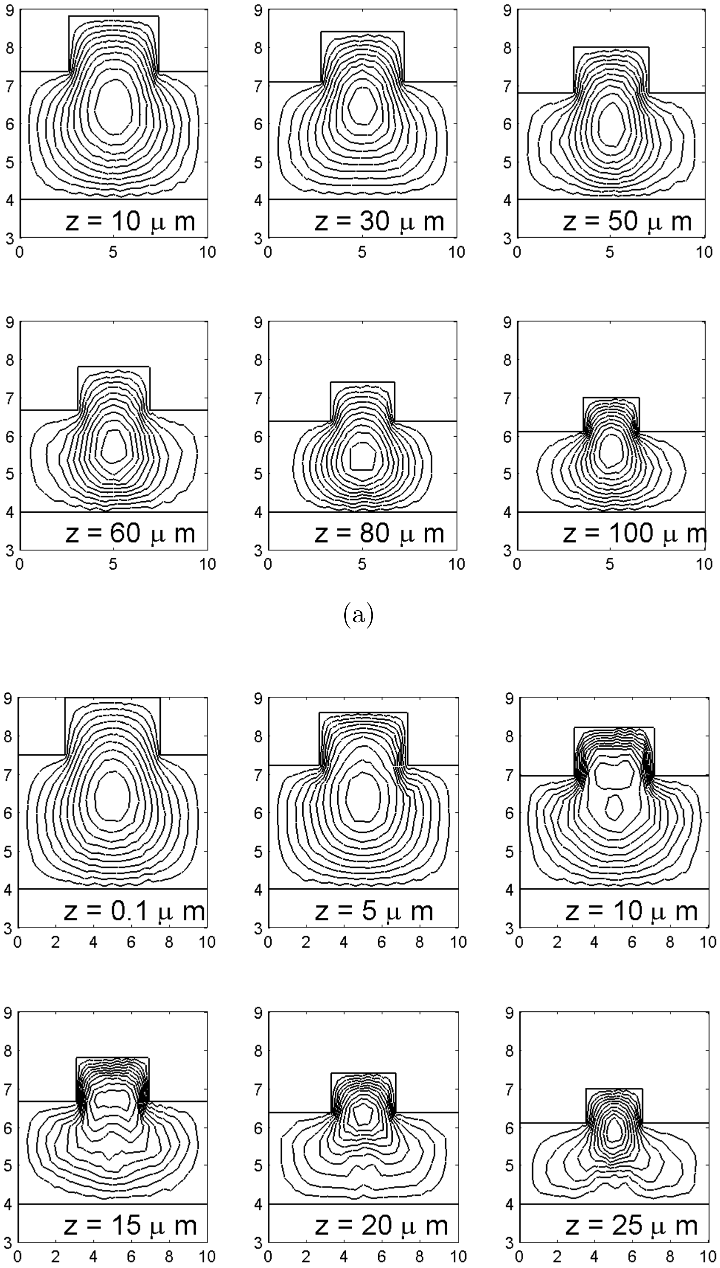

(a)

(b)

Figure 8.6: Field propagation in the SOI taper: (a) slope $= \frac{1}{50}$; and (b) slope $= \frac{1}{12.5}$.

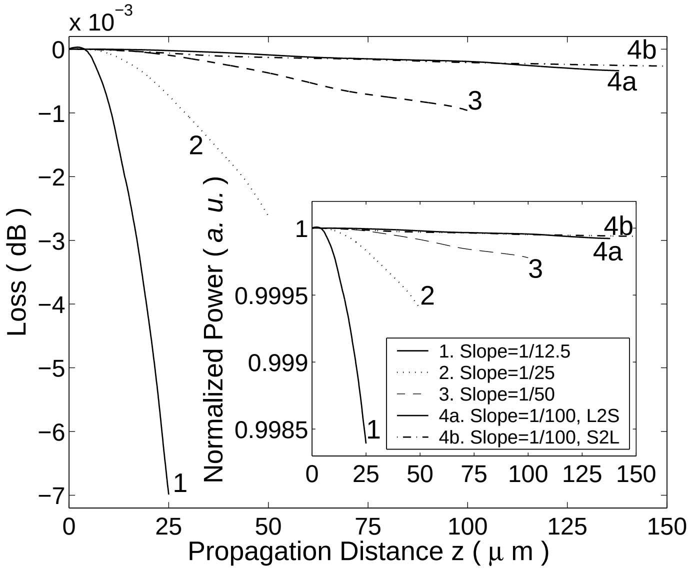

Figure 8.7: Loss of the SOI taper. The inset shows the value of the normalized power. L2S and S2L denote "from large to small port" and "from small to large port", respectively.

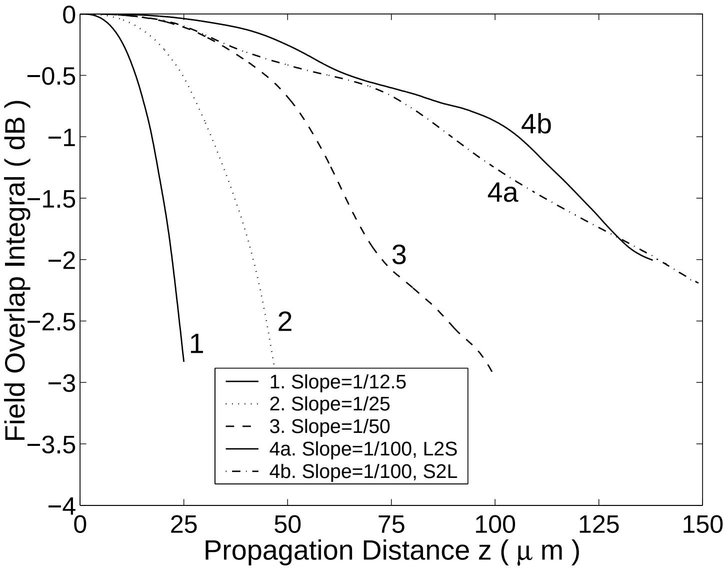

Figure 8.8: Field overlap integral between the propagating beam and the input local normal mode.

8.4 Summary

Our general design procedures enable the realization of SOI polarization converters with cross-section varying from submicron to tens of micrometers. Therefore, by employing large cross-section SOI polarization converters and corresponding input/output rib waveguides rather than small III-V counterparts, coupling loss to commercial single-mode fibers or laser diodes could be greatly reduced meanwhile strong polarization conversion is maintained. Due to the strong optical confinement, adjacent SOI polarization rotators can be situated very closely to each other, enabling large-scale waveguide arrays and high-density integrations. By maintaining single-mode cross-section in a tapered waveguide, the excess loss could be very small even for fast variation in the longitudinal direction; therefore the power transfer efficiency is greatly improved. Consequently, our compact low-loss polarization converters will have wide applications in high-performance large-scale optoelectronic integrated circuits (OEIC).

Chapter 9

Conclusion and Future Topics

This chapter draws conclusions from previous chapters and proposes promising topics for future research.

9.1 Conclusion

With the aid of efficient and accurate finite-element analysis, we have realized a category of novel passive polarization converters by employing the fast-developing silicon-on-insulator technology. Our general design procedures enable rapid and precise design of polarization manipulating devices, regardless of the outer slab layer configuration and the thickness of silicon guiding film of SOI wafers. These procedures apply to devices made of low index-contrast III-V materials (GaAs/AlGaAs and InP/InGaAsP, etc.) as well, although associated design charts could not be normalized as for SOI designs. The technique to etch the angled-facet along the crystallographic plane and remove the external waveguiding layer beside the sloped sidewall greatly enhances both the fabrication feasibility and the performance of slanted-angle polarization rotators. Characteristics related to the device size, fabrication tolerance, bending, loss and coupling have been thoroughly studied for asymmetric SOI polarization rotators, and merits over III-V counterparts have been addressed. Experimental verifications [5, 7, 8] have shown good agreement with theoretical analysis and have confirmed the promising characteristics of novel asymmetric SOI polarization converters.

Our sophisticated and versatile numerical finite-element packages can be widely employed for various problems of guided-wave and beam-propagation analysis in integrated photonics, and have the potential to be commercialized since currently available software is mainly based on the finite-difference method whose deficiency has already been pointed out earlier.

9.2 Suggestions for Future Research

This research focuses on designing and analyzing integrated optical devices with finite-element techniques, and we have found interesting research topics for both numerical algorithms and silicon photonics.

1. Suggested future topics for numerical algorithms:
    - Adaptive remeshing by eliminating and combining triangles in relatively less important regions. The adaptive mesh refinement employed in this dissertation simply subdivides elements.
    - Node renumbering to reduce matrix bandwidth and increase calculation efficiency. This function is especially desired for adaptive mesh generation.
    - FE-BPM with nodal triangular elements combined with methods to eliminate spurious modes. The mesh interpolation between tangential and nodal variables seems to be a cumbersome task and wastes much computer resource for each step of propagation based on mixed elements and adaptive meshing.
    - Tapered-BPM employing FEM procedures. In conventional BPM algorithms, the stair-case approximation in the propagation direction could cause the accumulation of numerical errors.
2. Suggested future topics for silicon photonics:
    - Improved experimental verification of asymmetrical SOI polarization rotators. Advanced fabrication procedures involving nano-photonics could be employed to enhance the device performance. More studies on single-mode and bending characteristics could be experimentally carried out.

- Other SOI taper structures for better coupling efficiency in silicon photonics;
- Application of SOI polarization converters in large scale arrayed-waveguide gratings (AWG);
- Investigating polarization beam splitters by utilizing SOI technology.

Appendix A

Derivation of the Polarization Conversion Efficiency Formula

For a birefringent optical waveguide, the phase delay ϑ between the two fundamental polarizations after propagating a distance L is expressed as Eq. (2.2), and is related to the half-beat length L_π (Eq. (2.3)) as

$$\vartheta = \pi \frac{L}{L_\pi} \tag{A.1}$$

In the orthogonal coordinate system formed by the optical-axes (u, v) as shown in Fig. 2.4, the related Jones matrix [277] is expressed as

$$[J_\varphi] = \begin{bmatrix} 1 & 0 \\ 0 & e^{-j\,\vartheta} \end{bmatrix} \tag{A.2}$$

In the fixed (x, y) coordinate, which is angled φ regarding to the optical-axes (u, v), this Jones matrix must be multiplied by a rotation matrix [58] $[R(\varphi)] = \begin{bmatrix} \cos\varphi & \sin\varphi \\ -\sin\varphi & \cos\varphi \end{bmatrix}$ according to this pattern [277]:

$$[J_0] = [R(-\varphi)][J_\varphi][R(\varphi)] = \begin{bmatrix} \cos^2\varphi + e^{-j\,\vartheta}\sin^2\varphi & \sin\varphi\,\cos\varphi\,(1-e^{-j\,\vartheta}) \\ \sin\varphi\,\cos\varphi\,(1-e^{-j\,\vartheta}) & \sin^2\varphi + e^{-j\,\vartheta}\cos^2\varphi \end{bmatrix} \tag{A.3}$$

The Jones vector for a TE-polarized (x-polarized) electric input field is

$$\begin{bmatrix} E_x^{in} \\ E_y^{in} \end{bmatrix} = \begin{bmatrix} 1 \\ 0 \end{bmatrix} \tag{A.4}$$

The corresponding output electric field is therefore calculated as

$$\begin{bmatrix} E_x^{out} \\ E_y^{out} \end{bmatrix} = [J_0] \begin{bmatrix} E_x^{in} \\ E_y^{in} \end{bmatrix} = \begin{bmatrix} \cos^2\varphi + e^{-j\,\vartheta}\sin^2\varphi \\ \sin\varphi\,\cos\varphi\,(1-e^{-j\,\vartheta}) \end{bmatrix} \tag{A.5}$$

Noting that the Jones matrices $[J_\varphi]$, $[R(\varphi)]$ and $[J_0]$ are unitary for linear lossless materials [278], so that $|E_x^{out}|^2 + |E_y^{out}|^2 = |E_x^{in}|^2 + |E_y^{in}|^2 = 1$. From Eq. (5.1), the polarization conversion efficiency is expressed in terms of output field components

$$PC_{\text{TE}\to\text{TM}} = \frac{|E_y^{out}|^2}{|E_x^{out}|^2 + |E_y^{out}|^2} \times 100\% = \sin^2\varphi\,\cos^2\varphi\,(2 - e^{j\,\vartheta} - e^{-j\,\vartheta}) \times 100\% \tag{A.6}$$

Utilizing Eq. (A.1) and the Euler's formula $e^{j\,\vartheta} = \cos\vartheta + j\,\sin\vartheta$, Eq. (A.6) becomes

$$PC = 2\,\sin^2\varphi\,\cos^2\varphi\,(1-\cos\vartheta) \times 100\% = 2\,\sin^2\varphi\,\cos^2\varphi\,(1-\cos(\pi\frac{L}{L_\pi})) \times 100\% \tag{A.7}$$

Further employing the half-angle formula $\cos 2\vartheta = 1 - 2\sin^2\vartheta$, the formulation for polarization conversion efficiency is simplified as

$$PC = 4\,\sin^2\varphi\,\cos^2\varphi\,\sin^2(\frac{\pi L}{2L_\pi}) \times 100\% \tag{A.8}$$

Eq. (5.2) is therefore proved for a TE-polarized input light. Similar procedure works for derivation with a TM-polarized input.

Bibliography

[1] H. Deng, D. O. Yevick, C. Brooks, and P. E. Jessop, "Design rules for slanted-angle polarization rotators," *J. Lightwave Technol.*, vol. 23, no. 1, pp. 432–445, Jan. 2005.

[2] H. Deng and D. O. Yevick, "The nonunitarity of finite-element beam propagation algorithms," *IEEE Photon. Technol. Lett.*, vol. 17, no. 7, pp. 1429–1431, July 2005.

[3] H. Deng, D. O. Yevick, and S. K. Chaudhuri, "Bending characteristics of asymmetric SOI polarization rotators," *IEEE Photon. Technol. Lett.*, vol. 17, no. 10, Oct. 2005, in press.

[4] H. Deng, D. O. Yevick, C. Brooks, and P. E. Jessop, "The fabrication tolerance of silicon-on-insulator polarization rotators," *Journal of the Optical Society of America A (JOSA A)*, submitted for publication.

[5] C. Brooks, P. E. Jessop, H. Deng, D. O. Yevick, and G. Tarr, "Passive polarization rotating waveguides in silicon-on-insulator," *Optical Engineering*, accepted for publication.

[6] H. Deng, D. O. Yevick, C. Brooks, and P. E. Jessop, "Design procedures for slanted-angle SOI polarization rotators," in *OSA/IEEE Proc. Optical Fiber Communication Conference (OFC'04)*, Los Angles, CA, Feb. 22-27, 2004, paper MF-41.

[7] C. Brooks, P. E. Jessop, H. Deng, D. O. Yevick, and G. Tarr, "Polarization rotating waveguides in silicon on insulator," in *OSA Proc. Integrated Photonics Research Conference (IPR'04)*, San Francisco, CA, June 30-July 2, 2004, paper IFG4.

[8] C. Brooks, “Polarization rotating waveguides in silicon-on-insulator,” Master’s thesis, McMaster University, Hamilton, Ontario, Canada, 2005.

[9] Y. C. Zhu, U. Khalique, J. J. G. M. van der Tol, E. J. Geluk, F. H. Groen, F. Karouta, and M. K. Smit, “Ultrashort, highly effiecient integrated optical polarization converter,” in *12th European Conference on Integrated Optics (ECIO’05)*, Grenoble, France, Apr. 6-8, 2005, pp. 96–99, paper WeB1-2.

[10] U. Khalique, Y. C. Zhu, J. J. G. M. van der Tol, L. M. Augustin, R. Hanfoug, F. H. Groen, P. J. van Veldhoven, M. K. Smit, M. van de Moosdijk, W. de Laat, and K. Simon, “Ultrashort polarization converter on InP/InGaAsP fabricated by optical lithography,” in *Integrated Photonics Research and Applications topical meeting (IPRA’05)*, San Diego, CA, Apr. 11-13, 2005, pp. 1–3, paper IWA3.

[11] R. C. Alferness, “Guided-wave devices for optical communication (invited paper),” *IEEE J. Quantum Electron.*, vol. QE-17, no. 6, pp. 946–959, June 1981.

[12] R. C. Alferness and L. L. Buhl, “Waveguide electro-optic polarization transformer,” *Appl. Phys. Lett.*, vol. 38, no. 9, pp. 655–657, May 1981.

[13] K. Yamanouchi, K. Higuchi, and K. Shibayama, “TE-TM mode conversion by interaction between elastic surface waves and a laser beam on a metal-diffused optical waveguide,” *Appl. Phys. Lett.*, vol. 28, no. 2, pp. 75–77, Jan. 1976.

[14] K. Yamanouchi, K. Wakazono, and K. Shibayama, “Optical surface wave mode converters and modulators utilizing static strain-optica effects,” *IEEE J. Quantum Electron.*, vol. QE-16, no. 6, pp. 628–634, June 1980.

[15] Y. Shani, R. Alferness, T. Koch, U. Koren, M. Oron, B. I. Miller, and M. G. Young, “Polarization rotation in asymmetric periodic loaded rib waveguides,” *Appl. Phys. Lett.*, vol. 59, no. 11, pp. 1278–1280, Sept. 1991.

[16] H. Heidrich, P. Albrecht, M. Hamacherm, H.-P. Nolting, H. Schroeter-Janβen, and C. M. Weinert, “Passive mode converter with a periodically titlted InP/GaInAsP rib waveguide,” *IEEE Photon. Technol. Lett.*, vol. 4, no. 1, pp. 34–36, Jan. 1992.

[17] C. M. Weinert and H. Heidrich, “Vectorial simulation of passive TE/TM mode converter devices on InP,” *IEEE Photon. Technol. Lett.*, vol. 5, no. 3, pp. 324–326, Mar. 1993.

[18] J. J. G. M. van der Tol, F. Hakimzadeh, J. W. Pedersen, D. Li, and H. van Brug, “A new short and low-loss passive polarization converter on InP,” *IEEE Photon. Technol. Lett.*, vol. 7, no. 1, pp. 32–34, Jan. 1995.

[19] J. J. G. M. van der Tol, J. W. Pedersen, E. G. Metaal, F. Hakimzadeh, Y. S. Oei, F. H. Groen, and I. Moerman, “Realization of a short integrated optic passive polarization converter,” *IEEE Photon. Technol. Lett.*, vol. 7, no. 8, pp. 893–895, Aug. 1995.

[20] T. Lang, F. Bahnmüller, and P. Benech, “New passive polarization converter on glass substrate,” *IEEE Photon. Technol. Lett.*, vol. 10, no. 9, pp. 1295–1297, Sept. 1998.

[21] C. van Dam, L. H. Spickman, F. P. G. M. van Ham, F. H. Groen, J. J. G. M. van der Tol, I. Moerman, W. W. Pascher, M. Hamacher, H. Heidrich, C. M. Weinert, and M. K. Smit, “Novel compact polarization converters based on ultra short bends,” *IEEE Photon. Technol. Lett.*, vol. 8, no. 10, pp. 1346–1348, Oct. 1996.

[22] C. van Dam, “InP-based polarisation independent wavelength demultiplexers,” Ph.D. dissertation, Delft University of Technology, Delft, The Netherlands, 1997.

[23] W. W. Lui, K. Magari, N. Yoshimoto, S. Oku, T. Hirono, K. Yokoyama, and W.-P. Huang, “Modeling and design of bending waveguide based semiconductor polarization rotators,” *IEEE Photon. Technol. Lett.*, vol. 9, no. 10, pp. 1379–1381, Oct. 1997.

[24] W. W. Lui, C.-L. Xu, T. Hirono, K. Yokoyama, and W.-P. Huang, “Full-vectorial wave propagation in semiconductor optical bending waveguides and equivalent straight waveguide approximations,” *J. Lightwave Technol.*, vol. 16, no. 5, pp. 910–914, May 1998.

[25] W. W. Lui, T. Hirono, K. Yokoyama, and W.-P. Huang, “Polarization rotation in semiconductor bending waveguides: A coupled-mode theory formulation,” *J. Lightwave Technol.*, vol. 16, no. 5, pp. 929–936, May 1998.

[26] B. E. Little and S. T. Chu, "Theory of polarization rotation and converqion in vertically coupled microsesonators," *IEEE Photon. Technol. Lett.*, vol. 12, no. 4, pp. 401–403, Apr. 2000.

[27] S. S. A. Obayya, B. M. A. Rahman, K. T. V. Grattan, and H. A. El-Mikati, "Beam propagation modeling of polarization rotation in deeply etched semiconductor bent waveguides," *IEEE Photon. Technol. Lett.*, vol. 13, no. 7, pp. 681–683, July 2001.

[28] K. Mertens, B. Scholl, and H. J. Schmitt, "Strong polarization conversion in periodically mloaded strip waveguides," *IEEE Photon. Technol. Lett.*, vol. 10, no. 8, pp. 1133–1135, Aug. 1998.

[29] W.-P. Huang and Z. M. Mao, "Polarization rotation in periodic loaded rib waveguides," *J. Lightwave Technol.*, vol. 10, no. 12, pp. 1825–1831, Dec. 1992.

[30] M. Gustavsson, "Analysis of polarization independent optical amplifiers and filters based on polarization rotation in periodically asymmetric waveguides," *IEEE J. Quantum Electron.*, vol. 29, no. 4, pp. 1168–1178, Apr. 1993.

[31] D. Li, H. van Brug, and H. J. Frankena, "Application of a fully vectorial beam propagation method," *Optical and Quantum Electronics*, vol. 29, pp. 313–322, 1997.

[32] T. Ando, T. Murata, H. Nakayama, J. Yamauchi, and H. Nakano, "Analysis and measurement of polarization conversion in a periodically loaded dielectric waveguide," *IEEE Photon. Technol. Lett.*, vol. 14, no. 9, pp. 1288–1290, Sept. 2002.

[33] S.-T. Chu and S. K. Chaudhuri, "A finite-difference time-domain method for the design and analysis of guided-wave optical structures," *J. Lightwave Technol.*, vol. 7, no. 12, pp. 2033–2028, Dec. 1989.

[34] A. Taflove and S. C. Hagness, *Computational Electrodynamics, the Finite-Difference Time-Domain Method*, 2nd ed. Norwood, MA: Artech House, 2000.

[35] F. J. Mustieles, E. Ballesteros, and F. Hernández-Gil, "Multimodal analysis method for the design of passive TE/TM converters in integrated waveguides," *IEEE Photon. Technol. Lett.*, vol. 5, no. 7, pp. 809–811, July 1993.

[36] S. S. A. Obayya, B. M. A. Rahman, and H. A. El-Mikati, “Vector beam propagation analysis of polarization conversion in periodically loaded waveguides,” *IEEE Photon. Technol. Lett.*, vol. 12, no. 10, pp. 1346–1348, Oct. 2000.

[37] K. Mertens, B. Scholl, and H. J. Schmitt, “New highly efficient polarization converters based on hybrid supermodes,” *J. Lightwave Technol.*, vol. 13, no. 10, pp. 2087–2092, Oct. 1995.

[38] K. Mertens, B. Opitz, R. Hövel, K. Heime, and H. J. Schmitt, “First realized polarization converter based on hybrid supermodes,” *IEEE Photon. Technol. Lett.*, vol. 10, no. 3, pp. 388–390, Mar. 1998.

[39] V. P. Tzolov and M. Fontaine, “Theoretical analysis of birefringence and form-induced polarization mode dispersion in birefringent optical fibers: A full-vectorial approach,” *J. Appl. Phys.*, vol. 77, no. 1, pp. 1–6, Jan. 1995.

[40] ——, “A passive polarization converter free of longitudinally-periodic structure,” *Optics Communications*, vol. 127, pp. 7–13, June 1996.

[41] J. Z. Huang, R. Scarmozzino, G. Nagy, M. J. Steel, and R. M. Osgood, Jr., “Realization of a compact and single-mode optical passive polarization converter,” *IEEE Photon. Technol. Lett.*, vol. 12, no. 3, pp. 317–319, Mar. 2000.

[42] Z. Huang, “Design and fabrication of integrated optical waveguide devices,” Ph.D. dissertation, Columbia University, New York, NY, 1999.

[43] Y. C. Zhu, F. H. Groen, D. H. P. Maat, X. J. M. Leijtens, and M. K. Smit, “Design of a short polarization converter on InP/InGaAsP using asymmetrical waveguides,” in *Proceedings 2000 IEEE/LEOS Symposium Benelux Chapter*, Delft University of Technology, The Netherlands, Oct. 30, 2000, pp. 227–230.

[44] Y. C. Zhu, F. H. Groen, X. J. M. Leijtens, and J. J. G. M. van der Tol, “Single-section polarisation converter on InP/InGaAsP using asymmetrical waveguides,” in *Proceedings 2001 IEEE/LEOS Symposium Benelux Chapter*, Vrije Universiteit Brussel, Belgium, Dec. 3, 2001, pp. 209–212.

[45] F. H. Groen, Y. C. Zhu, and J. J. G. M. van der Tol, "Compact polarisation converter in InP/InGaAsP using an asymmetrical waveguide," in *11th European Conference on Integrated Optics (ECIO'03)*, J. Ctyroky, M. Hubalek, and F. Ondracek, Eds., Czech Technical University in Prague, Apr. 2-4, 2003, pp. 141–144.

[46] H. El-Refaei and D. Yevick, "Compact InGaAsP/InP polarization rotator," in *OSA Proc. Integrated Photonics Research Conf. (IPR'01)*, Monterey, CA, July 2001, ITuB5/1:3.

[47] ——, "An optimized InGaAsP/InP polarization converter employing asymmetric rib waveguides," *J. Lightwave Technol.*, vol. 21, no. 6, pp. 1544–1548, June 2003.

[48] H. El-Refaei, D. Yevick, and T. Jones, "Slanted-rib waveguide InGaAsP-InP polarization converters," *J. Lightwave Technol.*, vol. 22, no. 5, pp. 1352–1357, May 2004.

[49] B. M. A. Rahman, S. S. A. Obayya, N. Somasiri, M. Rajarajan, K. T. V. Grattan, and H. A. El-Mikathi, "Design and characterization of compact single-section passive polarization rotator," *J. Lightwave Technol.*, vol. 19, no. 4, pp. 512–519, Apr. 2001.

[50] N. Somasiri, B. M. A. Rahman, and S. S. A. Obayya, "Fabrication tolerance study of a compact passive polarization rotator," *J. Lightwave Technol.*, vol. 20, no. 4, pp. 751–757, Apr. 2002.

[51] S. S. A. Obayya, N. Somasiri, B. M. A. Rahman, and K. T. V. Grattan, "Full vectorial finite element modeling of novel polarization rotator," *Optical and Quantum Electronics*, vol. 35, no. 3, pp. 297–312, Mar. 2003.

[52] L. Vincetti, A. Cucinotta, S. Selleri, and M. Zoboli, "Three-dimensional finite-element beam propagation method: assessments and developments," *J. Opt. Soc. Am. A*, vol. 17, no. 6, pp. 1124–1131, June 2000.

[53] D. Correia, J. P. da Silva, and H. E. Hernández-Figueroa, "Genetic algorithm and finite-element design of short single-section passive polarization converter," *IEEE Photon. Technol. Lett.*, vol. 15, no. 7, pp. 915–917, July 2003.

[54] T. Lu and D. Yevick, “A vectorial boundary element method analysis of integrated optical waveguides,” *J. Lightwave Technol.*, vol. 21, no. 8, pp. 1793–1807, Aug. 2003.

[55] K. Zhao and X. Zhong, *Optics (in Chinese).* Beijing, China: Peking University Press, 1984.

[56] G. P. Agrawal, *Nonlinear Fiber Optics.* San Diego, CA: Academic Press, 1989.

[57] ——, *Lightwave Technology: Components and Devices.* Hoboken, NJ: Wiley-Interscience, 2004.

[58] M. Mrozowski, *Guided electromagnetic waves: properties and analysis.* England: Research Studies Press Ltd. / John Wiley & Sons Inc., 1997.

[59] A. W. Snyder and J. D. Love, *Optical Waveguide Theory.* London: Chapman & Hall, 1983.

[60] G. T. Reed and A. P. Knights, *Silicon Photonics: an introduction.* Wiley, 2004.

[61] G. T. Reed, “The optical age of silicon,” *Nature*, vol. 427, pp. 595–596, Feb. 12, 2004.

[62] M. Salib, L. Liao, R. Jones, M. Morse, A. Liu, D. Samara-Rubio, D. Alduino, and M. Paniccia, “Silicon photonics,” *Intel® Technology Journal*, vol. 08, no. 02, pp. 142–160, May 10, 2004.

[63] L. Pavesi, “Will silicon be the photonic material of the third millenium?” *Journal of Physics: Condensed Matter*, vol. 15, pp. R1169–1196, July 9, 2003.

[64] R. A. Soref, “Silicon-based optoelectronics (invited paper),” *Proceedings of the IEEE*, vol. 81, no. 12, pp. 1687–1706, Dec. 1993.

[65] R. A. Soref and B. R. Bennett, “Electrooptical effects in silicon,” *IEEE J. Quantum Electron.*, vol. QE-23, no. 1, pp. 123–129, Jan. 1987.

[66] B. Jalali, S. Yegnanarayanan, T. Yoon, T. Yoshimoto, I. Rendina, and F. Coppinger, “Advances in silicon-on-insulator optoelectronics (invited paper),” *IEEE J. Select. Topics Quantum Electron.*, vol. 4, no. 6, pp. 938–947, Nov./Dec. 1998.

[67] A. V. Krishnamoorthy and K. W. Goossen, “Optoelectronic-VLSI: Photonics integrated with VLSI circuits,” *IEEE J. Select. Topics Quantum Electron.*, vol. 4, no. 6, pp. 899–912, Nov./Dec. 1998.

[68] T. Aalto, “Microphotonic silicon waveguide components,” Ph.D. dissertation, Helsinki University of Technology, Espoo, Finland, Dec. 2004.

[69] A.-J. Auberton-Herve, “In just 20 years: An SOI journey,” *Semiconductor International*, vol. 27, no. 1, pp. 74–75, Jan. 2004.

[70] J. B. Kuo and S.-C. Lin, *Low-Voltage SOI CMOS VLSI Devices and Circuits.* New York: Wiley, 2001.

[71] S. R. Giguere, L. Friedman, R. A. Soref, and J. P. Lorenzo, “Simulation of silicon electo-optic waveguide devices,” *J. Appl. Phys.*, vol. 68, no. 10, pp. 4964–4970, Nov. 15, 1990.

[72] M. R. T. Pearson, A. Bezinger, A. Delâge, J. W. Fraser, S. Janz, P. E. Jessop, and D.-X. Xu, “Arrayed waveguide grating demultiplexers in silicon-on-insulator,” in *Silica-based Optoelectronics II*, D. J. Robbins and D. C. Houghton, Eds., vol. 3953. SPIE, Mar. 2000, pp. 11–18.

[73] A. Rickman, G. T. Reed, B. L. Weiss, and F. Namavar, “Low-loss planar optical waveguides fabricated in SIMOX material,” *IEEE Photon. Technol. Lett.*, vol. 4, no. 6, pp. 633–635, June 1992.

[74] C. K. Tang, G. T. Reed, A. J. Walton, and A.G.Rickman, “Low-loss, single-mode, optical phase modulator in SIMOX material,” *J. Lightwave Technol.*, vol. 12, no. 8, pp. 1394–1400, Aug. 1994.

[75] A. Liu, R. Jones, L. Liao, D. Samara-Rubio, D. Rubin, O. Cohen, R. Nicolaescu, and M. Paniccia, “A high-speed silicon optical modulator based on a metal-oxide-semiconductor capacitor,” *Nature*, vol. 427, pp. 615–618, Feb. 12, 2004.

[76] C. E. Png, S. P. Chan, S. T. Lim, and G. T. Reed, "Optical phase modulators for MHz and GHz modulation in silicon-on-insulator (SOI)," *J. Lightwave Technol.*, vol. 22, no. 6, pp. 1573–1582, June 2004.

[77] M. K. Emsley, O. Dosunmu, and M. S. Ünlü, "High-speed resonant-cavity-enhanced silicon photodetectors on reflecting silicon-on-insulator substrates," *IEEE Photon. Technol. Lett.*, vol. 14, no. 4, pp. 519–521, Apr. 2002.

[78] P. D. Trinh, S. Yegnanarayanan, and B. Jalali, "Integrated optical directional couplers in silicon-on-insulator," *IEE Electron. Lett.*, vol. 31, no. 24, pp. 2097–2098, Nov. 1995.

[79] G. V. Treyz, P. G. May, and J.-M. Halbout, "Silicon Mach-Zehnder waveguide interferometers based on the plasma dispersion effect," *Appl. Phys. Lett.*, vol. 59, no. 7, pp. 771–773, Aug. 1991.

[80] C. Z. Zhao, G. Z. Li, E. K. Liu, Y. Gao, and X. D. Liu, "Silicon on insulator Mach-Zehnder waveguide interferometers operating at 1.3 μm," *Appl. Phys. Lett.*, vol. 67, no. 17, pp. 2448–2449, Oct. 1995.

[81] R. U. Ahmad, F. Pizzuto, G. S. Camarda, R. L. Espinola, H. Rao, and R. M. Osgood, Jr., "Ultracompact corner-mirrors and T-branches in silicon-on-insulator," *IEEE Photon. Technol. Lett.*, vol. 14, no. 1, pp. 65–67, Jan. 2002.

[82] Y. Wang, Z. Lin, C. Zhang, and F. Zhang, "Large cross section Y-branch with new fiber-waveguide endface in silicon-on-insulator," *IEEE Photon. Technol. Lett.*, vol. 16, no. 11, pp. 2493–2495, Nov. 2004.

[83] T. W. Ang, G. T. Reed, A. Vonsovici, A. G. R. Evans, P. R. Routley, and M. R. Josey, "Effects of grating heights on highly efficient unibond SOI waveguide grating couplers," *IEEE Photon. Technol. Lett.*, vol. 12, no. 1, pp. 59–61, Jan. 2000.

[84] T. E. Murphy, J. T. Hastings, and H. I. Smith, "Fabrication and characterization of narrow-band bragg-reflection filters in silicon-on-insulator ridge waveguides," *J. Lightwave Technol.*, vol. 19, no. 12, pp. 1938–1942, Dec. 2001.

[85] P. Trinh, S. Yegnananyanan, and B. Jalali, "5×9 integrated optical star coupler in silicon-on-insulator technology," *IEEE Photon. Technol. Lett.*, vol. 8, no. 6, pp. 794–796, June 1996.

[86] H. Wei, J. Yu, Z. Liu, X. Zhang, W. Shi, and C. Fang, "Fabrication of 4 × 4 tapered MMI coupler with large cross section," *IEEE Photon. Technol. Lett.*, vol. 13, no. 5, pp. 466–468, May 2001.

[87] S. Yegnanarayanan, P. D. Trinh, F. Coppinger, and B. Jalali, "Compact silicon-based integrated optic time delays," *IEEE Photon. Technol. Lett.*, vol. 9, no. 5, pp. 634–636, May 1997.

[88] P. D. Trinh, S. Yegnanarayanan, F. Coppinger, and B. Jalali, "Silicon-on-insulator (SOI) phased-array wavelength multi/demultiplexer with extremely low-polarization sensitivity," *IEEE Photon. Technol. Lett.*, vol. 9, no. 7, pp. 940–942, July 1997.

[89] M. R. T. Pearson, "Si-based optoelectronics: Monolithic integration for WDM," Ph.D. dissertation, McMaster University, Hamilton, Ontario, Canada, 2000.

[90] R. A. Soref, J. Schmidtchen, and K. Petermann, "Large single-mode rib waveguides in GeSi-Si and Si-on-SiO_2," *IEEE J. Quantum Electron.*, vol. 27, no. 8, pp. 1971–1974, Aug. 1991.

[91] J. Schmidtchen, A. Splett, B. Schoppert, and K. Petermann, "Low loss singlemode optical waveguides with large cross-section in silcion-on-insulator," *IEE Electron. Lett.*, vol. 27, no. 16, pp. 1486–1488, Aug. 1991.

[92] T. Zinke, U. Fischer, A. Splett, B. Schuppert, and K. Petermann, "Comparision of optical waveguide losses in silicon-on-insulator," *IEE Electron. Lett.*, vol. 29, no. 23, pp. 2031–2033, Nov. 1993.

[93] U. Fischer, T. Zinke, B. Schuppert, and K. Petermann, "Singlemode optical switches based on SOI waveguides with large cross-section," *IEE Electron. Lett.*, vol. 30, no. 5, pp. 406–408, Mar. 1994.

[94] U. Fischer, T. Zinke, J.-R. Kropp, F. Amdi, and L. Petermann, “0.1dB/cm waveguide losses in single-mode SOI rib waveguides,” *IEEE Photon. Technol. Lett.*, vol. 8, no. 5, pp. 647–648, May 1996.

[95] A. G. Rickman, G. T. Reed, and F. Namavar, “Silicon-on-insulator optical rib waveguide loss and mode characteristics,” *J. Lightwave Technol.*, vol. 12, no. 10, pp. 1771–1776, Oct. 1994.

[96] A. G. Rickman and G. T. Reed, “Silicon-on-insulator optical rib waveguides: loss, mode characteristics, bends and y-junctions,” *IEE Proc.-Optoelectron.*, vol. 141, no. 6, pp. 391–393, Dec. 1994.

[97] C. K. Tang, A. Kewell, G. Reed, A. Rickman, and F. Namavar, “Development of a library of low-loss insulator optoelectronic devices,” *IEE Proc.-Optoelectron.*, vol. 143, no. 5, pp. 312–315, Oct. 1996.

[98] S. P. Pogossian, L. Vescan, and A. Vonsovici, “The single-mode condition for semiconductor rib waveguides with large cross section,” *J. Lightwave Technol.*, vol. 16, no. 10, pp. 1851–1853, Oct. 1998.

[99] O. Powell, “Single-mode condition for silicon rib waveguides,” *J. Lightwave Technol.*, vol. 20, no. 10, pp. 1851–1855, Oct. 2002.

[100] J. Lousteau, D. Furniss, A. B. Seddon, T. M. Benson, A. Vukovic, and P. Sewell, “The single-mode condition for silicon-on-insulator optical rib waveguides with large cross section,” *J. Lightwave Technol.*, vol. 22, no. 8, pp. 1923–1929, Aug. 2004.

[101] J. Xia and J. Yu, “Single-mode condition for silicon rib waveguides with trapezoidal cross-section,” *Optics Communications*, vol. 230, no. 4-6, pp. 253–257, Feb. 2004.

[102] S. P. Chan, C. E. Png, S. T. Lim, G. T. Reed, and V. M. N. Passaro, “Single-mode and polarization-independent silicon-on-insulator waveguides with small cross section,” *J. Lightwave Technol.*, vol. 23, no. 6, pp. 2103–2110, June 2005.

[103] O. C. Zienkiewicz, *The Finite Element Method.* London & Montreal: Mcgraw-Hill, 1977.

[104] O. C. Zienkiewicz and R. L. Taylor, *The Finite Element Method*, 5th ed. Oxford & Boston: Butterworth-Heinemann, 2000.

[105] P. P. Silvester, "Finite-element solution of homogenous waveguide problems," *Alta Frequenza*, vol. 38, pp. 313–317, 1969.

[106] ——, "A general high-order finite-element waveguide analysis program," *IEEE Trans. Microwave Theory Tech.*, vol. MTT-17, no. 4, pp. 204–210, Apr. 1969.

[107] Z. J. Csendes and P. P. Silvester, "Numerical solution of dielectric loaded waveguides: I–finite-element analysis," *IEEE Trans. Microwave Theory Tech.*, vol. MTT-18, no. 12, pp. 1124–1131, Dec. 1970.

[108] P. P. Silvester and G. Pelosi, Eds., *Finite Elements for Wave Electromagnetics: Methods and Techniques.* New York: IEEE Press, 1994.

[109] P. P. Silvester and R. L. Ferrari, *Finite Elements for Electrical Engineers*, 3rd ed. Cambridge University Press, 1996.

[110] M. N. O. Sadiku, *Numerical Techniques in Electromagnetics*, 1st ed. CRC Press, 1992.

[111] ——, *Numerical Techniques in Electromagnetics*, 2nd ed. CRC Press, 2001.

[112] S. M. Saad, "Review of numerical methods for the analysis of arbitrarily-shaped microwave and optical dielectric waveguides," *IEEE Trans. Microwave Theory Tech.*, vol. MTT-33, no. 10, pp. 894–899, Oct. 1985.

[113] K. S. Chiang, "Review of numerical and approximate methods for the modal analysis of general optical dielectric waveguides (invited paper)," *Optical and Quantum Electronics*, vol. 26, pp. S113–S134, 1994.

[114] C. Vassallo, "1993-1995 optical mode solvers," *Optical and Quantum Electronics*, vol. 29, pp. 95–114, 1997.

[115] R. Scarmozzino, A. Gopinath, R. Pregla, and S. Helfert, “Numerical techniques for modeling guided-wave photonic devices (invited paper),” *IEEE J. Select. Topics Quantum Electron.*, vol. 6, no. 1, pp. 150–162, Jan./Feb. 2000.

[116] M. Koshiba, *Optical Waveguide Analysis.* New York: McGraw-Hill, 1992.

[117] ——, *Optical Waveguide Theory by the Finite Element Method.* KTK Scientific Publishers (Tokyo) / Kluwer Academic Press, 1992.

[118] ——, “The finite-element method,” in *Analysis Methods for Electromagnetic Wave Problems*, E. Yamashita, Ed. Artech House, 1990, ch. 1, pp. 1–31.

[119] J. Jin, *Finite Element Method in Electromagnetics.* Wiley, 1993.

[120] ——, *The Finite Element Method in Electromagnetics*, 2nd ed. New York: John Wiley & Sons, 2002.

[121] J. L. Volakis, A. Chatterjee, and L. C. Kempel, *Finite Element Method for Electromagnetics: Antennas, Microwave Circuits, and Scattering Applications.* New York: IEEE Press, 1998.

[122] F. A. Fernández and Y. Lu, *Microwave and Optical Waveguide Analysis by the Finite Element Method.* Research Studies Press Ltd. / John Wiley & Sons Inc., 1996.

[123] G. Pelosi, R. Coccioli, and S. Selleri, *Quick Finite Elements for Electromagnetic Waves.* Boston & London: Artech House, 1998.

[124] K. Okamoto, *Fundamentals of Optical Waveguides.* Academic Press, 2000.

[125] K. Kawano and T. Kitoh, *Introduction to Optical Waveguide Analysis: Solving Maxwell’s Equations and the Schrödinger Equation.* Wiley, 2001.

[126] M. S. Stern, “Semivectorial polarised finite difference method for optical waveguides with arbitrary index profiles,” *IEE Proceedings Pt. J.*, vol. 135, no. 1, pp. 56–63, Feb. 1988.

[127] H. Dong, A. Chronopoulos, J. Zou, and A. Gopinath, “Vectorial integrated finite-difference analysis of dielectric waveguides,” *J. Lightwave Technol.*, vol. 13, no. 10, pp. 1559–1563, Oct. 1993.

[128] C. Xu, “Finite-difference techniques for simulation of vectorial wave propagation in photonic guide-wave devices,” Ph.D. dissertation, University of Waterloo, Waterloo, Ontario, Canada, 1994.

[129] C. L. Xu and W. P. Huang, “Finite-difference beam-propagation method for guide-wave optics,” in *Progress In Electromagnetic Waves: PIERS 11*, W. P. Huang, Ed. EMW Publishing, Cambridge, 1995, ch. 1, pp. 1–49.

[130] D. M. Sullivan, *Electromagnetic Simulation using the FDTD Method.* New York: IEEE Press, 2000.

[131] J.-S. Gu, P.-A. Besse, and H. Melchior, “Method of lines for the analysis of the propagation characteristics of curved optical rib waveguides,” *IEEE J. Quantum Electron.*, vol. 27, no. 3, pp. 531–537, Mar. 1991.

[132] M. M. Ney, “Method of moments as applied to electromagnetic problems,” *IEEE Trans. Microwave Theory Tech.*, vol. MTT-33, no. 10, pp. 972–980, Oct. 1985.

[133] W. Yang and A. Gopinath, “A boundary integral method for propagation problems in integrated optical structures,” *J. Lightwave Technol.*, vol. 7, no. 7, pp. 777–779, July 1995.

[134] T. Lu, “Boundary element analysis of dielectric waveguides,” Master’s thesis, Queen’s University, Kingston, Ontario, Canada, 1998.

[135] T. B. Koch, J. B. Davies, and D. Wickramasinghe, “Finite element/finite difference propagation algorithm for integrated optical devices,” *IEE Electron. Lett.*, vol. 25, no. 8, pp. 514–516, Apr. 1989.

[136] Y. Arai, A. Maruta, and M. Matsuhara, “Transparent boundary for the finite-element beam-propagation method,” *Opt. Lett.*, vol. 18, no. 10, pp. 765–766, May 1993.

[137] H. E. Hernández-Figueroa, “Simple nonparaxial beam-propagation method for integrated optics,” *J. Lightwave Technol.*, vol. 12, no. 4, pp. 644–649, Apr. 1994.

[138] Y. Tsuji and M. Koshiba, “A finite-element beam-propagation method for strongly guiding and longitudinally varying optical waveguides,” *J. Lightwave Technol.*, vol. 14, no. 2, pp. 217–222, Feb. 1996.

[139] Y. Tsuji, M. Koshiba, and T. Tanabe, “A wide-angle beam propagatiom method based on a finite element scheme,” *IEEE Trans. Magn.*, vol. 33, no. 2, pp. 1544–1547, Mar. 1997.

[140] Y. Tsuji, M. Koshiba, and T. Shiraishi, “Finite element beam propagation method for three-dimensional optical waveguide structures,” *J. Lightwave Technol.*, vol. 15, no. 9, pp. 1728–1734, Sept. 1997.

[141] D. Yevick, “A guide to electric field propagation techniques for guided-wave optics (invited paper),” *Optical and Quantum Electronics*, vol. 26, pp. S185–S197, 1994.

[142] L. Thylen and D. Yevick, “Beam propagation method in anisotropic media,” *Applied Optics*, vol. 21, pp. 2751–2754, Aug. 1982.

[143] P. Danielsen and D. Yevick, “Improved analysis of the propagating beam method in longitudinally perturbed optical waveguide,” *Applied Optics*, vol. 21, no. 23, pp. 4188–4189, Dec. 1982.

[144] H.-P. Nolting and R. März, “Results of benchmark tests for different numerical BPM algorithms,” *J. Lightwave Technol.*, vol. 13, no. 2, pp. 216–224, Feb. 1995.

[145] J. Haes *et al.*, “A comparison between different propagative schemes for the simulation of tapered step index slab waveguides,” *J. Lightwave Technol.*, vol. 14, no. 6, pp. 1557–1569, June 1996.

[146] H. J. W. M. Hoekstra, “On beam propagation methods for modelling in integrated optics,” *Optical and Quantum Electronics*, vol. 29, pp. 157–171, 1997.

[147] J. A. Fleck and M. D. Feit, “Beam propagation in uniaxial anisotropic media,” *J. Opt. Soc. Am.*, vol. 73, pp. 920–926, July 1983.

[148] J. Shibayama, A. Yamahira, T. Mugita, J. Yamauchi, and H. Nakano, “A finite-difference time-domain beam-propagation method for TE- and TM-wave analyses,” *J. Lightwave Technol.*, vol. 21, no. 7, pp. 1709–1715, July 2003.

[149] P.-L. George, *Automatic Mesh Generation: Application to Finite Element Methods.* New York: John Wiley & Sons, 1991.

[150] P.-L. George and H. Bourachaki, *Delaunay Triangulation and Meshing: Application to Finite Elements.* Paris: Hermes, 1998.

[151] P. J. Frey and P.-L. George, *Mesh Generation: application to finite elements.* Oxford & Paris: Hermes Science Publishing, 2000.

[152] D. Yevick, J. Yu, W. Bardyszewski, and M. Glasner, “Stability issues in vector electric field propagation,” *IEEE Photon. Technol. Lett.*, vol. 7, no. 6, pp. 658–660, June 1995.

[153] D. Yevick, “The application of complex Padé approximants to vector field propagation,” *IEEE Photon. Technol. Lett.*, vol. 12, no. 12, pp. 1636–1638, Dec. 2000.

[154] G. R. Hadley, “High-accuracy finite-difference equations for dielectric waveguide analysis I: Uniform regions and dielectric interfaces,” *J. Lightwave Technol.*, vol. 20, no. 7, pp. 1210–1218, July 2002.

[155] ——, “High-accuracy finite-difference equations for dielectric waveguide analysis II: Dielectric corners,” *J. Lightwave Technol.*, vol. 20, no. 7, pp. 1219–1231, July 2002.

[156] D. Z. Djurdjevic, P. Sewell, T. M. Benson, and A. Vukovic, “Highly efficient finite-difference schemes for structures of nonrectangular cross-section,” *Microwave and Optical Technology Letters*, vol. 33, no. 6, pp. 401–407, June 20, 2002.

[157] J. Xia and J. Yu, “New finite-difference scheme for simulations of step-index waveguides with tile interfaces,” *IEEE Photon. Technol. Lett.*, vol. 15, no. 9, pp. 1237–1239, Sept. 2003.

[158] T. Ando, H. Nakayama, J. Yamauchi, and H. Nakano, "Optical waveguide analysis using a Yee-lattice-based modified finite-difference formula for an arbitrary dielectric interface," *Electronics and Communications in Japan, Part 2*, vol. 85, no. 12, pp. 1–9, Dec. 2002.

[159] A. Splett, M. Majd, and K. Petermann, "A novel beam propagation method for large refractive index steps and large propagation distances," *IEEE Photon. Technol. Lett.*, vol. 3, no. 5, pp. 466–468, May 1991.

[160] P.-L. Liu and B.-J. Li, "Semivectorial beam-propagation method for analyzing polarizaed modes of rib waveguides," *IEEE J. Quantum Electron.*, vol. 28, no. 4, pp. 778–782, Apr. 1992.

[161] O. Mitomi, N. Yoshimoto, K. Magari, T. Ito, Y. Kawaguchi, Y. Suzaki, Y. Tohmori, and K. Kasaya, "Analyzing the polarization dependence in optical spot-size converter by using a semivectorial finite-element beam propagation method," *J. Lightwave Technol.*, vol. 17, no. 7, pp. 1255–1261, July 1999.

[162] K. Kawano, M. Kohtoku, H. Okamoto, Y. Itaya, and M. Naganuma, "Coupling and conversion characteristics of spot-size-converter integrated laser diodes," *IEEE J. Select. Topics Quantum Electron.*, vol. 3, no. 6, pp. 1351–1360, Dec. 1997.

[163] D. Z. Djurdjevic, T. M. Benson, P. Sewell, and A. Vukovic, "Fast and accurate analysis of 3-D curved optical waveguide couplers," *J. Lightwave Technol.*, vol. 22, no. 10, pp. 2333–2340, Oct. 2004.

[164] J. B. Davies, F. A. Fernández, and G. Y. Philippou, "Finite element analysis of all modes in cavities with circular symmetry," *IEEE Trans. Microwave Theory Tech.*, vol. MTT-30, no. 11, pp. 1975–1980, Nov. 1982.

[165] D. R. Lynch and K. D. Paulsen, "Origin of vector parasites in numerical maxwell solutions," *IEEE Trans. Microwave Theory Tech.*, vol. 39, no. 3, pp. 383–394, Mar. 1991.

[166] K. D. Paulsen and D. R. Lynch, “Elimination of vector parasites in finite element maxwell solutions,” *IEEE Trans. Microwave Theory Tech.*, vol. 39, no. 3, pp. 395–404, Mar. 1991.

[167] B. M. A. Rahman and J. B. Davies, “Finite-element analysis of optical and microwave waveguide problems,” *IEEE Trans. Microwave Theory Tech.*, vol. MTT-32, no. 1, pp. 20–28, Jan. 1984.

[168] ——, “Finite-element solution of intergrated optical waveguides,” *J. Lightwave Technol.*, vol. LT-2, no. 5, pp. 682–688, Oct. 1984.

[169] M. Silveira and A. Gopinath, “Analysis of dielectric guides by transverse magnetic field finite element penalty method,” *J. Lightwave Technol.*, vol. 13, no. 3, pp. 442–446, Mar. 1995.

[170] P. Cheung, M. Silveire, and A. Gopinath, “Correction to the analysis of dielectric guides by transvers magnetic field finite element penalty function method with extensions,” *J. Lightwave Technol.*, vol. 14, no. 12, pp. 2799–2803, Dec. 1996.

[171] K. Hayata, M. Koshiba, M. Eguchi, and M. Suzuki, “Vectorial finite-element method without any spurious solutions for dielectric waveguding problem using transverse magnetic-field component,” *IEEE Trans. Microwave Theory Tech.*, vol. MTT-34, no. 11, pp. 1120–1124, Nov. 1986.

[172] Z.-E. Abid, K. L. Johnson, and A. Gopinath, “Analysis of dielectric guides by vector transverse magnetic field finite elements,” *J. Lightwave Technol.*, vol. 11, no. 10, pp. 1545–1549, Oct. 1993.

[173] A. Bossavit, *Computational Electromagnetism: Variational Formulations, Complementarity, Edge Elements.* Boston: Academic Press, 1998.

[174] J.-F. Lee, D.-K. Sun, and Z. J. Cendes, “Full-wave analysis of dielectric waveguides using tangential vector finite elements,” *IEEE Trans. Microwave Theory Tech.*, vol. 39, no. 8, pp. 1262–1271, Aug. 1991.

[175] J. C. Nédélec, “Mixed finite elements in R^3,” *Numerische Mathematik*, vol. 35, pp. 315–341, 1980.

[176] ——, “A new family of mixed finite elements in R^3,” *Numerische Mathematik*, vol. 50, pp. 57–81, 1986.

[177] L. E. García-Castillo, A. J. Ruiz-Genovés, I. Gómez-Revuelto, M. Salazar-Palma, and T. K. Sarkar, “Third-order Nédélec curl-conforming finite element,” *IEEE Trans. Magn.*, vol. 38, no. 5, pp. 2370–2372, Sept. 2002.

[178] I. Tsukerman, “Symbolic algebra as a tool for understanding edge elements,” *IEEE Trans. Magn.*, vol. 39, no. 3, pp. 1111–1114, May 2003.

[179] M. Koshiba and K. Inoue, “Simple and efficient finite-element analysis of microwave and optical waveguides,” *IEEE Trans. Microwave Theory Tech.*, vol. 40, no. 2, pp. 371–377, Feb. 1992.

[180] M. Koshiba, S. Maruyama, and K. Hirayama, “A vector finite element method with the high-order mixed-interpolation-type triangular elements for optical waveguiding problems,” *J. Lightwave Technol.*, vol. 12, no. 3, pp. 495–502, Mar. 1994.

[181] M. Koshiba and Y. Tsuji, “Curvilinear hybrid edge/nodal elements with triangular shape for guided-wave problems,” *J. Lightwave Technol.*, vol. 18, no. 5, pp. 737–743, May 2000.

[182] D. Schulz, C. Glingener, M. Bludszuweit, and E. Voges, “Mixed finite element beam propagation method,” *J. Lightwave Technol.*, vol. 16, no. 7, pp. 1336–1342, July 1998.

[183] S. Selleri and M. Zoboli, “Performance comparison of finite-element approaches for electromagnetic waveguides,” *J. Opt. Soc. Am. A*, vol. 14, no. 7, pp. 1460–1466, July 1997.

[184] P. I. Davies, “Solving the symmetric definite generalized eigenvalue problem,” Ph.D. dissertation, University of Manchester, Manchester, United Kingdom, Dec. 2000.

[185] Y. Saad, *Iterative methods for sparse linear systems*, 2nd ed. Philadelphia: Society for Industrial and Applied Mathematics (SIAM), 2003.

[186] ——, *Numerical methods for large eigenvalue problems.* Manchester, United Kingdom: Manchester University Presss, 1992.

[187] J. Mielewski and M. Mrozowski, "Application of the Arnoldi method in FEM analysis of waveguides," *IEEE Microwave Guided Wave Lett.*, vol. 8, no. 1, pp. 7–9, Jan. 1998.

[188] B. M. A. Rahman, N. Somasiri, and M. Windmann, "Polarization crosstalk in high index contrast planar silica waveguides," *IEEE Photon. Technol. Lett.*, vol. 14, no. 8, pp. 1109–1111, Aug. 2002.

[189] K. Dossou, S. LaRochelle, and M. Fontaine, "Numerical analysis of the contribution of the transverse asymmetry in the photo-induced index change profile to the birefringence of optical fiber," *J. Lightwave Technol.*, vol. 20, no. 8, pp. 1463–1470, Aug. 2002.

[190] F. A. Fernández, Y. C. Yong, and R. D. Ettinger, "A simple adaptive mesh generator for 2-D finite element calculation," *IEEE Trans. Magn.*, vol. 29, no. 2, pp. 1882–1885, Mar. 1993.

[191] Z. J. Cendes, D. N. Shenton, and H. Shahnasser, "Magnetic field computation using delaunay triangulation and complementary finite element methods," *IEEE Trans. Magn.*, vol. MAG-19, no. 6, pp. 2551–2554, Nov. 1983.

[192] Z. J. Cendes and D. N. Shenton, "Adaptive mesh refinement in the finite element computation of magnetic fields," *IEEE Trans. Magn.*, vol. MAG-21, no. 5, pp. 1811–1816, Sept. 1985.

[193] Y. Tsuji and M. Koshiba, "Simple and efficient adaptive mesh generation for approxiamte scalar guided-mode and beam-propagation solutions," *IEICE Trans. Electron.*, vol. E81-C, no. 12, pp. 1814–1820, Dec. 1998.

[194] ——, "Adaptive mesh generation for full-vectorial guided-mode and beam-propagation solutions," *IEEE J. Select. Topics Quantum Electron.*, vol. 6, no. 1, pp. 163–169, Jan./Feb. 2000.

[195] P. Fernandes, P. Girdinio, P. Molfino, G. Molinari, and M. Repetto, "A comparison of adaptive strategies for mesh refinement based on 'a posteriori' local error estimation precedures," *IEEE Trans. Magn.*, vol. 26, no. 2, pp. 795–798, Mar. 1990.

[196] S. R. H. Hoole, "Eigen value and eigen vector perturbation and adaptive mesh generation in the analysis of waveguides," *IEEE Trans. Magn.*, vol. 26, no. 2, pp. 791–794, Mar. 1990.

[197] F. Schmidt, "An adaptive approach to the numerical solution of Fresnel's wave equation," *J. Lightwave Technol.*, vol. 11, no. 9, pp. 1425–1434, Sept. 1993.

[198] H. Deng, "Silicon on insulator (SOI) polarization independent arrayed waveguide gratings (AWG)," ECE Ph.D. Proposal, University of Waterloo, Ontario, Canada, Oct. 2002.

[199] M. S. Stern, "Semivectorial polarised $\boldsymbol{H}$ field solutions for dielectric waveguides with arbitrary index profiles," *IEE Proceedings Pt. J.*, vol. 135, no. 5, pp. 333–338, Oct. 1988.

[200] R. Baets, "Nano-photonic integrated circuits: the promise and the problems," presented at the Norwegian Electro-optics Meeting, Tønsberg, Norway, May 2-4, 2004.

[201] W. Bogaerts, R. Baets, P. Dumon, V. Wiaux, S. Beckx, D. Taillaert, B. Luyssaert, J. V. Campenhout, P. Bienstman, and D. V. Thourhout, "Nanophotonic waveguides in silicon-on-insulator fabricated with CMOS technology," *J. Lightwave Technol.*, vol. 23, no. 1, pp. 401–412, Jan. 2005.

[202] W. Bogaerts, "Nanophotonic waveguides and photonic crystals in silicon-on-insulator," Ph.D. dissertation, Ghent University, Ghent, Belgium, 2004.

[203] D. Taillaert, "Grating couplers as interface between optical fibres and nanophotonic waveguides," Ph.D. dissertation, Ghent University, Ghent, Belgium, 2004.

[204] I. Kiyat, A. Aydinli, and N. Dagli, “A compact silicon-on-insulator polarization splitter,” *IEEE Photon. Technol. Lett.*, vol. 17, no. 1, pp. 100–102, Jan. 2005.

[205] W. Wang, Y. Tang, Y. Wang, H. Qu, Y. Wu, T. Li, J. Yang, Y. Wang, and M. Liu, “Etched-diffraction-grating-based planar waveguide demultiplexer on silicon-on-insulator,” *Optical and Quantum Electronics*, vol. 36, pp. 559–566, May 2004.

[206] G. P. Nordin and P. C. Deguzman, “Broadband form birefringent quarter-wave plate for the mid-infrared wavelength region,” *OSA Optics Express*, vol. 5, no. 8, pp. 163–168, Oct. 11, 1999.

[207] “Special issue on alignment tolerant structures for ease of optoelectronic packaging (ATSEOP),” *IEEE J. Select. Topics Quantum Electron.*, vol. 3, no. 6, Dec. 1997.

[208] K. D. Mesel, “Spot-size converters for photonic integrated circuits,” Ph.D. dissertation, Ghent University, Ghent, Belgium, 2002.

[209] M. G. Galarza, “Leaky-waveguide-based integrated spot-size converters for alignment-tolerant optical fiber coupling,” Ph.D. dissertation, Ghent University, Ghent, Belgium, 2003.

[210] B. Hermansson, D. Yevick, and P. Danielsen, “Propagating beam analysis of multimode waveguide tapers,” *IEEE J. Quantum Electron.*, vol. QE-19, no. 8, pp. 1246–1251, Aug. 1983.

[211] I. Moerman, P. P. V. Daele, and P. M. Demeester, “A review on fabrication technologies for the monolithic integration of tapers with III-V semiconductor devices (invited paper),” *IEEE J. Select. Topics Quantum Electron.*, vol. 3, no. 6, pp. 1308–1320, Dec. 1997.

[212] R. S. Fan and R. B. Hooker, “Tapered polymer single-mode waveguides for mode transformation,” *J. Lightwave Technol.*, vol. 17, no. 3, pp. 466–474, Mar. 1999.

[213] K. Yokoyama, N. Sekino, T. Hirono, Y. Tohmori, and Y. Kawaguchi, “Design and fabrication of high-coupling efficiency spot-size converter integrated laser diodes using

three-dimensional BPM program," *J. Lightwave Technol.*, vol. 16, no. 8, pp. 1456–1463, Aug. 1998.

[214] K. Kawano, M. Kohtoku, M. Wada, H. Okamoto, Y. Itaya, and M. Naganuma, "Design of a spotsize-converter-integrated laser diode (SS-LD) with a lateral taper, thin-film core and ridge in the 1.3-μm-wavelength region based on the 3-D BPM," *IEEE J. Select. Topics Quantum Electron.*, vol. 2, no. 2, pp. 348–354, June 1996.

[215] B. Mersali, A. Ramdane, and A. Carenco, "Optical-mode transformer: A III-V circuit integration enabler (invited paper)," *IEEE J. Select. Topics Quantum Electron.*, vol. 3, no. 6, pp. 1321–1331, Dec. 1997.

[216] T. Brenner and H. Melchior, "Integrated optical modeshape adapters in InGaAsP/InP for efficient fiber-to-waveguide coupling," *IEEE Photon. Technol. Lett.*, vol. 5, no. 9, pp. 1053–1055, Sept. 1993.

[217] P. Sewell, T. M. Benson, P. C. Kendall, and T. Anada, "Tapered beam propagation," *IEE Electron. Lett.*, vol. 32, no. 11, pp. 1025–1026, May 1996.

[218] G. R. Hadley, "Wide-angle beam propagation using Padé approximant operators," *Optics Letters*, vol. 17, no. 20, pp. 1426–1428, Oct. 1992.

[219] K. Saitoh and M. Koshiba, "Approximate scalar finite-element beam-propagation method with perfectly matched layers for anisotropic optical waveguides," *J. Lightwave Technol.*, vol. 19, no. 5, pp. 786–792, May 2001.

[220] C.-L. Xu, W.-P. Huang, S. K. Chaudhuri, and J. Chrostowski, "An unconditionally stable vectorial beam propagation method for 3-D structures," *IEEE Photon. Technol. Lett.*, vol. 6, no. 4, pp. 549–551, Apr. 1994.

[221] F. Schmidt and R. März, "On the reference wave vector of paraxial Helmholtz equations," *J. Lightwave Technol.*, vol. 14, no. 10, pp. 2395–2400, Oct. 1996.

[222] D. Yevick and B. Hermansson, "New approach to lossy optical waveguide," *IEE Electron. Lett.*, vol. 21, pp. 1029–1030, Oct. 1985.

[223] ——, “New formulations of the matrix beam propagation method: Application to rib waveguides,” *IEEE J. Quantum Electron.*, vol. 25, no. 2, pp. 221–229, Feb. 1989.

[224] D. Yevick and W. Bardyszewski, “Correspondence of variational finite-difference (relaxation) and imaginary-distance propagation methods for modal analysis,” *Optics Letters*, vol. 17, no. 5, pp. 329–330, Mar. 1992.

[225] S. Jüngling and J. C. Chen, “A study and optimization of eigenmode calculations using the imaginary-distance beam-propagation method,” *IEEE J. Quantum Electron.*, vol. 30, no. 9, pp. 2098–2105, Sept. 1994.

[226] K. Saitoh and M. Koshiba, “Full-vectorial imaginary-distance beam propagation method based on a finited element scheme: application to photonic crystal fibers,” *IEEE J. Quantum Electron.*, vol. 38, no. 7, pp. 927–933, July 2002.

[227] Y. Tsuji and M. Koshiba, “Guided-mode and leaky-mode analysis by imaginary distance beam propagation method based on finite element scheme,” *J. Lightwave Technol.*, vol. 18, no. 4, pp. 618–623, Apr. 2000.

[228] S. S. A. Obayya, B. M. A. Rahman, K. T. V. Grattan, and H. A. El-Mikati, “Full vectorial finite-element solution of nonlinear bistable optical waveguides,” *IEEE J. Quantum Electron.*, vol. 38, no. 8, pp. 1120–1125, Aug. 2002.

[229] G. R. Hadley, “Transparent boundary condition for beam propagation,” *Optics Letters*, vol. 16, no. 9, pp. 624–626, May 1991.

[230] J.-P. Bérenger, “A perfectly matched layer for the absorbtion of electromagnetic waves,” *Journal of Computational Physics*, vol. 114, pp. 185–200, Oct. 1994.

[231] Z. S. Sacks, D. M. Kingsland, R. Lee, and J.-F. Lee, “A perfectly matched anisotropic absorber for use as an absorbing boundary condition,” *IEEE Trans. Antennas Propagat.*, vol. 43, no. 12, pp. 1460–1463, Dec. 1995.

[232] A. Cucinotta, G. Pelosi, S. Selleri, L. Vincetti, and M. Zoboli, “Perfectly matched anisotropic layers for optical waveguides analysis through the finite element beam

propagation method," *Microwave and Optical Technology Letters*, vol. 23, no. 2, pp. 67–69, Oct. 1999.

[233] S. Selleri, L. Vincetti, A. Cucinotta, and M. Zoboli, "Complex FEM modal solver of optical waveguides with PML boundary conditions," *Optical and Quantum Electronics*, vol. 33, no. 4-5, pp. 359–371, Apr. 2001.

[234] S. Selleri, L. Vincetti, and M. Zoboli, "Full-vector finite-element beam propagation method for anisotropic optical device analysis," *IEEE J. Quantum Electron.*, vol. 36, no. 12, pp. 1392–1401, Dec. 2000.

[235] F. Fogli, G. Bellanca, and P. Bassi, "TBC and PML conditions for 2D and 3D BPM: a comparison," *Optical and Quantum Electronics*, vol. 30, no. 5-6, pp. 443–456, May 1998.

[236] A. Mitchell, D. M. Kokotoff, and M. W. Austin, "Improvement to the PML boundary condition in the FEM using mesh compression," *IEEE Trans. Microwave Theory Tech.*, vol. 50, no. 5, pp. 1297–1302, May 2002.

[237] F. L. Teixeira and W. C. Chew, "General closed-form PML constitutive tensors to match arbitrary bianisotropic and dispersive linear media," *IEEE Microwave Guided Wave Lett.*, vol. 8, no. 6, pp. 223–225, June 1998.

[238] ——, "Unified analysis of perfectly matched layers using differential forms," *Microwave and Optical Technology Letters*, vol. 20, no. 2, pp. 124–126, Jan. 20, 1999.

[239] ——, "Complex space approach to perfectly matched layers: a review and some new developments," *Int. J. Numer. Model.*, vol. 13, pp. 441–455, Sept. 2000.

[240] Y. Tsuji and M. Koshiba, "Finite element beam propagation method with perfectly matched layer boundary conditions for three-dimensional optical waveguides," *International Journal of Numerical Modelling: Electronic Networks, Devices and Fields*, vol. 13, pp. 115–126, Mar. 2000.

[241] T. Fujisawa and M. Koshiba, “Full-vector finite-element beam propagation method for three-dimensional nonlinear optical waveguides,” *J. Lightwave Technol.*, vol. 20, no. 10, pp. 1876–1884, Oct. 2002.

[242] W. P. Huang, C. L. Xu, W. Lui, and K. Yokoyama, “The perfectly matched layer (PML) boundary condition for the beam propagation method,” *IEEE Photon. Technol. Lett.*, vol. 8, no. 5, pp. 649–651, 1996.

[243] M. Hikari, M. Koshiba, and Y. Tsuji, “A time domain beam propagation method based on a finite element scheme,” *Electronics and Communications in Japan, Part 2*, vol. 82, no. 11, pp. 52–58, Nov. 1999.

[244] W. P. Huang, C. L. Xu, W. Lui, and K. Yokoyama, “The perfectly matched layer boundary condition for modal analysis of optical waveguides: Leaky mode calculations,” *IEEE Photon. Technol. Lett.*, vol. 8, no. 5, pp. 652–654, 1996.

[245] C. R. Pollock, *Fundamentals of Optoelectronics.* Chicago: IRWIN, 1995.

[246] P. C. Lee, D. Schulz, and E. Voges, “Three dimensional finite difference beam propagation algorithm for photonic devices,” *J. Lightwave Technol.*, vol. 10, no. 12, pp. 1832–1838, Dec. 1992.

[247] D. Schulz, C. Glingener, and E. Voges, “Novel generalized finite-difference beam propagation method,” *IEEE J. Quantum Electron.*, vol. 30, no. 4, pp. 1132–1140, Apr. 1994.

[248] B. Hermansson, D. Yevick, W. Bardyszewski, and M. Glasner, “The unitarity of split-operator finite difference and finite-element methods: applications to longitudinally varying semiconductor rib waveguides,” *J. Lightwave Technol.*, vol. 8, no. 12, pp. 1866–1873, Dec. 1990.

[249] C. Vassallo, “Wide-angle BPM and power conservation,” *IEE Electron. Lett.*, vol. 31, no. 2, pp. 130–131, Jan. 1995.

[250] ——, “Difficulty with vectorial BPM,” *IEE Electron. Lett.*, vol. 33, no. 1, pp. 61–62, Jan. 1997.

[251] J. Yamauchi, K. Matsubara, T. Tsuda, and H. Nakano, “Norm-conserving finite-difference beam-propagation method for TM wave analysis in step-index optical waveguides,” *J. Lightwave Technol.*, vol. 18, no. 5, pp. 721–727, May 2000.

[252] L. Poladian and F. Ladouceur, “Unification of TE and TM beam-propagation algorithms,” *IEEE Photon. Technol. Lett.*, vol. 10, no. 1, pp. 105–107, Jan. 1998.

[253] T. F. Jabłoński, “Complex modes in open lossless dielectric waveguides,” *J. Opt. Soc. Am. A*, vol. 11, no. 4, pp. 1272–1282, Apr. 1994.

[254] Y. Lu and F. A. Fernández, “An efficient finite element solution of inhomogeneous anisotropic and lossy dielectric waveguides,” *IEEE Trans. Microwave Theory Tech.*, vol. 41, no. 6, pp. 1215–1223, June 1993.

[255] T. Fujisawa and M. Koshiba, “Finite element characterization of chromatic dispersion in nonlinear holey fibers,” *OSA Optics Express*, vol. 11, no. 13, pp. 1481–1489, June 2003.

[256] W. H. Press, S. A. Teukolsky, W. T. Vetterling, and B. P. Flannery, *Numerical Recipes in C: the Art of Scientific Computing*, 2nd ed. Cambridge University Press, 1992.

[257] H. Goldstein, *Classical Mechanics*, 2nd ed. Addison-Wesley, 1980.

[258] H. Rao, M. J. Steel, R. Scarmozzino, and R. M. Osgood, Jr., “Complex propagators for evanescent waves in bidirectional beam propagation method,” *J. Lightwave Technol.*, vol. 18, no. 8, pp. 1155–1160, Aug. 2000.

[259] S. S. A. Obayya, “Novel finite element analysis of optical waveguide discontinuity problems,” *J. Lightwave Technol.*, vol. 22, no. 5, pp. 1420–1425, May 2004.

[260] W. Huang, C. Xu, S.-T. Chu, and S. K. Chaudhuri, “The finite-difference vector beam propagation method: Analysis and assessment,” *J. Lightwave Technol.*, vol. 10, no. 3, pp. 295–305, Mar. 1992.

[261] S. S. A. Obayya, B. M. A. Rahman, and H. A. El-Mikati, “New full-vectorial numerically efficient propagation algorithm based on the finite element method,” *J. Lightwave Technol.*, vol. 18, no. 3, pp. 409–415, Mar. 2000.

[262] K. Saitoh and M. Koshiba, “Full-vectorial finite element beam propagation method with perfectly matched layers for anisotropic optical waveguides,” *J. Lightwave Technol.*, vol. 19, no. 3, pp. 405–413, Mar. 2001.

[263] S. Kim and A. Gopinath, “Vector analysis of optical dielectric waveguide bends using finite-difference method,” *J. Lightwave Technol.*, vol. 14, no. 9, pp. 2085–2091, Sept. 1996.

[264] T. Yamamoto and M. Koshiba, “Numerical analysis of curvature loss in optical waveguides by the finite-element method,” *J. Lightwave Technol.*, vol. 11, no. 10, pp. 1579–1583, Oct. 1993.

[265] P. Danielsen and D. Yevick, “Propagating beam analysis of bent optical waveguides,” *Journal of Optical Communication*, vol. 4, pp. 94–98, 1983.

[266] C. Vassallo, *Optical Waveguide Concepts.* The Netherlands: Elsevier, 1991.

[267] M. Heiblum and J. H. Harris, “Analysis of curved optical waveguides by conformal tranformation,” *IEEE J. Quantum Electron.*, vol. QE-11, no. 2, pp. 75–83, Feb. 1975.

[268] W. J. Song, G. H. Song, B. H. Ahn, and M. Kang, “Scalar BPM analyses of TE and TM polarized fields in bent waveguides,” *IEEE Trans. Antennas Propagat.*, vol. 51, no. 6, pp. 1185–1198, June 2003.

[269] H. Deng, G. H. Jin, J. Harari, J. P. Vilcot, and D. Decoster, “Investigation of 3-D semivectorial finite-difference beam propagation method for bent waveguides,” *J. Lightwave Technol.*, vol. 16, no. 5, pp. 915–922, May 1998.

[270] P. Bienstman, E. Six, M. Roelens, M. Vanwolleghem, and R. Baets, “Calculation of bending losses in dielectric waveguides using eigenmode expansion and perfectly matched layers,” *IEEE Photon. Technol. Lett.*, vol. 14, no. 2, pp. 164–166, Feb. 2002.

[271] W. Berglund and A. Gopinath, "WKB analysis of bend losses in optical waveguides," *J. Lightwave Technol.*, vol. 18, no. 8, pp. 1161–1166, Aug. 2000.

[272] H. Takahashi, Y. Hibino, and I. Nishi, "Polarization-insensitive arrayed-waveguide grating wavelength multiplexer on silicon," *Optics Letters*, vol. 17, no. 7, pp. 499–501, Apr. 1992.

[273] R. J. Deri, A. Shahar, E. Colas, R. N. Thurston, W. J. Tomlinson, A. Yi-Yan, and M. Seto, "Single-mode semiconductor optical waveguides with large dimensions suitable for compact bend applications," *Appl. Phys. Lett.*, vol. 57, no. 23, pp. 2396–2398, Dec. 1990.

[274] R. J. Deri and E. Kapon, "Low-loss III-V semiconductor optical waveguides (invited paper)," *IEEE J. Quantum Electron.*, vol. 27, no. 3, pp. 626–640, Mar. 1991.

[275] S. Kitamura, H. Hatakeyama, T. Tamanuki, T. Sasaki, K. Komatsu, and M. Yamaguchi, "Angled-facet S-bend semiconductor optical amplifiers for high-gain and large-extinction ratio," *IEEE Photon. Technol. Lett.*, vol. 11, no. 7, pp. 788–790, July 1999.

[276] T. M. Benson, P. Sewell, S. Sujecki, and P. C. Kendall, "Structure related beam propagation," *Optical and Quantum Electronics*, vol. 31, pp. 689–703, Oct. 1999.

[277] H. G. Jerrard, "Modern description of polarized light: matrix methods," *Optics and Laser Technology*, vol. 14, no. 6, pp. 309–319, Dec. 1982.

[278] J. P. Gordon and H. Kogelnik, "PMD fundamentals: Polarization mode dispersion in optical fibers," *Proceedings of the National Academy of Science of the United States of America (PNAS)*, vol. 97, no. 9, pp. 4541–4550, Apr. 25, 2000.